Electronic Processes in Metal Halide Perovskites

Adam Daizhen Wright

Corpus Christi College

University of Oxford

A thesis submitted for the degree of

Doctor of Philosophy

Trinity 2018

Acknowledgements

I would like to thank the **Engineering and Physical Sciences Research Council** for funding me through the Centre for Doctoral Training in Plastic Electronics. I am also grateful to my college, **Corpus Christi**, for accommodating and otherwise nurturing me for much of my time in Oxford, especially by awarding me a Senior Scholarship in my final year. The teaching and social opportunities which Corpus offered me greatly enhanced my experience of graduate life; I will miss the **MCR**!

I also owe much gratitude to my wonderful supervisors, **Professor Laura Herz** and **Professor Michael Johnston**, for their direction, support and advice, which instilled me with confidence and expertise in a manner suitable to my personality. I have lost count of the times that things turned out better than I had feared, thanks to them.

My labmates have been the lifeblood of my DPhil experience, being ever-supportive in matters scientific and personal: Becky Milot, Laura Martínez Maestro, Kun Peng, James Ball, Mathias Uller Rothmann, Silvia Motti, Jessie Boland, Juliane Gong, Jay Patel, Chris Davies, Beth Parrott, Waqaas Rehman, Sabrina Sterzl, Tim Crothers, Djamshid Damry, Juliane Borchert, Alex Knight, Hannah Eggimann, Kimberley Savill, Chelsea Xia, Leo Buizza, Kilian Lohmann, Olia Zadvorna and Michael Trimpl. I am thankful to them all for being both dependable colleagues and worthy friends, but would like to particularly mention **Becky** for being my constant mentor, **Jay** for his camaraderie on the road that led to this thesis, and **Sabrina** for being so sincere and dependable. Without them, the dark hours in the lab with liquid helium would not have been as bearable as they were. I am also grateful to the support staff in the department and my collaborators, who all helped make my work possible.

Doing a PhD has been my aspiration for as long as I can remember, and with hindsight I can gratefully identify the two educators most instrumental in inducing me to realise this dream: **Dr Bernard Pike**, my secondary school physics teacher, and **Dr Themis Mavrogordatos**, who taught me in Cambridge (sometimes even about Physics). I must also thank my long-time friend **Daniel Rowlands** for his companionship and wisdom on our mostly-common path. Without great support, guidance and counselling, I could not have done what was necessary to reach this point; thank you to those who provided this, especially my friends and family.

Of course, my dear siblings **Tom** and **Emma** and my dear parents **Mai** and **David** laid the foundation for everything, and their love was invaluable throughout. Last but not least, thank you to my darling **Crista** for being here for me.

Abstract

Metal halide perovskites are a class of materials which have recently achieved remarkable success in solar cells. The rapid rate of improvement in the efficiencies of perovskite-based devices has however often outpaced understanding of the electronic processes occurring within these semiconductor materials. This thesis is concerned with providing insight into the factors influencing electron motion and recombination in a series of hybrid metal halide perovskites, principally using photoluminescence spectroscopy. Such knowledge is essential for the development of higher-performance perovskite-based devices.

The temperature dependence of emission line broadening is investigated in the four commonly-studied formamidinium and methylammonium perovskites, $FAPbI_3$, $FAPbBr_3$, $MAPbI_3$ and $MAPbBr_3$, and it is discovered that scattering from longitudinal optical phonons via the Fröhlich interaction is the dominant source of electron-phonon coupling near room temperature, with scattering off acoustic phonons negligible. Energies for the interacting longitudinal optical phonon modes are determined to be 11.5 and 15.3 meV, and Fröhlich coupling constants of approximately 40 and 60 meV are extracted for the lead iodide and bromide perovskites, respectively.

The low-temperature photoluminescence of $FAPbI_3$ is studied, and both a power-law time dependence in the emission intensity, and an additional low-energy emission peak which exhibits an anomalous relative Stokes shift, are observed. Using a rate-equation model and a Monte Carlo simulation, it is revealed that both phenomena arise from the existence of an exponential trap-density tail with characteristic energy scale of $\approx$3 meV. In this high-quality hybrid perovskite, trap states therefore comprise a continuum of energetic levels (associated with disorder) rather than discrete trap energy levels (associated e.g. with elemental vacancies). These first two studies confirm that hybrid perovskites may be viewed as classic semiconductors, using a band-structure picture.

Finally, the relationship between the structural and optical properties of the double perovskite $Cs_2AgBiBr_6$ is examined. Temperature-dependent time-resolved photoluminescence measurements reveal the presence of a 'fast' and a 'slow' carrier decay component, The appearance of the former component correlates with the structural phase-transition to the low-temperature tetragonal phase, indicating that it may originate from the formation of tetragonal twin domains.

Contents

List of Publications

Wright, A. D., Verdi, C., Milot, R. L., Eperon, G. E., Pérez-Osorio, M. A., Snaith, H. J., Giustino, F., Johnston, M. B., and Herz, L. M. "Electron–phonon coupling in hybrid lead halide perovskites". *Nature Communications*, 2016, **7**, 11755.

Wright, A. D., Milot, R. L., Eperon, G. E., Snaith, H. J., Johnston, M. B., and Herz, L. M. "Band-Tail Recombination in Hybrid Lead Iodide Perovskite". *Advanced Functional Materials*, 2017, **27**, 1700860.

Schade, L., **Wright, A. D.**, Johnson, R. D., Dollmann, M., Nayak, P., Prabhakaran, D., Herz, L. M., Nicholas, R., Snaith, H. J., Radaelli, P. G. "Revealing the relationship between the structural and optical properties in the PV candidate $Cs_2AgBiBr_6$ double perovskite". **Manuscript in Preparation**, 2018

Patel, J. B.,Milot R. L., **Wright A. D.**, Herz L. M., Johnston M. B. "Formation dynamics of $CH_3NH_3PbI_3$ perovskite following two-step layer deposition". *The Journal of Physical Chemistry Letters*, 2016, **7**, 96-102.

Davies, C. L., Filip, M. R., Patel, J. B., Crothers, T. W., Verdi, C., **Wright, A. D.**, Milot. R. L., Giustino, F., Johnston, M. B., Herz, L. M. "Bimolecular recombination in methylammonium lead triiodide perovskite is an inverse absorption process". *Nature Communications* 2018, **9**, 293.

Borchert, J., Milot, R. L., Patel, J. B., Davies, C. L., **Wright, A. D.**, Martíinez Maestro, L., Snaith, H. J., Herz, L. M., Johnston, M. B. "Large-Area, Highly Uniform Evaporated Formamidinium Lead Triiodide Thin Films for Solar Cells". *ACS Energy Letters*, 2017, **2**, 2799.

x

List of Abbreviations

Physical Constants

k_B . . . . . 1.38×10^{-23} J K^{-1} (Boltzmann constant)

Abbreviations

CCD . . . . . Charge-Coupled Device

CFD . . . . . Constant Fraction Disciminator

DC . . . . . Direct Current

DSSC . . . . . Dye-Sensitised Solar Cell

FA$^+$ . . . . . Formamidinium ion, $HC(NH_2)_2^+$

fps . . . . . Frames Per Second

FTIR . . . . . Fourier Transform InfraRed

FWHM . . . . Full-Width at Half-Maximum

iCCD . . . . . intensified Charge-Coupled Device

IRF . . . . . Instrument Response Function

LA . . . . . Longitudinal Acoustic

LO . . . . . Longitudinal Optical

MA$^+$ . . . . . Methylammonium ion, $CH_3NH_3^+$

MCP . . . . . Micro Channel Plate

MHP . . . . . Metal Halide Perovskite

ND . . . . . Neutral Density

OPV . . . . . Organic PhotoVoltaic

PCE . . . . . Power Conversion Efficiency

PL . . . . . Photoluminescence

PMT . . . . . Photomultiplier Tube

SPAD . . . . . Single Photon Avalanche Diode

TA . . . . . Transverse Acoustic

TO . . . . . Transverse Optical

1 Introduction

It is a truth universally acknowledged, that a civilisation subject to increasing energy demands and dependent on non-renewable and environmentally deleterious fossil fuels, must be in want of a good alternative energy source. Among the many possibilities, solar radiation represents a vast source of clean, renewable energy [1]. Harnessing solar power incident on only 0.16% of the land on this planet (roughly the size of Romania) at just 10% efficiency would generate 20 TW [2], well in excess of the world power consumption of 12.45 TW in 2015 [3].

Solar energy may be used to produce hydrogen fuel, or converted into thermal or electrical energy [1]. Electricity generated from sunlight via the photovoltaic effect [4] constituted over 95% of the world's solar energy production in 2015 [3], of which almost all (95% in 2017 [5]) is produced by solar cells based on crystalline silicon. Commercial silicon cells typically have power conversion efficiencies (PCEs) between 14 and 20% [6], though the record for research-grade cells is nearly 27% [5]. Although silicon cells currently dominate the market thanks to their high PCEs and long-term durability, they face competition from technologies based on thin-film absorbers [7]; these offer lower production costs and less energy-intensive fabrication processes than are required to

produce the highly-purified silicon needed for solar cells [8, 9].

The most promising of these rival materials are the metal halide perovskites (MHPs), which can be made from earth-abundant chemicals and processed at low temperatures [9]. Furthermore, they possess a remarkable combination of structural and optoelectronic properties which make them excellent photovoltaic materials [10], facilitating an unprecedented rise in their PCEs to 23.3% [11] just 13 years after Miyasaka *et al.* [12] first started researching MHP solar cells. However, understanding of the underlying physical processes which govern the favourable properties of MHPs has not always kept pace with the rapid improvements in MHP-based devices [13]. Early MHP solar cells used 'hybrid' perovskites (containing both organic and inorganic components) in device architectures analogous to those used in organic polymer photovoltaics (OPV) [14, 15], leading to uncertainty over the extent to which MHPs could be described in terms of an inorganic semiconductor bandstructure picture [16].

The work presented in this thesis therefore examines factors influencing electronic motion and recombination in MHPs, with the aim of informing future improvements in optoelectronic devices based on these materials. In doing so, it explores how well electronic processes in these materials resemble those of a typical inorganic semiconductor.

To that end, Chapter 2 provides background on MHPs. By briefly reviewing the progress of these materials from obscure curiosities towards commercial success, the unique properties which make them worth researching are laid out while giving context to the importance of the material compositions studied in this thesis. The current literature understanding of electronic behaviour in MHPs is also summarised, with particular emphasis on how it can be probed using photoluminescence (PL) spectroscopy. The experimental techniques of time-correlated single photon counting (TCSPC) and gated intensified charge-coupled device (iCCD) spectroscopy, which were used to measure PL from MHPs in this work, are then discussed in detail in Chapter 3. These allow

charge recombination processes to be probed with time resolution from the picosecond to microsecond scale while also following the evolution of the emission spectra as a function of time, excitation power and temperature.

PL spectroscopy forms the basis of the results presented and discussed in Chapter 4, in which the strength and nature of the interactions between electrons and phonons in four hybrid perovskite materials: $MAPbI_3$, $FAPbI_3$, $MAPbBr_3$ and $FAPbBr_3$ are investigated. Phonons are collective lattice vibrations which can scatter charge carriers, so setting the fundamental upper limit on their speed [17]. By measuring the phonon-derived broadening of the PL spectra of these materials at temperatures from 4 K up to 370 K, Fröhlich coupling to longitudinal optical phonons is identified as the dominant source of charge-carrier scattering at room temperature in the four materials, and the strength of their electron-phonon coupling is quantified. It is found that although the choice of organic cation has relatively little effect on the Fröhlich interactions, bromide perovskites exhibit higher Fröhlich coupling than iodide perovskites as a result of their smaller high-frequency values of the dielectric function. The increased scattering from LO phonons in bromide perovskites may be the cause of their lower THz charge-carrier mobilities relative to iodide perovskites [18]. These findings are supported by first-principles theoretical calculations performed by collaborators, underlining the suitability of an electronic bandstructure picture for describing charge carriers in MHPs.

Whereas phonons provide the fundamental intrinsic limit to charge-carrier mobilities in MHPs, defects and impurities are an extrinsic source of scattering; this may be limiting for DC transport over large length scales [19]. Charge transport is also affected by sub-bandgap energetic states (traps), in which some carriers may become trapped and so cause a reduction in the overall conductivity [20]. Chapter 5 uncovers a new source of charge-carrier trapping in $FAPbI_3$ in the form of an exponentially-distributed band-tail of sub-bandgap states. Through measurement of the low-temperature PL of $FAPbI_3$,

a power-law time dependence in the decay of the emission intensity, and an additional low-energy emission peak which exhibits an anomalous relative Stokes shift, are observed: both signatures of band-tail mediated recombination. This interpretation is supported by carrying out both an analytical rate-equation model and classical Monte Carlo simulations to describe the effects of the band-tail recombination on the low-temperature PL, which permit the quantification of the characteristic energy of the band tail to be approximately 3 meV. Such a reasonably shallow tail may contribute to the high charge-carrier mobility of $FAPbI_3$ [18], while the observed deeper states of the tail may in part be responsible for the open-circuit voltage losses commonly observed in these materials. Since energetic band tails are a common feature of classic inorganic semiconductors, the observations and analysis in this chapter support the characterisation of MHPs as being one of them, even when containing partly-organic components.

A further investigation in Chapter 6 focuses on the double perovskite $Cs_2AgBiBr_6$, which differs from the MHPs studied in earlier chapters in that it does not suffer from the inclusion of toxic lead [21]. $Cs_2AgBiBr_6$ also differs from these Pb-based materials however by the indirect nature of its bandgap, which complicates its photovoltaic potential [22]. In order to aid the engineering of double perovskites with more favourable properties, such as a direct or tunable bandgap, a deeper understanding of the relationship between the structural and optical properties of this material is required. Therefore, Chapter 6 applies time-dependent PL measurements to $Cs_2AgBiBr_6$, revealing a charge-carrier recombination mechanism which disappears at the structural phase transition from the low-temperature phase, and so may originate from the formation of tetragonal twin domains. The temperature dependence of the PL and absorption spectra of $Cs_2AgBiBr_6$ are analysed in terms of an indirect bandgap, confirming again the applicability of a classic bandstructure picture to MHPs.

Finally, Chapter 7 summarises the work described in this thesis, and provides an outlook on potential further studies which could extend it.

2
Background

Contents

This chapter reviews the electronic and optical properties of MHPs. These properties must be considered in the context of the remarkable promise that MHPs hold as photovoltaic materials, since this is the principal purpose for which understanding of these properties is sought. Therefore, after introducing these materials, this chapter gives an overview of the history of MHP-based solar cells and the challenges they face on the road

to commercial success. Particular emphasis is given to the role of material composition, since the effect of varying this on electronic processes is a major theme of his work. Next, a review of the current state of understanding of the optoelectronic properties of perovskites is given, followed by an account of how measurement of photoluminescence can be used to give a window on these properties: this provides the foundation for the photoluminescence spectroscopy experiments which underpin most of the results in this thesis. The remaining sections of this chapter give the background to the experimental results presented in later chapters, covering electron-phonon coupling, trap states in MHPs and double perovskites.

2.1 Structure

Perovskites are a class of materials with stoichiometry ABX_3 and sharing a crystal structure with $CaTiO_3$, which was first classified by Gustav Rose in 1839. He named it in honour of the mineralogist Lev Perovski of Russia, where it was discovered [23]. Silicate perovskites are highly abdundant in the Earth's mantle [24], but the metal halide perovskites (often synecdochically referred to as just 'perovskites' within the field) which are the subject of this thesis are artificial. For MHPs, A is a monovalent cation which can either be organic or inorganic: the most common organic cations are methylammonium ($CH_3NH_3^+$ or MA^+) and formamidinium ($HC(NH_2)_2^+$ or FA^+), while caesium (Cs^+) is the most common inorganic one. B is a divalent metal cation (usually Pb^{2+}) and X is a halide anion (I^-, Br^- or Cl^-) [13]. The ideal cubic perovskite crystal structure is shown in Fig. 2.1, which is the high-temperature phase of MHPs. At lower temperatures, up to two phase transitions may occur to phases in which such structures as the orthorhombic, tetragonal, trigonal or hexagonal phases have been reported [25]. The structural flexibility of MHPs allows a wide compositional parameter space to be explored, although the sizes of the ions which can form an ideal perovskite structure are dictated by the Goldschmidt tolerance factor [26], which limits the possibilities for substitutions at each site. If the A cation

is replaced by a larger ion than allowed by the tolerance factor, the three-dimensional structure will transition to a layered structure known as a two-dimensional perovskite; however, it is 3D MHPs which are the focus of this thesis [27].

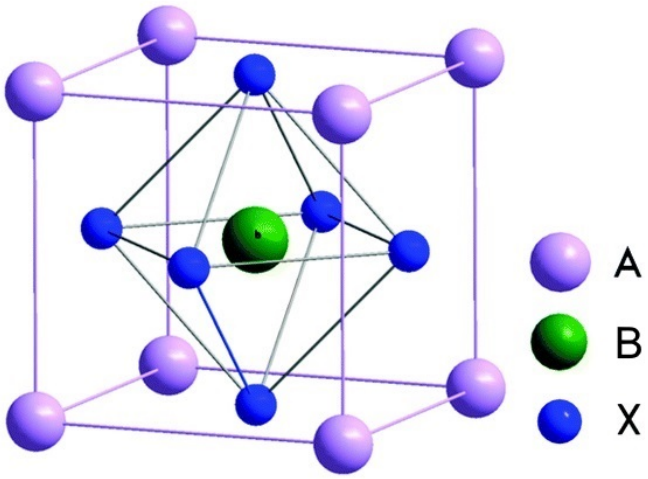

Figure 2.1: Crystal structure of a MHP in the cubic phase. MHPs have the chemical formula ABX_3, where A is a monovalent cation, B is a divalent metal cation, and X is a halide anion. Reproduced from Ref. [28] with permission from The Royal Society of Chemistry.

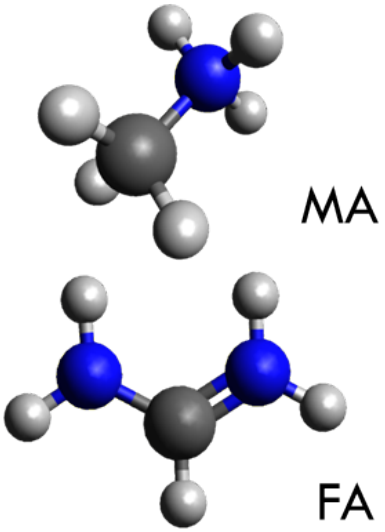

Figure 2.2: Chemical structures of the MA and FA cations. Nitrogen is represented by blue, carbon is black and hydrogen is grey-white.

2.2 Evolution of MHP solar cells

MHPs have been synthesised since as far back as 1882 [29], but it was not until the l970s and 1980s that their fundamental optoelectronic properties were first studied, by Weber *et al.* [30, 31]. Mitzi *et al.* [32–35] built on this work in the 1990s and 2000s, exploring the synthesis of a range of MHPs, particularly those with an organic A cation, known as hybrid organic-inorganic perovskites. However, it was not until 2005 that the work on the first ultimately succesful MHP solar cell began, due to a serendipitous collaboration between researchers investigating 2D perovskites for use in LEDs and those investigating dye-sensitised solar cells (DSSCs) [12]. DSSCs contain a mesoporous layer of an n-type semiconductor, typically TiO_2, coated in a molecular dye and immersed in an electrolyte solution. The dye absorbs sunlight while the semiconductor acts as a charge transporter for the photoexcited electrons from the dye. Miyasaka *et al.* employed $MAPbI_3$ nanocrystals as the sensitiser in a DSSC architecture, replacing the dye, and published the first peer-reviewed paper on a MHP solar cell in 2009, achieving a PCE of 3.8 % [36] with an architecture like that shown in Fig. 2.3a.

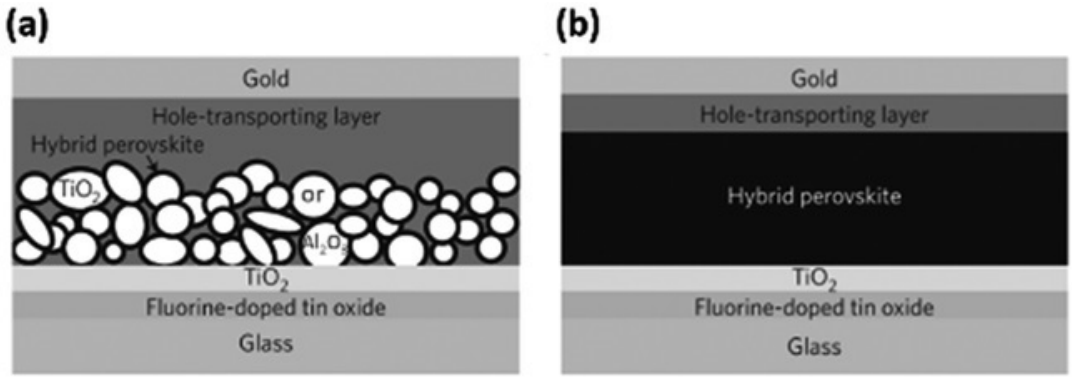

Figure 2.3: Device architectures for MHP solar cells. **(a)** shows the mesoporous perovskite-sensitised architecture, which was derived from DSSCs. **(b)** shows the planar heterojunction configuration. Reproduced from Ref. [37] with permission from The Royal Society of Chemistry.

These initial MHP solar cells were only stable for a few minutes before the perovskite dissolved in the liquid electrolyte. In 2012 two collaborations, one involving Snaith,

Miyasaka *et al.* [38], the other including Park, Grätzel *et al.* [39] concurrently succeeded in producing wholly solid-state MHP solar cells in 2012, using spiro-OMeTAD as the solid hole transport material and achieving PCEs of around 10 %. Notably, these devices used Al_2O_3 as the mesoporous mount for the $MAPbI_3$. Al_2O_3 is an insulator so acted only as a scaffold for the perovskite; the $MAPbI_3$ was a good electron transport material in its own right. After it was also found that $MAPbI_3$ could act as a hole transport material [40], planar heterojunction MHP solar cells became possible. Their structure is shown in Fig. 2.3b; planar architectures are more compatible with large-scale fabrication, particularly using vapour deposition, than meso-structured device architectures [41]. These developments triggered a period during which remarkable advances in MHP synthesis and device fabrication occurred [29], as manifested in the unprecedented improvement of the PCEs of MHP solar cells (see Fig. 2.4). Detailed accounts of the advances during this period can be found in Refs. [42], [43], and [28].

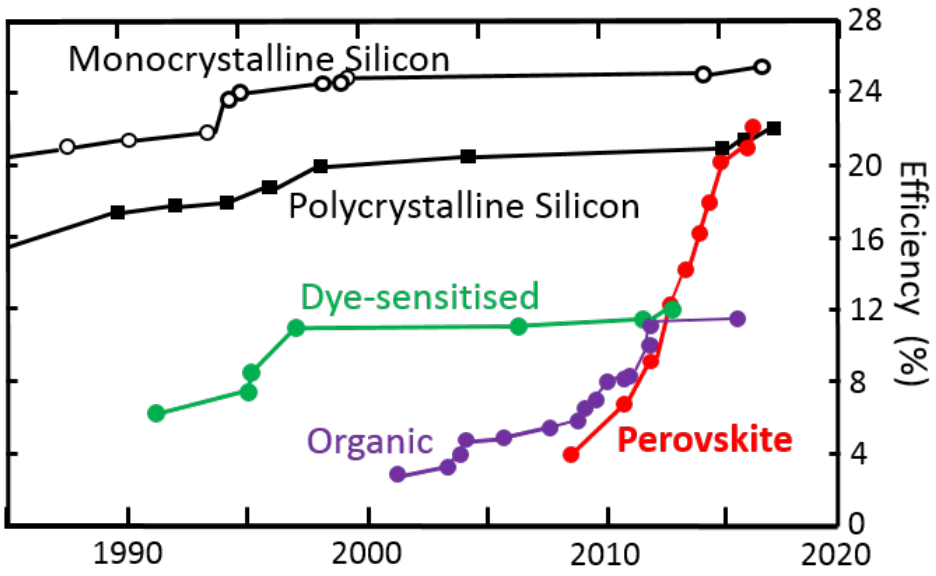

Figure 2.4: Progression of solar cell PCEs for MHPs and competitor technologies. Data derived from Ref. [11].

While $MAPbI_3$ remains the archetypal MHP [44], it suffers from an intrinsic thermal instability due to the relatively volatile methylammonium ions, which evaporate during

heating [27, 44]. Furthermore, $MAPbI_3$ is prone to degradation in the presence of oxygen and moisture [27], and the presence of toxic lead in a readily water-soluble form is also of concern from a health and environmental perspective [45], although encapsulation may ameliorate these issues. MHPs with different compositions have therefore been investigated with the aim of avoiding these issues, and indeed some of the most efficient and stable MHP solar cells contain multiple mixtures of different ions at the A and X sites [44, 46]. Replacing lead with tin, or combinations of other metals such as bismuth and silver, is also under investigation [47]. The record PCE for a MHP solar cell now stands at 23.3% [11], partially thanks to developments in understanding how chemical composition affects the material and optoelectronic properties of MHPs. In order to continue progress towards the Shockley-Queisser limit (the theoretical thermodynamic maximum PCE for a single-junction solar cell [48]), improvements in the optical design and material quality will also be needed [19, 49]. While these challenges continue to be addressed, the commercial viability for MHP solar cells in the short- to medium-term may lie in co-operation with their dominant rival technology of silicon, in the form of perovskite-silicon tandem cells [49].

2.3 Optoelectronic properties

MHPs combine the advantages of facile and inexpensive synthesis via solution processing or vapour deposition techniques [50, 51], with outstanding device PCEs. The prospect of mass-producing high-efficiency solar cells generating low-cost electricity is the ultimate driver of most research into MHPs. A lot of this research, including this work, has focused on the optoelectronic properties of MHPs, whose unique combination thereof provides the foundation for their high PCEs [10].

2.3.1 Absorption and exciton dissociation

MHPs are well-suited to every step of the photovoltaic process. As evident from their origins as a sensitiser in DSSCs, MHPs are good light absorbers, possessing high absorption coefficients ($\sim 10^5 \text{cm}^{-1}$ [52]) across the visible spectrum [19]. Furthermore, their composition can be varied to achieve a bandgap within 1.1 and 1.4 eV, absorbing the optimal amount of the solar spectrum for a single-junction solar cell [53]. Upon absorbing a photon, the excited electron remains Coulombically bound to the hole it leaves behind in the valence band: this bound state is an exciton [13]. The archetypal MHP, $MAPbI_3$, has a sufficiently low exciton binding energy, E_b, that the thermal energy at room temperature ($k_\text{B}T \approx 26\,\text{meV}$) is sufficient to dissociate the electrons and holes and allow them to be part of the photocurrent. This is in contrast to the organic molecular semiconductors used in organic photovoltaics, a competitor technology to MHP solar cell; their exciton binding energies are so high that additional measures must be taken to cause the excitons to dissociate, at the cost of using unstable nanostructured materials and reducing some of the output photovoltage [54]. It should be noted that there has been considerable variation (5 to 50 meV) in the reported values of E_b for $MAPbI_3$ [13], but the consensus is that the excitons dissociate efficiently at room temperature [55].

2.3.2 Charge transport

Having separated the photogenerated charge-carriers, MHPs then exhibit excellent charge-transport properties. These can be quantified by the charge-carrier diffusion length, L_D, which is defined as

$$L_\text{D} = \sqrt{\frac{\mu k_\text{B} T}{e R_T}} \tag{2.1}$$

where μ is the charge-carrier mobility, e is the elementary charge, and R_T is the total charge-carrier recombination rate [19]. L_D represents the average distance a charge carrier

can diffuse without undergoing recombination. A long L_D is beneficial for the internal quantum efficiency of a solar cell, since it means that photogenerated charge carriers are more likely to be able to reach the boundary of the absorber material and thence the external circuit [56]. Electron and hole diffusion lengths of several micrometers have been measured in $MAPbI_3$ [57, 58]. In planar heterojunction solar cells, the absorber layer thickness will be larger than the absorption depth (hundreds of nanometres for $MAPbI_3$ [59]) in order to optimise the number of photons absorbed, so for efficient charge collection the diffusion lengths should exceed the absorption depth: the long L_D in $MAPbI_3$ makes this possible [19]. Since R_T (which may be considered to be a pseudo first-order recombination rate coefficient) is dependent on the charge-carrier density (as expressed in Eqn. 2.2), the diffusion length is also dependent on the charge-carrier density. Furthermore, MHP solar cells are unusual in that electron transport to the contacts is dominated by diffusion rather than by drift, due to electric field screening by mobile ions [60, 61].

As expressed in Equation 2.1, L_D is proportional to the square root of the product of the mobility and the recombination lifetime (the inverse of the total recombination rate). For $MAPbI_3$ and $FAPbI_3$, μ has been measured to be of the order of 10 $cm^2\ V^{-1}s^{-1}$ using terahertz spectroscopy [19], which is considered 'high' by some [62, 63] but only modest by others [10, 64]. Certainly they are higher than in organic semiconductors, against which MHPs have often been benchmarked due to the frequent presence of an organic cation in their compositions [64]. However, the electronic structure at the band edges in $MAPbI_3$ is dominated by orbitals from the inorganic skeleton of the lattice [65], so their bandstructure resembles a typical inorganic semiconductor. Additionally, their carrier effective masses are close to those of Si and GaAs [64, 66], the archectypal inorganic semiconductors. It therefore may be more appropriate to benchmark MHPs against inorganic semiconductors instead (as is discussed later in this thesis, in Chapters

4 and 6), in which case the perovskite mobilities are relatively low. In any case, the slow recombination rate in MHP films makes up for any deficiency in the mobility, with lifetimes up to several μs having been measured [67].

2.3.3 Recombination

The dynamics of charge-carrier recombination can be described by the following rate equation:

$$\frac{dn}{dt} = -k_3 n^3 - k_2 n^2 - k_1 n = -nR_T(n) \tag{2.2}$$

where n is the charge-carrier density, k_1 is the decay constant for first-order decay processes, k_2 is the second-order (electron-hole) recombination rate constant and k_3 is the Auger recombination rate constant [19]. R_T is the total recombination rate which appears in Equation 2.1. These processes are depicted in Fig. 2.5. First-order and second-order decay processes in MHPs are typically referred to as monomolecular and bimolecular respectively [13, 68], terms which have their roots in molecular spectroscopy and are not strictly meaningful for inorganic semiconductors, but are nevertheless employed henceforth in this thesis in keeping with convention in this field. Monomolecular recombination involves one charge-carrier, is typically mediated by traps, and can be radiative or nonradiative depending on the mechanism involved [69]. Auger processes involve a third charge-carrier which carries away the energy and momentum released by the nonradiative recombination of an electron and a hole, but are relatively unimportant at the charge carrier densities involved in photovoltaic applications [19]. Finally, bimolecular recombination involves intrinsic electron-hole recombination, is radiative [13], and can be explained as the inverse process of absorption, similar to GaAs [55]. The low bimolecular recombination rate is an underlying cause of the long L_D and hence good transport properties of MHPs. Meanwhile, reducing trap-mediated monomolecular recombination is only capable of

extending L_D to a limited extent [19]. It should be noted that a more complex treatment of trap-mediated recombination, accounting for doping in the semiconductor, can result in recombination kinetics being observed as anything ranging from monomolecular to bimolecular depending on the doping density, excitation fluence and trap depth [68].

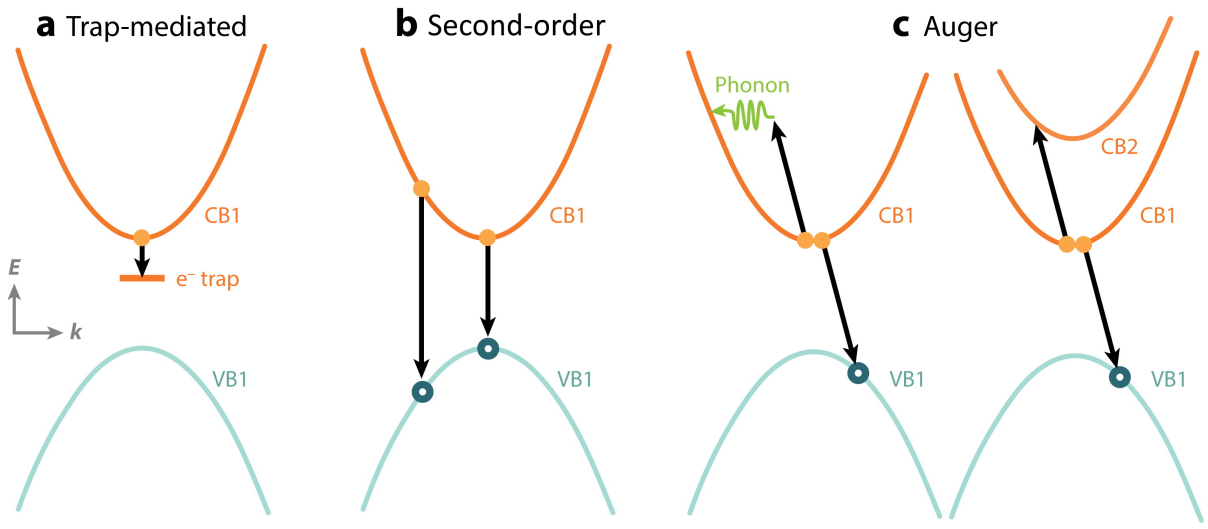

Figure 2.5: Recombination mechanisms active in MHPs. The valence band (VB) is shown in light blue, and the conduction band (CB) is shown in orange. **(a)** shows trap-mediated monomolecular recombination in which an electron is captured by a trap state; this is also possible for holes. **(b)** shows intrinsic bimolecular recombination, in which an electron and a hole recombine either between the CB minimum and VB minimum, or from states higher in the bands. **(c)** depicts Auger recombination, a higher-order process in which an electron and hole recombine non-radiatively by transferring energy to a third charge-carrier. Taken from Ref. [13], used with permission from Annual Reviews via the Copyright Clearance Center.

2.4 Functional form of fits to PL transients

Photoluminescence measurements have been extensively used to study the photophysical and semiconducting properties of MHPs [70–73]. Lead-based MHPs are direct bandgap semiconductors and emit in a relatively narrow band just below the absorption edge [74], with steady-state emission spectra as shown in Fig. 4.2. Transient PL measurements have determined that the recombination of photoexcited charge carriers is strongly fluence-dependent [70], as expected from the dependence on charge-carrier density in Equation 2.2.

In order to gain information about the recombination coefficients of a material, and the prevalent recombination mechanisms therein, it is necessary to quantitatively model the time dependence of the PL intensity. For a simplistic two-level quantum system, this time dependence can be modelled by a single exponential function, in which case a clear charge-carrier lifetime can be assigned. However, the presence of traps and multiple possible transitions makes non-exponential PL transients a common sight. Below, the most common functions which are fitted to MHP PL transients are outlined.

2.4.1 Exponential decays

At lower excitation densities, monomolecular recombination dominates. The mono-exponential function

$$I_{\mathrm{me}}(t) = I_0 e^{-k_1 t} \tag{2.3}$$

commonly [75, 76] used to fit photoluminescence (PL) transients, arises from neglecting the bimolecular and Auger terms in Equation 2.2, and taking the PL intensity $I_{\mathrm{me}}(t)$ to be proportional to n. I_0 is the PL intensity at $t = 0$. A biexponential function

$$I_{\mathrm{be}}(t) = I_1 e^{-t/\tau_1} + I_2 e^{-t/\tau_2} \tag{2.4}$$

may instead be used to account for both a fast and a slow monomolecular decay component, attributable to separate populations of charge carriers [77, 78]. A stretched exponential function

$$I_{\mathrm{se}} = I_0 e^{-(t/\tau_c)^{\beta}} \tag{2.5}$$

has also been used to phenomenologically account for the presence of a local distribution of monoexponential decay rates [79, 80]. Here, a more heterogeneous distribution of decay rates corresponds to a distribution coefficient, β, which is closer to 0 than 1, while

the time taken for the PL intensity to drop to I_0/e is τ_c, the characteristic lifetime [79]. The average lifetime of a stretched exponential function is often given as

$$\tau_{av} = \frac{\tau_c}{\beta}\Gamma\left(\frac{1}{\beta}\right) \tag{2.6}$$

where Γ is the gamma function [81]. However, this diverges as β tends to 0 so is not always very meaningful as an average lifetime [82].

2.4.2 Bimolecular recombination

Alternatively, bimolecular recombination may be taken into account as well [83]. If only the Auger recombination term is neglected, integration of Equation 2.2 yields:

$$n_{bm}(t) = \frac{k_1}{k_2}\left[e^{k_1 t}\left(1 + \frac{k_1}{n_0 k_2}\right) - 1\right]^{-1} \tag{2.7}$$

where n_0 is the initial charge-carrier density.

2.4.3 Power-law decays

The sum of many monoexponential decays with densely distributed lifetimes τ_i, $I(t) \sim \sum_i e^{-t/\tau_i}$, approximates to a power-law decay [84] with exponent α, i.e. a function of the form

$$I_{pl}(t) = I_0 t^{-\alpha} \tag{2.8}$$

as detailed in Section 2.5.

2.5 Power-law time dependence of PL

Power-law decays take the form $I(t) \propto t^{-\alpha}$, where I is intensity, t is time and α is some positive constant, and result from the superposition of many monoexponential decays with densely-distributed recombination rates [84–86]. Several models have been developed to explain the physical origin of power-law decays for luminescence [85, 87–90]. A common

feature is that charge carriers are localized in trap states with an occupation probability $p(t)$ of the form $p\,(t) = \ e^{-\gamma t}$, where the functional form of the escape rate γ varies with the model [91]. The models can be divided into two categories, in which the escape rate depends on either the energetic depth of the traps (Arrhenius detrapping models) or the separation between traps (hopping models). In both cases, the total PL intensity can be shown analytically to decay as a power law, given certain reasonable assumptions.

2.5.1 Arrhenius detrapping models

In Arrhenius detrapping models, the escape rate from a trap of energetic depth ϵ has the form

$$\gamma_{\mathrm{Arr}}(\epsilon) = \nu_0 e^{-\epsilon/k_{\mathrm{B}}T} \tag{2.9}$$

where ν_0 is the attempt-to-escape frequency [91]. The PL intensity decays as a power law if the energetic distribution of the traps is exponential [87, 92, 93].

In the simplest such model the charge carrier is assumed to rapidly undergo radiative recombination after escaping to the band edge, without retrapping [94]. Randall and Wilkins [87, 94] analytically derive a power-law decay under these conditions as follows:

If $N(\epsilon, t)$ is the number of charge-carriers in traps of depth ϵ at time t, then

$$\frac{\mathrm{d}N(\varepsilon, t)}{\mathrm{d}t} = -N\,(\epsilon, t)\,\gamma_{\mathrm{Arr}}(\epsilon) \tag{2.10}$$

Integrating then gives

$$N\,(\epsilon, t) = N_0(\epsilon) \exp\left(-\nu_0 t e^{-\epsilon/k_{\mathrm{B}}T}\right) \tag{2.11}$$

where $N_0\,(\epsilon) = N\,(\epsilon, 0)$. The PL intensity $I(t)$ is proportional to the rate of supply of charge carriers to the band edge, so if the traps have an energetic distribution given by $n(\epsilon)$,

$$I\,(t) \propto \int_0^\infty n(\epsilon) \frac{\mathrm{d}N(\epsilon, t)}{\mathrm{d}t} \mathrm{d}\epsilon \tag{2.12}$$

Thus, for an exponential energetic distribution of traps with characteristic depth ϵ_0, $n(\epsilon) = Ae^{-\epsilon/\epsilon_0}$, and assuming $N_0(\epsilon) \propto n(\epsilon)$,

$$I(t) \propto \int_0^\infty Ae^{-\epsilon/\epsilon_0} \exp\left(-\nu_0 t e^{-\epsilon/k_B T}\right) \nu_0 e^{-\epsilon/k_B T} d\epsilon \tag{2.13}$$

Substitution of $\xi = \nu_0 t e^{-\epsilon/k_B T}$ yields

$$I(t) \propto A \frac{k_B T}{t} (\nu_0 t)^{-k_B T/\epsilon_0} \int_0^{\nu_0 t} \xi^{-k_B T/\epsilon_0} \exp(-\xi) d\xi \tag{2.14}$$

The upper limit of the integral may be taken to infinity since for typical observation times, $t \gg \nu_0$. Therefore

$$I(t) \propto t^{-(1+k_B T/\epsilon_0)}, \tag{2.15}$$

a power law decay [87].

The multiple-trapping model is a more sophisticated Arrhenius detrapping model, in which charge-carriers are permitted to be repeatedly excited to, and retrapped from, the band-edge [93]. Orenstein and Kastner [93] describe how multiple-trapping causes the transient photocurrent to exhibit power-law kinetics. Their formalism can also be applied to the PL by considering activation to the band edge rather than the mobility edge.

2.5.2 Hopping models

In the case of hopping models, trapped charge-carriers tunnel between localized traps spatially separated by distance r at a rate [91, 95]

$$\gamma_{\text{hop}}(r) = Ae^{-r/R_0}, \tag{2.16}$$

$$A = \nu_0 e^{-\delta\epsilon/k_B T} \qquad \text{for } \delta\epsilon > 0 \tag{2.17}$$

$$= \nu_0 \qquad \text{for } \delta\epsilon < 0 \tag{2.18}$$

where R_0 is the decay length of the charge-carrier wavefunction and A is a prefactor containing the frequency of escape attempts ν_0 and the difference in energy between the destination and origin sites for the hopping, $\delta\epsilon$.

Huntley [85] uses a model in which one sign of charge carrier is mobile, to derive an approximate power law decay for the case when the traps are randomly distributed in space. In an analogous fashion to Equation 2.12, the PL intensity $I(t)$ in these models is proportional to the rate at which oppositely-charged carriers tunnel together, so

$$I\left(t\right) \propto \int_0^\infty p(r)\frac{\mathrm{d}N(r,t)}{\mathrm{d}t}\mathrm{d}r \tag{2.19}$$

where $p(r)$ is the probability that such a recombining pair of carriers are in traps separated by r and $N(r,t)$ is the number of such pairs separated by r at time t. Charge carriers are assumed to recombine with their nearest eligible neighbour, and A is assumed to be constant.

For recombination centres randomly distributed in space, the probability of a recombination centre being within a volume V of a trapped carrier follows the exponential distribution, with probability density $p\left(V\right) = \rho e^{-\rho V}$. The probability that the nearest recombination centre lies between a distance of r and $r+\mathrm{d}r$ of the trapped carrier is therefore

$$p\left(r\right)\mathrm{d}r = e^{-\frac{4}{3}\rho\pi r^3}4\pi\rho r^2\mathrm{d}r \tag{2.20}$$

By the same steps as expressed in Equations 2.10 to 2.13, we arrive at

$$I\left(t\right) \propto \int_0^\infty e^{-\frac{4}{3}\pi\rho r^3}4\pi\rho r^2 \exp\left(-Ate^{-r/R_0}\right)Ae^{-r/R_0}\mathrm{d}r \tag{2.21}$$

Assuming that most electrons recombine around their mean lifetime $1/\gamma_{\mathrm{hop}}(r)$, at a given time t then all electrons within a distance r_c of a recombination centre will have tunnelled there, where

$$t = \frac{1}{\gamma_{\mathrm{hop}}(r_c)} = A^{-1}e^{r_c/R_0}, \tag{2.22}$$

$$r_c = R_0 \ln(At) \tag{2.23}$$

Then the integral in Equation 2.21 reduces to only the case when $r = r_c(t)$, so

$$I(t) \propto e^{-\frac{4}{3}\pi(R_0 \ln(At))^3} 4\pi\rho R_0^3 (\ln(At))^2 t^{-1} \tag{2.24}$$

This approximates to t^{-1} provided the density of recombination centres is not too large relative to the volume of the charge-carrier wavefunction ($\rho \ll \frac{4}{3}\pi R_0^3$). In Dunstan's model of distant-pair recombination, the possibility that an electron's nearest neighbour hole may recombine with its own nearer neighbour electron is also accounted for [88]. This complicates the form of $p(r)$, but still produces power-law PL decays.

2.6 Electron-phonon coupling

While much recent attention has been devoted towards unravelling the charge-carrier recombination mechanisms underlying the excellent optoelectronic properties of MHPs [13, 19], the interaction of charge-carriers with lattice vibrations (phonons) is currently still a subject of intense debate [64, 96]. Such electron-phonon interactions matter because they set a fundamental intrinsic limit to charge-carrier mobilities in the absence of extrinsic scattering off impurities or interfaces [17]. In addition, charge-carrier cooling following non-resonant (above bandgap) photon absorption is governed by interactions between charges and phonons [13]. Slow charge-carrier cooling components (compared to GaAs) have been postulated for hybrid perovskites [97] which may open the possibility for PCEs beyond the Shockley-Queisser limit. Furthermore, electron-phonon coupling has been shown to yield predominantly homogeneous emission line broadening in hybrid lead iodide perovskite at room temperature, making it suitable as a gain medium for short-pulse lasers [59].

Along high-symmetry directions in crystals, phonons can be classified according to the direction in which they displace ions: perpendicular to the direction of the phonon wave vector in the case of transverse phonons, parallel for longitudinal phonons [17]. For

crystals with at least two atoms in their primitive cell, the phonon dispersion relations can exhibit two types of phonon branch: acoustic and optical. The acoustic phonon branches have lower energies and consist of modes in which adjacent ions are displaced in-phase with each other, whereas optical phonons cause adjacent ions to move out of phase. Schematics of the ionic displacements caused by transverse acoustic (TA), transverse optical (TO), longitudinal acoustic (LA) and longitudinal optical (LO) phonons are shown in Fig. 2.6. Electron-phonon coupling is governed by the changes in the electronic Hamiltonian with nuclear displacements in the lattice. The first type of change is caused by deformation potential interactions: lattice distortions due to phonons change the bandstructure and hence the electronic Hamiltonian. Long-wavelength acoustic phonons can cause ionic displacements similar to placing the crystal under macroscopic strain, oscillating at the phonon frequency. Long-wavelength optical phonons meanwhile involve only relative displacements of alternating ions so can cause only microscopic strains, but these can still affect bond angles and lengths, and hence variations in the bandstructure. The second type of change involves electromechanical or piezoelectric interactions, which create an electric field that modifies the electronic Hamiltonian. In noncentrosymmetric crystals, a macroscopic electric polarization field can be generated by a stress. This is known as the piezoelectric effect, and can be caused by the oscillating strain field associated with long-wavelength acoustic phonons. In polar or partly ionic crystals with more than one ion per primitive cell meanwhile, LO phonons cause uniform displacement of adjacent sheets of oppositely-charged ions, as shown in Fig. 2.6. In an analogous fashion to pulling apart the plates of a parallel-plate capacitor, this results in a longitudinal electric field which interacts with electrons: this is termed the Fröhlich interaction.

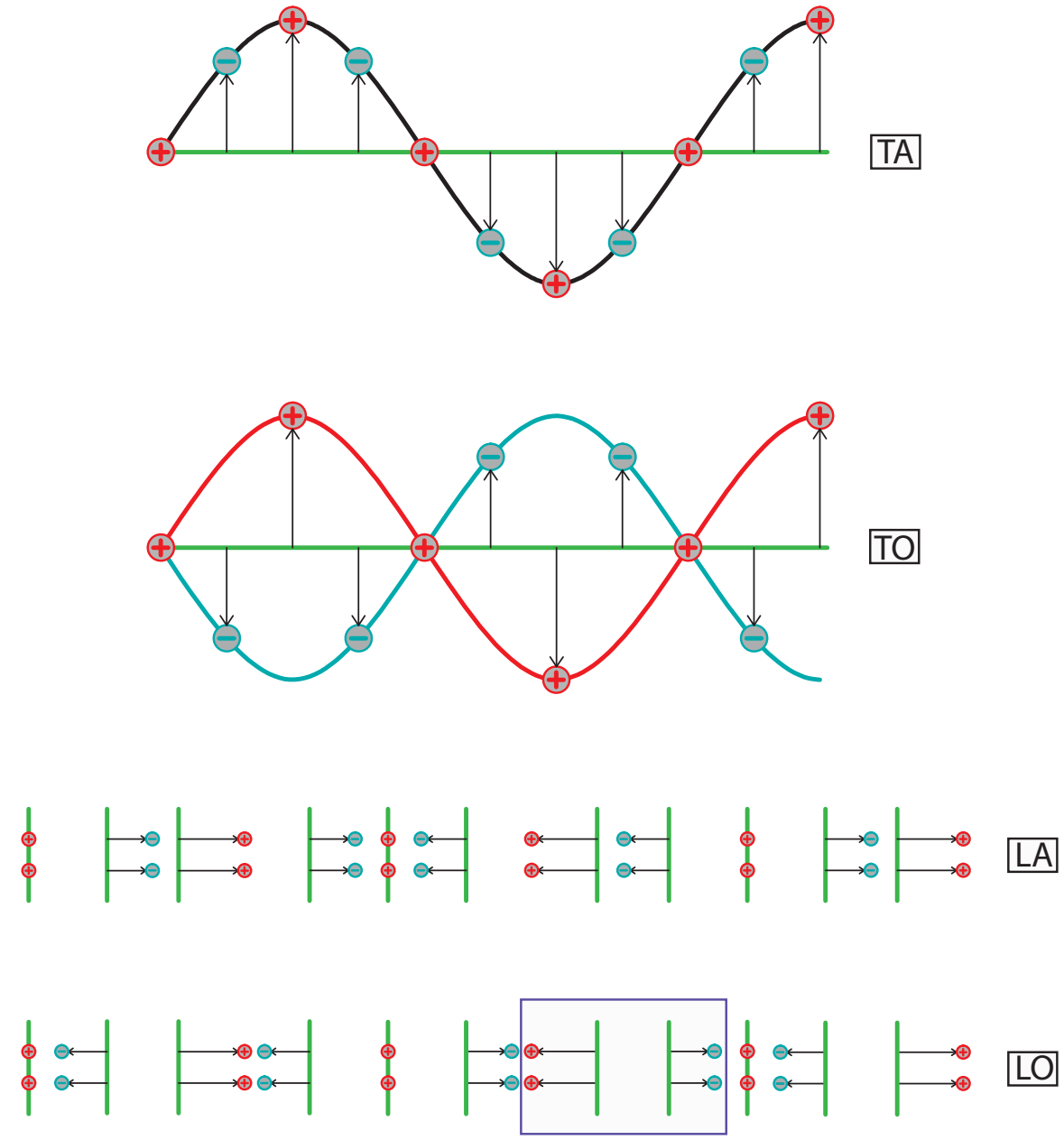

Figure 2.6: Comparison of the displacements of ions in a diatomic lattice within different types of phonon modes. Positive ions are shown in red, while blue is used for the negative ions. The ionic equilibrium positions are indicated by the green lines, and displacements from this position are indicated by the black arrrows. Transverse acoustic (TA), transverse optical (TO), longitudinal acoustic (LA) and longitudinal optical (LO) phonons are shown. For the TA and TO phonon modes, only one row of ions is shown, but two rows are shown for the LA and LO phonon modes in order to highlight that in LO phonons, the separation between vertical planes of oppositely-charged ions is changed in a manner analogous to pulling apart the plates of a parallel-plate capacitor. This results in a longitudinal electric field which causes the Fröhlich interaction between LO phonons and electrons.

Despite the importance of electron-phonon interactions to the optoelectronic properties of these materials, currently no clear picture has emerged of which mechanisms are active. To address this issue, a number of studies have examined the temperature-dependence of the charge-carrier mobility μ. Charge-carrier scattering with low-energy acoustic phonons can relatively easily be quantified by considering the distribution function of a nondegenerate electron gas approximated by a Boltzmann distribution, which gives the probability that a particular state with energy E_k is occupied at any temperature T. Such calculations result in predicted variations in mobility following $\mu \propto T^{-3/2}$ for acoustic phonon deformation potential scattering [98, 99], and $\mu \propto T^{-1/2}$ for acoustic phonon piezoelectric scattering [17]. For Fröhlich interactions between charges and LO phonons analytical solutions are harder to establish [100], but the reduction in LO phonon occupancy with decreasing temperature similarly leads to an increase in charge-carrier mobility in polar semiconductors [17]. Even for non-polar semiconductors such as silicon, electron-phonon interactions are found to be complex, for example involving higher order phonon terms and intervalley scattering [101]. In $MAPbI_3$, μ has been found [58, 102–104] to scale with T^m with m in the range between -1.4 and -1.6. Several groups [64, 96, 104] therefore proposed that electron-phonon coupling at room temperature is almost solely governed by deformation potential scattering with acoustic phonons, which is known [17, 98] to theoretically result in $\mu \propto T^{-3/2}$. While such behaviour may be adopted by non-polar inorganic semiconductors such as silicon or germanium [17, 99], it would be extremely unusual for perovskites that exhibit polar [105, 106] lead-iodide bonds. These findings have therefore raised the puzzling question of why such hybrid perovskites appear to evade the Fröhlich interactions between charge-carriers and polar longitudinal optical (LO) phonon modes that normally govern polar inorganic semiconductors, such as GaAs [17, 107], at room temperature.

2.7 Traps in MHPs

MHPs are most renowned for their successful implementation in solar cells, but perovskite light-emitting diodes [108, 109] and lasers [69] are also attracting intense research attention. In order to operate efficiently, these devices all require high rates of radiative recombination compared with non-radiative recombination. Therefore, future development will require the understanding and reduction of competing processes [110], such as the trap-mediated recombination of charge carriers. Sub-bandgap trap states limit the open-circuit voltage in perovskite solar cells [111], and can act as non-radiative recombination centres, leading to shorter charge-carrier lifetimes [112] and will limit device efficiencies to below the Shockley-Queisser limit [113, 114]. For example, the relatively low open-circuit voltage of Cu_2ZnSnS_4 (CZTS) solar cells has been attributed to the presence of deep traps [115].

Despite a wide range of experimental [58, 68, 77, 112, 116, 117] and theoretical [115, 118, 119] evidence for the presence of trap states in hybrid perovskites, their causes and nature are still largely unknown [111, 120]. In particular, it is unclear whether such traps form energetically discrete crystallographic defect levels [68, 77, 121], or instead comprise a distribution of states arising e.g. from structural disorder [122, 123]. Computational simulations have predicted the energies of point defects, and their presence has been inferred from the fluence-dependence of photoluminescence (PL) decays [68, 117]. However, the observation of an exponential onset (Urbach tail) in the absorption spectrum of methylammonium lead triiodide perovskite ($MAPbI_3$) [122, 124, 125] is indicative of a disordered system in which the position of the band edges varies spatially or temporally, resulting in potential minima which form a tail of trap states [126], as shown in Fig. 2.7. It has been suggested that the manifestation of traps in hybrid perovskites is influenced by their composition [72, 127] and fabrication method [128, 129]. Thus,

knowledge of the physical origin of the traps would aid efforts to reduce their density and depth in order to improve device performance.

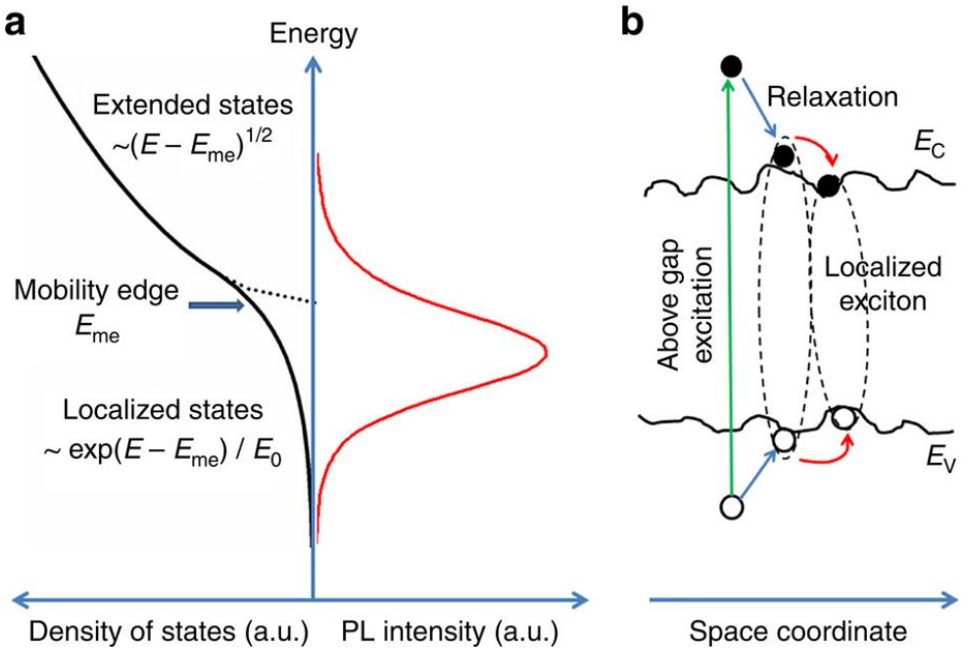

Figure 2.7: Schematic of a band tail of excitonic trap states. **(a)** shows the density of states, with the band tail of localised states approximated by an exponential function up to the mobility edge E_{me}, above which excitons may transition to extended states, approximating free excitons. Under low excitation, mostly the localised states are occupied, and this is where PL emission is observed from, as shown by the red spectrum. In **(b)**, the localised band tail states are shown in space coordinates. Local fluctuations in the band edge potential can trap electrons and holes to form localised excitons. Taken from Ref. [123], used under a Creative Commons Attribution 4.0 International License.

2.8 Double perovskites

Double perovskites (also known as elpasolites or ordered perovskites) are class of perovskite in which neighbouring B sites in the perovskite lattice are occupied by alternately monovalent (B') and trivalent (B") metal cations, such that their general formula is $A_2B'B"X_6$ and their crystal structure (known as rock salt ordering [130]) is as shown in Fig. 2.8 [131, 132]. Attempts to homovalently replace the lead in ABX_3 perovskites in order to avoid the environmental and health risks associated with lead (which is toxic, bio-accumulative and carcinogenic, as mentioned above) have been faced with issues of poor

thermal- and air-stability, and low PCEs [133, 134]. Metal halide double perovskites open up a relatively large compositional space, and so have recently attracted research attention as possible lead-free alternative MHPs, [130]. Volonakis *et al.* computationally screened hypothetical metal halide double perovskites $Cs_2B'B''X_6$ compounds with B' = Cu, Ag or Au, B" = Bi or Sb, and X = Cl, Br or I [135]. They predicted that these compounds would have low carrier effective masses (a predictor of high carrier mobility [136]), and have band gaps in the visible range: both desirable characteristics for solar cells. Unfortunately, the compounds were all predicted to be indirect bandgap semiconductors [135].

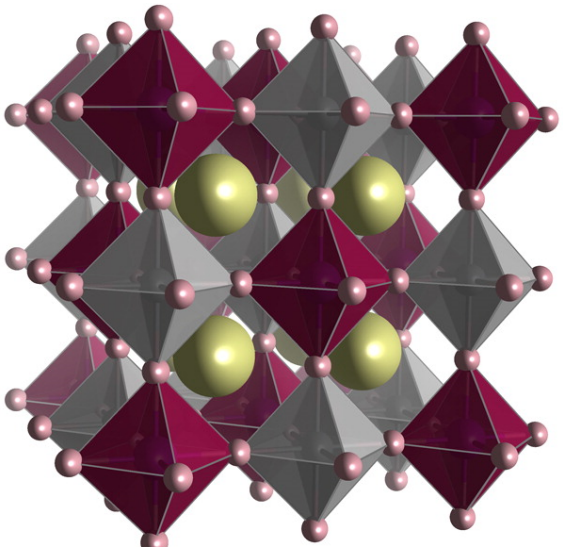

Figure 2.8: Structure of the double perovskite, $Cs_2AgBiBr_6$. Cs is shown in yelllow, Br is pale pink, $BiBr_6$ octahedra are dark red and $AgBr_6$ octahedra are grey. Taken from Ref. [137] with the permission of the American Chemical Society, to whom further permissions related to the material excerpted should be directed.

Indirect bandgaps imply weak oscillator strengths for light absorption and radiative recombination, and hence require a thicker absorber layer (as with silicon solar cells [47]) to sustain a given photocurrent, which is undesirable for thin film solar cell application, especially if the charge-carrier mobilities are low [138]. When synthesis has proven possible (Cu does not crystallise in the correct coordination for a double perovskite [130]) or desirable (Au is significantly more expensive than Ag [130]), experiments have tended to confirm the presence of an indirect bandgap, e.g. in $Cs_2AgBiBr_6$ and $Cs_2AgBiCl_6$

[139, 140] and only modest PCEs, not exceeding 2.5 % in the case of $Cs_2AgBiBr_6$ [141]. Notably, $Cs_2AgInCl_6$ has been synthesised and found to have a direct gap, but at 3.3 eV it is too large for single junction solar cell applications [130, 138]. Nonetheless, it may be possible to shift this material's bandgap into the visible range by substituting some Br for Cl [138]. The direct-gap materials $(MA)_2TlBiBr_6$ [142] and $Cs_2(Ag_{1-a}Bi_{1-b})Tl_xBr_6$ [143] have also been synthesised, with suitable bandgap energy of 2.16 eV and 1.5 eV respectively. However, thallium is even more toxic than lead [144]. Alternatively, it has been proposed that non-toxic direct gap metal halide double perovskites could be achieved by breaking crystal symmetry to permit an otherwise forbidden direct transition [135]. Even without a direct bandgap, metal halide double perovskites have shown promise as X-ray detectors with a low detection limit [145, 146].

2.9 Summary

The topics covered above are revisited in the following chapters. Firstly, the technique of PL spectroscopy, described in Chapter 3, is used to obtain information about the factors which influence electronic motion and recombination in MHPs through the theory and fitting techniques explored in Sections 2.3 and 2.4. Chapter 4 investigates how the electron-phonon coupling interactions discussed in Section 2.6 vary with the chemical composition of the MHP, as detailed in Section 2.1. Meanwhile Chapter 5 is heavily concerned with the identification of traps in $FAPbI_3$, and draws on the existing literature knowledge of traps in MHPs from Section 2.7 and the PL fitting methods in Section 2.4 to do so. Finally, Chapter 6 uses the introduction to double perovskites in Section 2.8 as a foundation for elucidating the optoelectronic and structural properties of $Cs_2AgBiBr_6$.

3
Experimental methods

Most of the results in this thesis were obtained using photoluminescence (PL) spectroscopy techniques. In these experiments, the sample is excited by a laser and the resultant emitted light is observed either spectrally or temporally, here mostly using a gated intensified (iCCD) CCD camera. In an iCCD, the PL signal is amplified by an intensifier before being detected by a charge-coupled device (CCD). Switching the intensifier on and off allows temporal sampling of the signal. For shorter time scales, time-correlated single photon counting (TCSPC) can be used: this technique detects one photon at a time and reconstructs the time dependence of the PL from a histogram of the photon arrival times.

This chapter discusses both techniques in detail: first detailing their operating principles, then the set-ups used for the experiments in this study, and lastly the means by which they were calibrated. A Fourier-transform infrared (FTIR) spectrometer was used to obtain absorption spectra for the samples used in Chapter 6, and so this chapter also outlines this supplementary technique. Finally, the techniques used by collaborators to produce samples are summarised.

3.1 Photoluminescence spectroscopy

Photoluminescence spectroscopy is the study of the non-equilibrium electromagnetic radiation emitted by a material after it has been excited by light [147]. Electrons in the material are excited to higher energy states upon absorbing this light, and return to their ground states via recombination processes, which may be radiative or non-radiative. Thus, photoluminescence (PL) provides information about the electronic energy states in the material and the electronic processes competing with PL emission. Although PL does not directly contribute to current generation in solar cells, it can be used to indicate photovoltaic efficiency because radiative recombination is the reverse process of light absorption [13]. For these reasons, PL spectroscopy is well-suited to investigating the factors which influence electronic motion and recombination in MHPs, and was the principal experimental technique used to obtain results in this thesis.

In these experiments, the excitation was provided by a laser which delivers a continuous or pulsed beam. Continuous excitation is the more analogous to solar illumination, and allows the measurement of steady-state PL spectra, while pulsed excitation allows the PL to be time-resolved. Since the electronic processes of interest to this study (diffusion, trapping and recombination) occur over timescales ranging from picoseconds to milliseconds, it was necessary to employ two different techniques for measuring the PL with different degrees of temporal resolution: TCSPC up to the nanosecond timescale, and iCCD spectroscopy beyond this. Both techniques allow the PL to be mapped in time by varying the timing of the detection window with respect to the arrival of the excitation pulse at the sample.

3.1.1 Gated intensified iCCD spectroscopy

The charge-coupled device is the basis for the digital imaging systems widely used in telescopes and digital cameras today, but cannot achieve a frame rate faster than

around $\sim 10^6$ frames per second (fps) alone [148]. The frame rate of an imaging system is the inverse of the time taken for an image to be acquired and read out [149]. In order to obtain higher temporal resolution, gated intensified CCD (iCCD) cameras utilise an image intensifier in front of a CCD to amplify the light signal, so reducing the acquisition time. Furthermore, the intensifier may be operated by a fast optical shutter, bypassing the limit imposed by the readout time of the CCD to sample light on timescales as low as two nanoseconds [150].

The operation of an iCCD is depicted in Fig. 3.1: photons are converted to electrons, which are easier to multiply, before being converted back to photons before arriving at the CCD. Incident photons enter the image intensifier tube and land on the photocathode, causing a photoelectron to be released. When the intensifier is 'gated' on, the photoelectrons are attracted to the microchannel plate (MCP) by an electric field. The MCP may also be gated "off" by being held at a negative voltage relative to the photocathode, in which case photoelectrons cannot reach the MCP and no signal is observed. The MCP consists of a honeycomb of glass channels around 10 μm across, with a resistive coating, through which the photoelectrons are accelerated by a large electric field [150]. Photoelectrons of sufficient energy will generate secondary electrons from collisions with the channel walls, which are also accelerated across the MCP. In this way, an electron gain is produced which is dependent on the voltage across the MCP. Upon exiting the MCP, the resultant electron cloud is further accelerated towards a phosphor by a high voltage, whereupon photons are released: many more than were initially incident on the photocathode. These photons are coupled by a fibre optic to the CCD, where they land on an array of capacitive bins which accumulate charge in proportion to the number of photons that were incident on them. At the end of the exposure time, the accumulated charge is sequentially shifted along the array and read out as a voltage, which digitally encodes the image that was incident on the CCD [151].

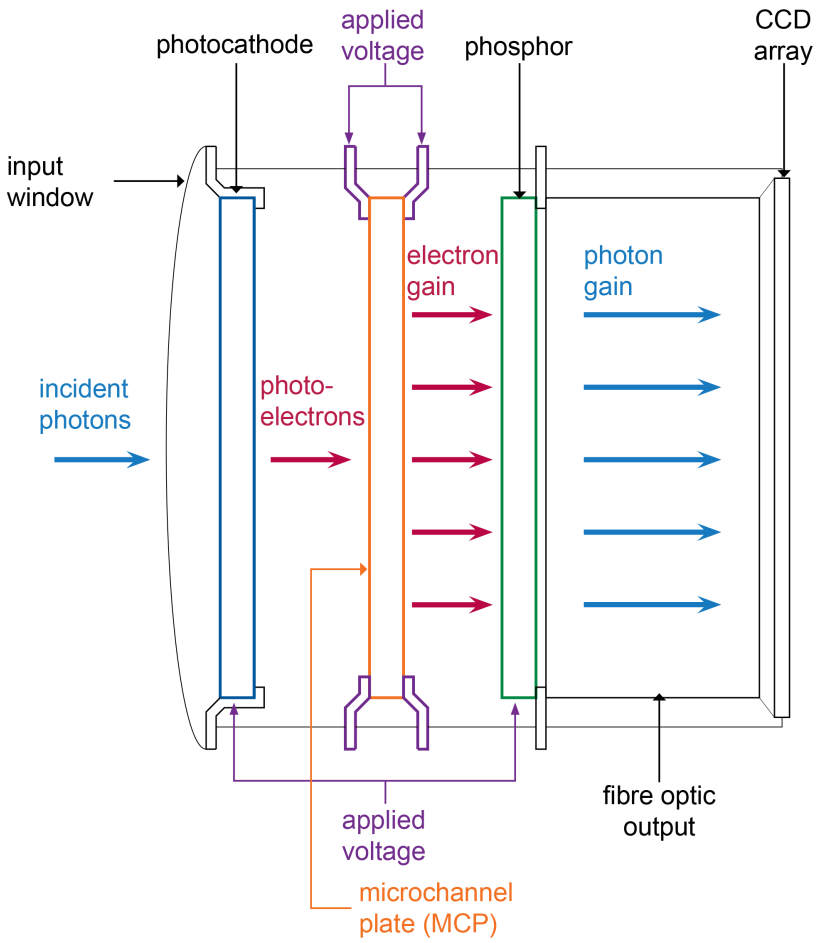

Figure 3.1: Schematic diagram of the operation of the image intensifier tube in an iCCD. Photons generate photoelectrons, which are multiplied before generating photons, thus amplifying the signal. The intensifier may be gated "off" by reversing the voltage of the MCP with respect to the photocathode, allowing for temporal sampling of the signal.

The principal advantages of iCCDs therefore lie in their light sensitivity and gateability. Due to signal amplification in the intensifier, the noise of the camera is no longer dominated by the readout noise inherent to the CCD, allowing detection of single photons. Meanwhile, by varying the gate timing and duration, the time-dependence of an optical signal may be measured at a resolution dependent on the gating rate. By repetitively gating the intensifier, the amplified signal may further be enhanced by being cumulatively detected on the CCD over many gating cycles before being read out. However, the possible number of accumulations is limited by the charge capacity of individual CCD pixels, which will eventually saturate and spill over into neighbouring pixels ('blooming'), resulting in image artefacts. The benefits conferred by coupling an intensifier to a CCD do however come at the cost of lower spatial resolution [150].

3.1.2 Time-correlated single photon counting

TCSPC is a spectroscopic technique capable of measuring weak light signals with a time resolution as low as tens of picoseconds, under pulsed excitation [152]. Whereas the temporal resolution of ordinary transient electronic recorders (such as iCCD cameras) is determined by how often they can sample the signal within a single excitation cycle, and thus is limited by factors such as the rise-time of the detector or the electronic sampling rate of the analogue-to-digital converter [61], TCSPC depends only on timing the detection of a single photon per excitation cycle [153]. The time resolution of TCSPC is then limited by only by the spread of the transit times of the photon pulses in the detector, rather than the rise-time of the detector, since single-photon detection relies only on the detector registering a signal above a specific threshold value [152]. Furthermore, single photon detection greatly reduces the computational processing effort required per excitation cycle, with the added benefit of avoiding gain noise (random variations in the amplification of analogue photodetectors) and reducing the electronic noise to the level of

shot noise [152]. Using TCSPC, the decay profile of a weak signal may be reconstructed from single-photon detection events over multiple excitation cycles [153].

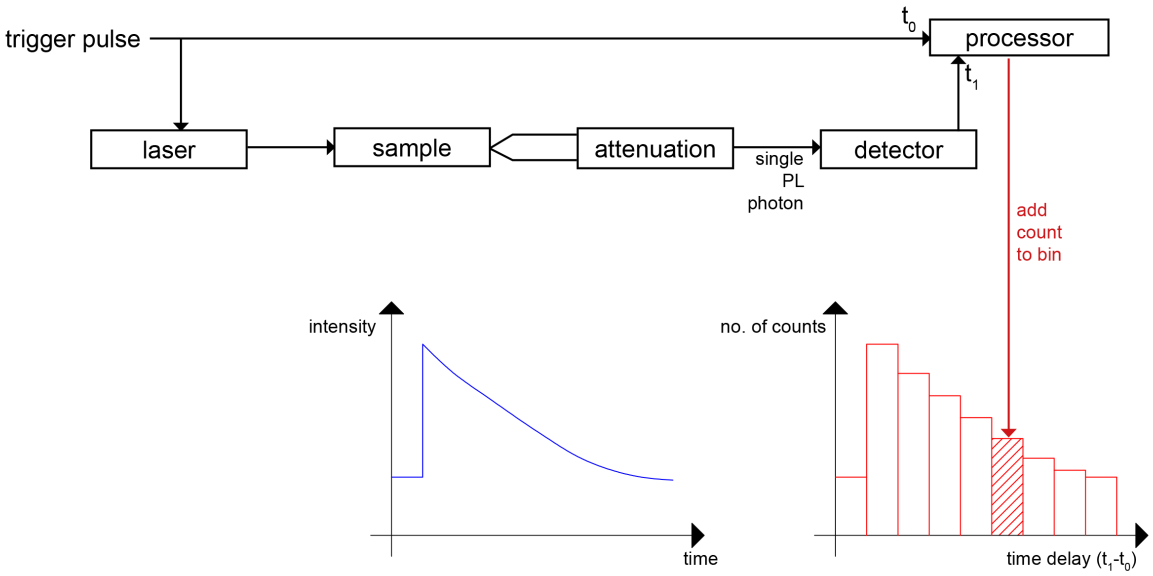

Figure 3.2: Schematic diagram of the principles of TCSPC. The arrival time of a PL photon t_1 is referenced against an initial trigger pulse at time t_0. The technique requires that at most one photon be detected per excitation period, which may require PL signal attenuation. After many excitation periods, a histogram of PL photon time delays $t_1 - t_0$ is built up, reproducing the true PL decay profile.

The operating principles of TCSPC are illustrated in Fig. 3.2. A repetitive electrical signal is split into two: one part triggers a laser pulse, which photoexcites the sample, while the other is passed to a constant fraction discriminator (CFD) within the processor. The arrival of the electrical pulse at time t_0 is measured by the CFD, which starts a time-to-amplitude converter (TAC): this generates a voltage which increases linearly with time [154]. Meanwhile, the arrival of the first photon of the PL is registered by a detector such as a MCP, photomultiplier tube (PMT) or single photon avalanche diode (SPAD), and the timing of detection t_1 is sent to the processor. This time is referenced against the time of arrival of the initial trigger pulse by stopping the voltage ramp of the TAC, producing a voltage proportional to the time delay $t_1 - t_0$ between the detection of the photon and the trigger pulse. A histogram of PL photon arrival time per time

bin is thus built up as more excitation cycles occur. Critically, TCSPC relies on the PL light intensity being sufficiently low at the detector that it is negligibly unlikely that more than one photon is detected per excitation cycle; if necessary, this condition can be ensured by attenuating the PL. Consequently, after a large number of excitation cycles, the histogram accurately represents the true photon distribution of the PL signal with time. If more than one photon were to arrive at the detector per cycle, only the first would be registered and so the histogram would suffer from a bias towards photons with shorter arrival times, which is known as 'pile-up' [153]. Therefore, the probability of a photon being detected per cycle is usually kept below 1 % [153].

The timing precision of a TCSPC system is characterised by its Instrument Response Function (IRF), which is the function the system records if detecting the laser pulse directly [152]. In an ideal system, this would be infinitely thin, with deviations from ideality resulting in a broader IRF. Usually, the main source of IRF broadening is the uncertainty in the photon registration time introduced by the detector as it converts the photon into an electrical pulse, followed by jitter in the synchronisation signal at the excitation source [153]. The PL signal recorded by the TCSPC system is in fact the convolution of the true PL decay with the IRF [152]. Deconvolution can recover PL lifetimes down to a tenth of the IRF full-width at half-maximum (FWHM) [153] but is not necessary when considering timescales far in excess of this.

One disadvantage of TCSPC is that the requirement of a low photon detection rate per cycle means that it can be a slow technique. Increasing the trigger repetition rate increases the speed of measurement, at the cost of reducing the time window available for detection between laser pulses. Measurement of PL at long delay times after excitation may therefore lead to long acquisition times.

3.1.3 PL experimental details

The PL spectroscopy experiments for this thesis were conducted on a single bench, with different detectors used for the iCCD and TCSPC measurements, as shown in Fig. 3.3. The samples were photo-excited by a 398 nm picosecond pulsed diode laser (PicoHarp, LDH-D-C-405M). A 400 nm bandpass filter was placed after the laser to cut off longer-wavelength parasitic emissions. The laser beam was attenuated as necessary by neutral density (ND) filters and focused onto the sample by a convex lens with focal length 250 mm, with an iris diaphragm used to control the laser spot size (measured to be 5.8 $\times 10^{-4}$ cm^2) and maintain a circular beam profile. Between measurements, the laser was blocked by an electronic shutter. The resultant PL from the sample was collected by a collimating lens with focal length 250 mm and passed through a linear polariser to avoid Wood's anomalies from the diffraction gratings later in the beam path, followed by a longpass interference filter to prevent laser scatter from reaching the detectors. Further ND filters were placed in the path of the PL if necessary to attenuate the signal to avoid saturation at the detector, or to ensure the low photon detection probability required for TCSPC. Depending on the position of a retractable mirror, the PL signal was then coupled into a grating spectrometer (Princeton Instruments, SP-2558), which either directed the spectrally dispersed PL onto an iCCD (PI-MAX4, Princeton Instruments) or to a photon-counting detector (a PDM series Single Photon Avalanche Diode (SPAD) from MPD), whose timing was controlled with a PicoHarp300 TCSPC event timing processor.

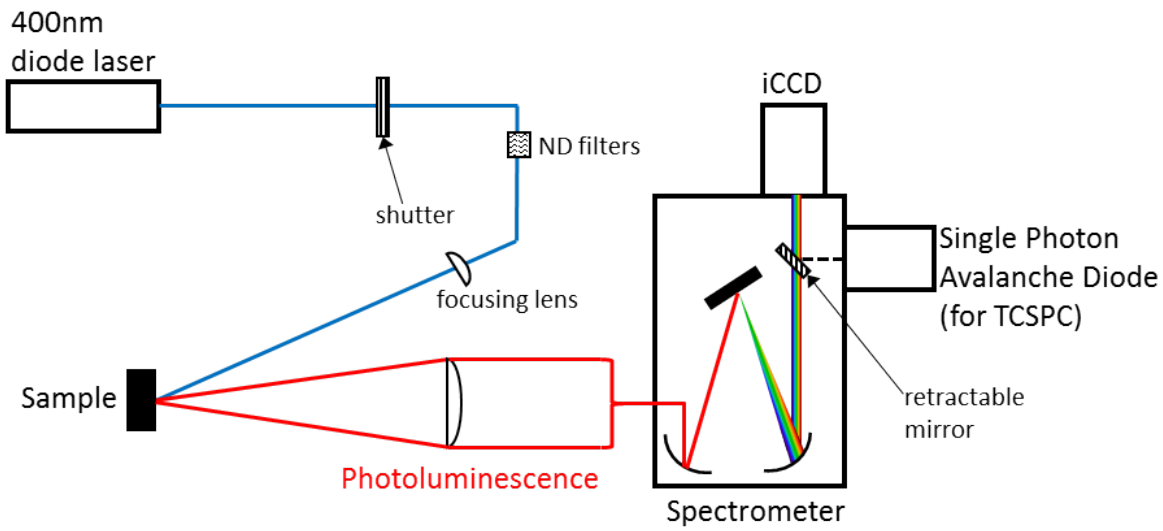

Figure 3.3: Schematic diagram of photoluminescence spectroscopy setup. The PL is collimated and focused by lenses into the spectrometer, which spatially separates the wavelengths in the PL. The spectrally separated PL may be directed onto the iCCD or SPAD depending on the position of a retractable mirror.

For the temperature dependent measurements in Chapters 4 and 5, each sample was mounted under vacuum ($P < 10^{-6}$ mbar) in a cold-finger liquid helium cryostat (Oxford Instruments, MicrostatHe). An associated temperature controller (Oxford Instruments, ITC503) monitored the temperature at two sensors mounted on the heat exchanger of the cryostat and the end of the sample holder, respectively; the reading from the latter was taken as the sample temperature. Meanwhile the data in Chapter 6 was obtained with the sample mounted in a gas-exchange helium cryostat (Oxford Instruments, OptistatCF2). The bandgap of MHPs has been found to shift with illumination during other PL studies in which a single sample spot was exposed to a laser for an extended period of time [155]. In between measurements at successive temperatures for this thesis, the sample was moved such that a fresh spot was illuminated each time, with the aim of avoiding such effects. Repeated experiments in which the PL was measured from low to high temperatures reproduced consistent temperature-dependent trends of the PL spectra for a given material, regardless of whether a sample was re-measured or a fresh sample

was used. In particular, discontinuities were not apparent in the data in Fig. 5.3b and c, which were obtained by varying the excitation fluence at each temperature step during a single experiment. Drifts in the PL signal with exposure time were thus not apparent. Such shifts have been proposed to result from mechanisms involving the diffusion of molecules or ions [155], in which case they would not be significant for the experiments on the time- and power-dependence of PL in this thesis, which were all performed at cryogenic temperatures.

The iCCD was used to capture PL spectra. Under continuous-wave laser excitation, the iCCD recorded steady-state PL spectra. Under pulsed laser excitation, the iCCD could either record time-integrated PL spectra over many excitation cycles, or the time evolution of the PL spectra by varying the time delay at which the intensifier was gated on relative to the arrival of the laser pulse at the sample. At longer delay times, the PL signal decreased in intensity and so the intensifier was concomitantly gated on for longer. Meanwhile TCSPC was used to capture PL transients, particularly at the wavelength of peak PL emission as determined by the iCCD. However, by varying the central wavelength of the diffraction gratings, it was also possible to measure the time-evolution of the PL spectral profile using TCSPC.

3.1.4 System calibration

Ahead of performing spectral and time-dependent measurements, a number of calibrations had to be made. Firstly, the spectrometer had to undergo wavelength calibration with respect to what was detected by the iCCD and SPAD. The response of the iCCD to an Ocean Optics HG-1 Mercury Argon Calibration Source was used to calibrate the wavelength of light incident on each CCD pixel under the diffraction grating settings used in the experiments. Meanwhile, the response of the SPAD was calibrated against a Spectra-Physics 155 Helium Neon laser emitting at a wavelength of 632.8 nm.

Secondly, the spectral response of the detectors in the experimental setup was determined by comparing their measured response to a Gooch & Housego OL 254U Lamp with known emission spectrum. Thus, where the measured lamp spectrum was relatively higher than the true emission spectrum, the measured PL spectra had to be reduced, such that

$$I_{\mathrm{sc}}^{\mathrm{PL}}(\lambda) = I_{\mathrm{m}}^{\mathrm{PL}}(\lambda) \times \frac{I_{\mathrm{t}}^{\mathrm{lamp}}(\lambda)}{I_{\mathrm{m}}^{\mathrm{lamp}}(\lambda)} \tag{3.1}$$

where $I_{\mathrm{sc}}^{\mathrm{PL}}$ is the spectrally corrected PL spectrum, $I_{\mathrm{m}}^{\mathrm{PL}}$ is the measured PL spectrum, $I_{\mathrm{t}}^{\mathrm{lamp}}$ is the true lamp spectrum and $I_{\mathrm{m}}^{\mathrm{lamp}}$ is the measured lamp spectrum.

The effect of the post-sample ND filters on the PL was determined separately by measurement of their transmission spectra using a PerkinElmer Lambda 1050 UV/NIS/NIR spectrometer. By dividing the measured PL spectrum by the transmittance(s) of the ND filter(s) in the beam path, the shape and intensity of the spectrum without the effect of the ND filter(s) could be restored.

Finally, the instrument response function of the SPAD was determined by placing a roughened quartz disc in the sample position and measuring the detector response to the scattered light from the incident laser. Since the FWHM of the IRF was less than 0.5 ns, it was judged that deconvolution of the measured PL signals would not produce a significantly more accurate PL trace over the timescales of the PL decays, which typically had lifetimes over 10 ns.

3.2 Absorption spectroscopy

As mentioned above, absorption is a closely related process to emission and so absorption spectroscopy provides complementary information to PL spectroscopy. Whereas PL spectroscopy gives information about charge-carrier energy levels and lifetimes in a material based on the timing and energy of the photons emitted by recombining

charge-carriers, absorption spectroscopy measures the wavelength-dependent absorption characteristics of a material. Energetic transitions ranging from lattice vibrations to core-shell electrons can be detected in absorption spectra, and it is often used to identify substances by their unique absorption characteristics. In this study however, absorption spectroscopy is used in a limited capacity to find the energies associated with excitonic, direct gap and indirect gap transitions in bismuth-silver double perovskites, as detailed in Chapter 6. Notably, the peak energy of absorption is typically higher than that of emission, by an energy known as the Stokes shift [154], which arises from the relaxation of photoexcited electrons to the conduction band minima by phonon emission, before recombining radiatively.

3.2.1 Determining the absorbance

The absorption of a material can be quantified by its absorbance, also known as 'optical density'. The absorbance, A is defined by

$$A = -\log_{10}\left(\frac{I}{I_0}\right) \tag{3.2}$$

where I is the transmitted light intensity and I_0 is the light intensity at the sample surface [156]. Therefore, the most simplistic method of measuring the absorbance spectrum of a sample would be to measure the spectrum of a light source before and after having placed the sample between the source and detector, the former and latter measurements giving approximations to I_0 and I respectively. This is known as dispersive spectroscopy. However, a more sophisticated approach requires accounting for the light reflected by the sample surface: the absorbance is only meaningful if calculated from the *internal* transmittance, i.e. the light intensity which passes through the sample as a fraction of that which first started propagating through the sample. Since the internal transmittance

cannot be directly measured, the (external) transmittance T and reflectance R spectra of the sample must be measured instead, where $T = {}^{I_{\text{transmitted}}}/_{I_0}$ and $R = {}^{I_{\text{reflected}}}/_{I_0}$. Then,

$$A = -\log_{10}\left(\frac{T}{1-R}\right) \tag{3.3}$$

In order to determine the true T and R of a sample, the measured spectra must be referenced against the source spectra. For transmission, the reference spectrum is T_{blank}, the measured transmittance with no sample in the beam path, while for reflection a mirror of known reflectance is put in place of the sample, to obtain R_{mirror}. T_{mirror} and R_{blank} meanwhile serve as transmittance and reflectance backgrounds respectively, so that

$$T = \frac{T_{\text{measured}} - T_{\text{mirror}}}{T_{\text{blank}} - T_{\text{mirror}}} \tag{3.4}$$

$$R = \frac{R_{\text{measured}} - R_{\text{blank}}}{R_{\text{mirror}} - R_{\text{blank}}} \times \rho_{\text{mirror}} \tag{3.5}$$

where ρ_{mirror} is the reflectance of the mirror. While this approach does not account for scattering or inhomogeneities in the sample, nor multiple reflections, it provides a first-order route to the absorbance.

3.2.2 Fourier-transform infrared spectroscopy

Whereas dispersive spectrometers operate by measuring the absorbance of a sample at individual frequencies sequentially, Fourier Transform Infrared (FTIR) spectrometers shine light of many frequency components through the sample. By tracking the effect of the sample on the incident light as the intensity distribution of the frequency components of the light is varied, the absorbance spectrum of the light can be deduced.

In detail, an FTIR spectrometer consists of an infrared source, an interferometer, and a detector. Typically, the interferometer is a Michelson interferometer, as shown in Fig. 3.4a [157], which consists of a beamsplitter, and two mirrors, one of which can be

precisely translated. The source radiation is divided into two beams by the beamsplitter: one half is transmitted, the other half is reflected. The moving and fixed mirrors respectively reflect the two beams back towards the beamsplitter, whereupon half of each beam continues on through the sample and then to the detector. Depending on the optical path difference (the difference in the distance travelled, accounting for the refractive index of the propagation medium) between the two beams, the light intensity measured by the detector will change due to variation in the interference between the two beams. The distribution of intensities measured by the detector as the movable mirror is translated is known as the interferogram.

A monochromatic light source would result in a simple sinusoidal interferogram, but for the broadband light source used in FTIR spectroscopy, each frequency component in the source contributes a sinusoid to the interferogram. By applying a Fourier transform to the interferogram, its frequency components can be extracted to produce its spectrum. The absorption of a sample will modulate the frequency components found in the interferogram and hence the spectrum it produces. Thus, just as in dispersive spectroscopy, the absorbance of the sample can be deduced by measuring its transmittance and reflectance, albeit via the effect of the sample on the interferogram of transmitted and reflected light (as shown in Fig. 3.4b). A Helium-Neon laser may be directed along the same path as the infrared source in order to act as a reference, from which the position and velocity of the movable mirror may be determined.

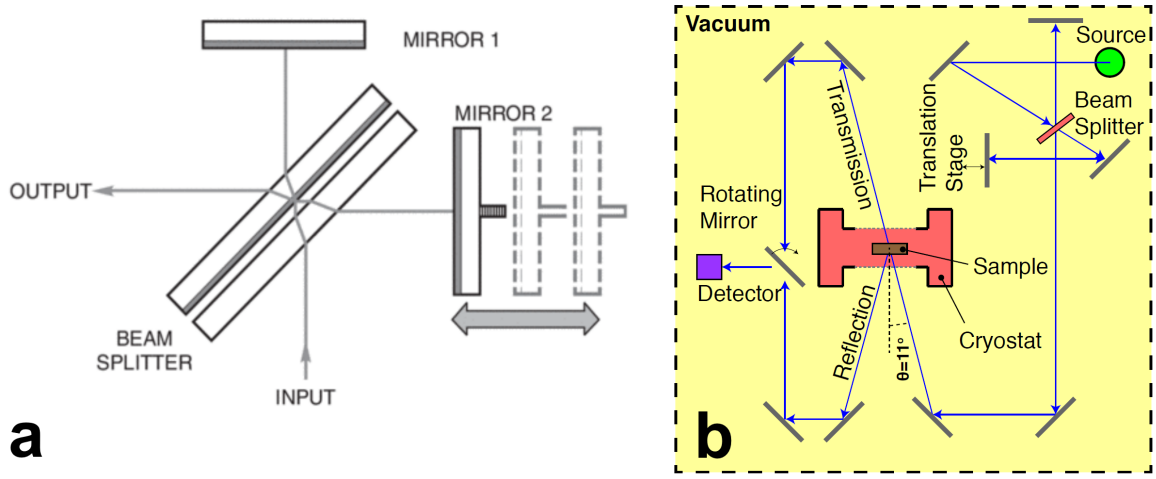

Figure 3.4: Schematic diagram of the operation of an FTIR spetcrometer. In **(a)**, the operation of a Michelson interferometer is shown, taken from Ref. [157]. A beamsplitter divides light from an input source into two beams, which are both reflected back towards the beamsplitter and interfere with each other. Moving one mirror changes the path length difference between the two beams, changing the light intensity at the output detector. **(b)** (taken from Ref. [55], used under a Creative Commons Attribution 4.0 International License) depicts the FTIR setup used in the absorbance spectroscopy experiments in Chapter 6, with the sample mounted inside a gas exchange cryostat within the spectrometer.

FTIR spectrometers have several advantages over dispersive spectrometers. Firstly, FTIR spectrometers collect all wavelengths simultaneously, whereas dispersive spectrometers record each wavelength sequentially. This is called the multiplex or Fellgett advantage, and results in an improvement to the signal-to-noise ratio. A further improvement in signal-to-noise ratio arises from the use of a circular aperture to direct the beam in an FTIR spectrometer, rather than narrow entrance and exit slits in the monochromator of a dispersive instrument. This is known as the Jacquinot or throughput advantage, since for a given resolution and wavelength a circular aperture will transmit more light than a slit. Thirdly, the reference laser in FTIR spectrometers allows them to achieve higher wavelength precision (known as the Connes advantage) than allowed by the mechanical movement of diffraction gratings in dispersive instruments. Thus, FTIR spectrometers requires shorter measurement times and achieve a higher signal-to-noise ratio and higher spectral accuracy than dispersive spectrometers [157].

3.2.3 FTIR experimental details

For the absorbance measurements used in Chapter 6, a Bruker Vertex 80 FTIR spectrometer was used, as shown in Fig. 3.4b, configured with a tungsten halogen lamp illumination source, a CaF_2 beamsplitter and a silicon detector. The incident light was angled at 11 degrees to the normal of the sample. The samples were mounted in a gas-exchange helium cryostat (Oxford Instruments, OptistatCF2) and heated over temperatures from 5 to 295 K in increments of 5 K.

3.3 Sample preparation

3.3.1 MA and FA perovskite thin films

[performed by G. E. Eperon, Department of Physics, University of Oxford]

All materials unless otherwise stated were purchased from Sigma-Aldrich and used as received. Methylammonium iodide (MAI), methylammonium bromide (MABr), formamidinium iodide (FAI) and formamidinium bromide (FABr) were purchased from Dyesol. Thin films were prepared on Z-cut quartz substrates. These were initially cleaned sequentially with acetone followed by propan-2-ol, then treated with oxygen plasma for 10 minutes.

MA perovskite films were deposited in a nitrogen-filled glovebox using a 'solvent quenching' method wherein an excess of antisolvent is deposited onto the wet substrate while spin-coating [158]. A 1:1 molar ratio solution of MAX and PbX_2 (X = I, Br) was dissolved in anhydrous N,N-dimethylformamide (DMF) at 1 M. This was then spin-coated onto the quartz substrates at 5000 rpm for 25 seconds. During spin-coating, after 7 seconds an excess of anhydrous chlorobenzene was rapidly deposited onto the spinning film. After spin-coating, films were annealed at 100 °C for 10 minutes.

FA perovskite films were deposited using an acid-addition method to produce smooth and uniform pinhole-free films [80]. FAX and PbX_2 (X = I, Br) were dissolved in

anhydrous N,N-dimethylformamide (DMF) in a 1:1 molar ratio at 0.55 M. Immediately prior to film formation, small amounts of acid were added to the precursor solutions to enhance the solubility of the precursors and allow smooth and uniform film formation. 38 µl of hydroiodic acid (57% w/w) was added to 1 ml of the 0.55 M $FAPbI_3$ precursor solution, and 32 µl of hydrobromic acid (48% w/w) was added to 1 ml of the 0.55 M $FAPbBr_3$ precursor solution. Films were then spin-coated from the precursor plus acid solution on warm (85 °C) oxygen plasma-cleaned substrates at 2000 rpm in a nitrogen-filled glovebox, and subsequently annealed in air at 170 °C for 10 minutes. This heat treatment ensured that films were in the black perovskite phase of $FAPbI_3$, rather than the yellow hexagonal nonperovskite phase. Films continued to appear black throughout the study and showed no signs of yellowing, or a reduction in emission.

3.3.2 $Cs_2AgBiBr_6$ perovskites

3.3.2.1 Single crystals

[performed by L. Schade, Department of Physics, University of Oxford]

Single-crystal samples of $Cs_2AgBiBr_6$ were grown following the crystallization process reported by Slavney *et al.* [21]. The crystals had a thickness of around 1 mm in each direction.

3.3.2.2 Thin films

[performed by G. Longo, Department of Physics, University of Oxford]

Thin films of $Cs_2AgBiBr_6$ were prepared by vapour deposition, using a novel method [159]. They were grown on z-cut quartz substrates to a thickness of 300 nm.

3.4 *Ab initio* calculations

[carried out by C. Verdi, Department of Materials, University of Oxford]

Ab initio calculations were carried out on $MAPbI_3$ in the orthorhombic phase using the crystallographic data in Ref. [160]. The ground-state electronic structure was computed within the local density approximation to density functional theory (DFT) including spin-orbit coupling, as implemented in the `Quantum ESPRESSO` package [161]. The electronic quasiparticle energies were calculated with the SS-GW method described in Ref. [162] using the `Yambo` code [163], and interpolated by means of Wannier functions as in Ref. [164], using `wannier90` [165]. This yields bandgap and effective masses in good agreement with experiment, which is crucial for electron-phonon calculations. In fact, the electron-phonon self-energy at the band edges is very sensitive to the curvature of the bands. The lattice dynamical properties were computed within density functional perturbation theory at the Γ point, as in Ref. [166]. All calculations were performed for the low-temperature orthorhombic structure of $MAPbI_3$, since the vibrational frequencies are relatively insensitive to the structure [166], and the measured PL broadening does not change across the orthorhombic/tetragonal phase transition. In the case of $MAPbBr_3$ the vibrational properties were calculated for the orthorhombic structure, starting from the lattice parameters and atomic coordinates given by Swainson *et al.*[167].

The LO-TO splitting was included through the evaluation of the nonanalytic contribution to the dynamical matrix. The electron-phonon coupling was calculated using the `EPW` code [168, 169], v.4. The electron-phonon self-energy, Σ was evaluated by calculating the electron-phonon matrix elements using the *ab initio* Fröhlich vertex [170] in its simplified form. The calculated Born effective charges and dielectric constants are reported in Table 4.3.

4

Electron-phonon coupling in hybrid lead halide perovskites

Initially published in Ref. [72].

This study clarifies the relative activity of different charge-carrier scattering mechanisms in hybrid lead halide perovskites by investigating charge-carrier scattering through an analysis of the photoluminescence (PL) linewidth as a function of temperature between 10 K and 370 K. By carefully examining the low-temperature regime in which thermal energies fall below those of high-energy LO phonon modes, the competing contributions from charge-carrier interactions with acoustic and optical phonons can be clearly separated. It is therefore possible to show unambiguously that Fröhlich coupling to LO phonons is the predominant cause of linewidth broadening in these materials at room temperature, with scattering from acoustic phonons and impurities being a minor component. Furthermore, excellent agreement is demonstrated between the experimentally determined temperature dependence of the PL linewidth and theoretical values derived from *ab initio* calculations (performed by collaborators) for $MAPbI_3$. To elucidate how charge-carrier–phonon interaction strengths depend on perovskite composition, $FAPbI_3$, $FAPbBr_3$, $MAPbI_3$ and $MAPbBr_3$ were examined, which represent a comprehensive set of the most commonly

implemented organic and halide ingredients in hybrid perovskites. High performing devices have used formulations containing both FA and MA cations in order to counteract the thermodynamic instability of $FAPbI_3$ in its perovskite phase at room temperature [171–173]. Meanwhile, mixed-halide perovskites incorporating both I^- and Br^- have been investigated for use in tandem solar cells [18, 80, 174] as these systems allow for bandgap optimization across a wide tuning range. It is shown that while the choice of organic cation has relatively little effect on the Fröhlich interactions, bromide perovskites exhibit higher Fröhlich coupling than iodide perovskites as a result of their smaller high-frequency values of the dielectric function. Overall, these results conclusively demonstrate that electron-phonon coupling in hybrid lead halide perovskites follows a classic bandstructure picture for polar inorganic semiconductors which are dominated by Fröhlich coupling between charge-carriers and LO phonon modes in the high-temperature regime.

4.1 Experimental details

Thin film samples of $MAPbI_3$, $FAPbI_3$, $MAPbBr_3$ and $FAPbBr_3$ were spin-coated according to the procedure described in Subsection 3.3.1. The samples were mounted under vacuum ($P < 10^{-6}$ mbar) in a cold-finger liquid helium cryostat, and were excited by the laser in pulsed mode with a repetition rate of 10 kHz and a fluence of 490 nJ cm^{-2}. PL measurements were taken using the setup described in Subsection 3.1.3. First-principles calculations of the electron-phonon coupling in $MAPbI_3$ were performed as described in Section 3.4.

4.2 Results

4.2.1 Temperature-dependent photoluminescence spectra

To conduct an analysis of electron-phonon coupling in hybrid lead halide perovskites time-integrated PL spectra of solution-processed $FAPbI_3$, $FAPbBr_3$, $MAPbI_3$ and $MAPbBr_3$

thin films were recorded over temperatures from 10 K to 370 K in increments of 5 K (Fig. 4.1). As discussed in Subsection 4.2.2.1, these spectra likely represent recombination of free carriers, except at the very lowest temperatures. The observed PL peak positions at room temperature are consistent with those reported previously for these materials [63, 73, 80, 175, 176]. The colour plots in Fig. 4.1 exhibit abrupt shifts in PL peak energies at various temperatures that are associated with phase transitions commonly found in these relatively soft materials. For example, $MAPbI_3$, $MAPbBr_3$ and $FAPbI_3$ have been reported to undergo a phase transition from an orthorhombic to a tetragonal structure between 130 and 160 K [63, 176, 177]. A further phase transition to the cubic phase follows at higher temperatures for the MA perovskites (at approximately 330 K for $MAPbI_3$ [63, 177] and 240 K for $MAPbBr_3$ [177]), while a transition to a trigonal phase occurs at around 200 K for $FAPbI_3$ [63]. The lower-temperature phase transition to the orthorhombic phase below $130-160\,\mathrm{K}$ is generally associated with larger energetic shifts as it marks a strong reduction in the extent of rotational freedom of the organic cation [160, 177, 178]. Higher-temperature structural changes are more subtle in this regard and therefore much harder to discern [58]. Apart from these discontinuities, the PL peak in all four materials shifts continuously towards higher energy with increasing temperature. This general trend is in contrast to that of typical semiconductors such as Si, Ge and GaAs, for which the bandgap decreases with temperature as a result of lattice dilation [99, 179]. The atypical positive bandgap deformation potential of hybrid lead halide perovskites has been attributed to a stabilisation of out-of-phase band-edge states as the lattice expands [180].

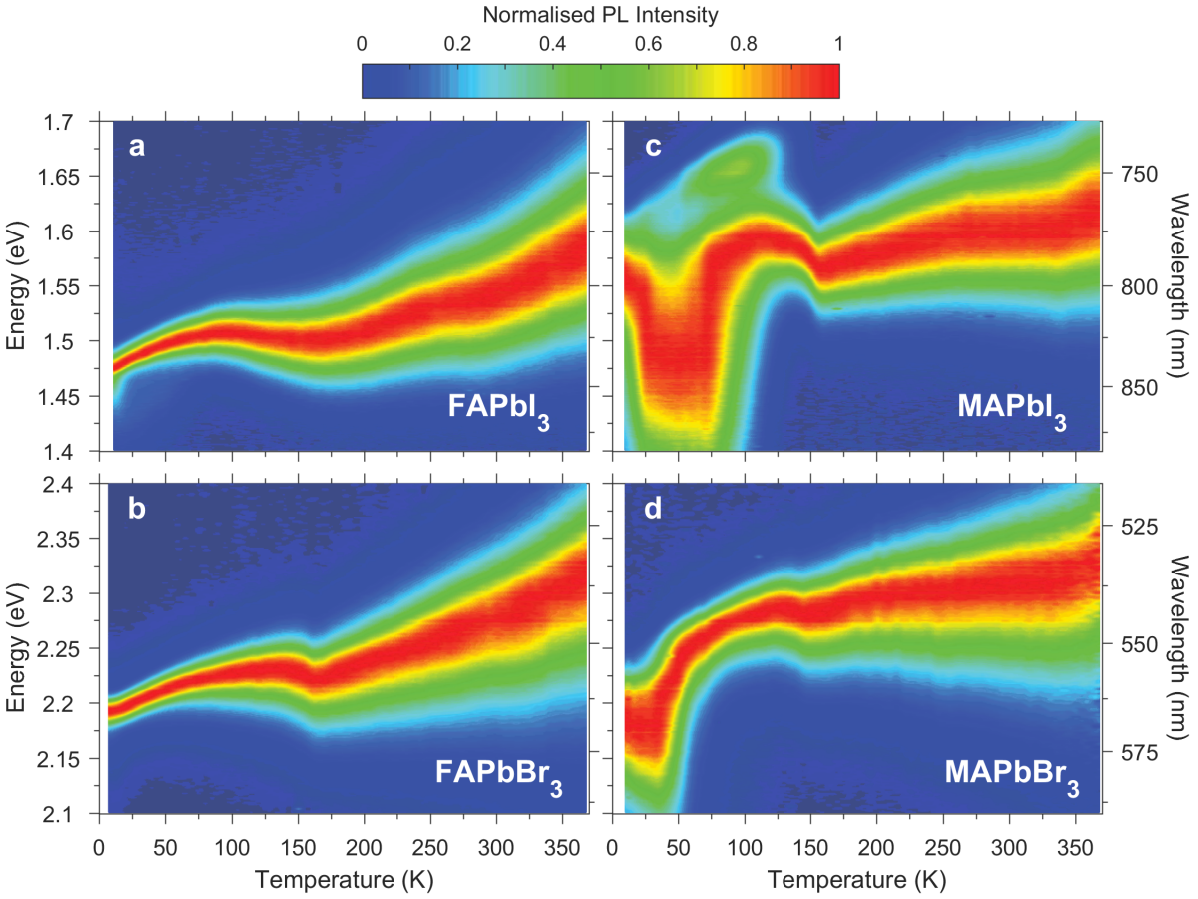

Figure 4.1: Temperature-dependence of time-integrated PL. Colour plots of normalised time-integrated photoluminescence spectra of **(a)** $FAPbI_3$, **(b)** $FAPbBr_3$, **(c)** $MAPbI_3$, and **(d)** $MAPbBr_3$ thin films at temperatures between 10 K and 370 K.

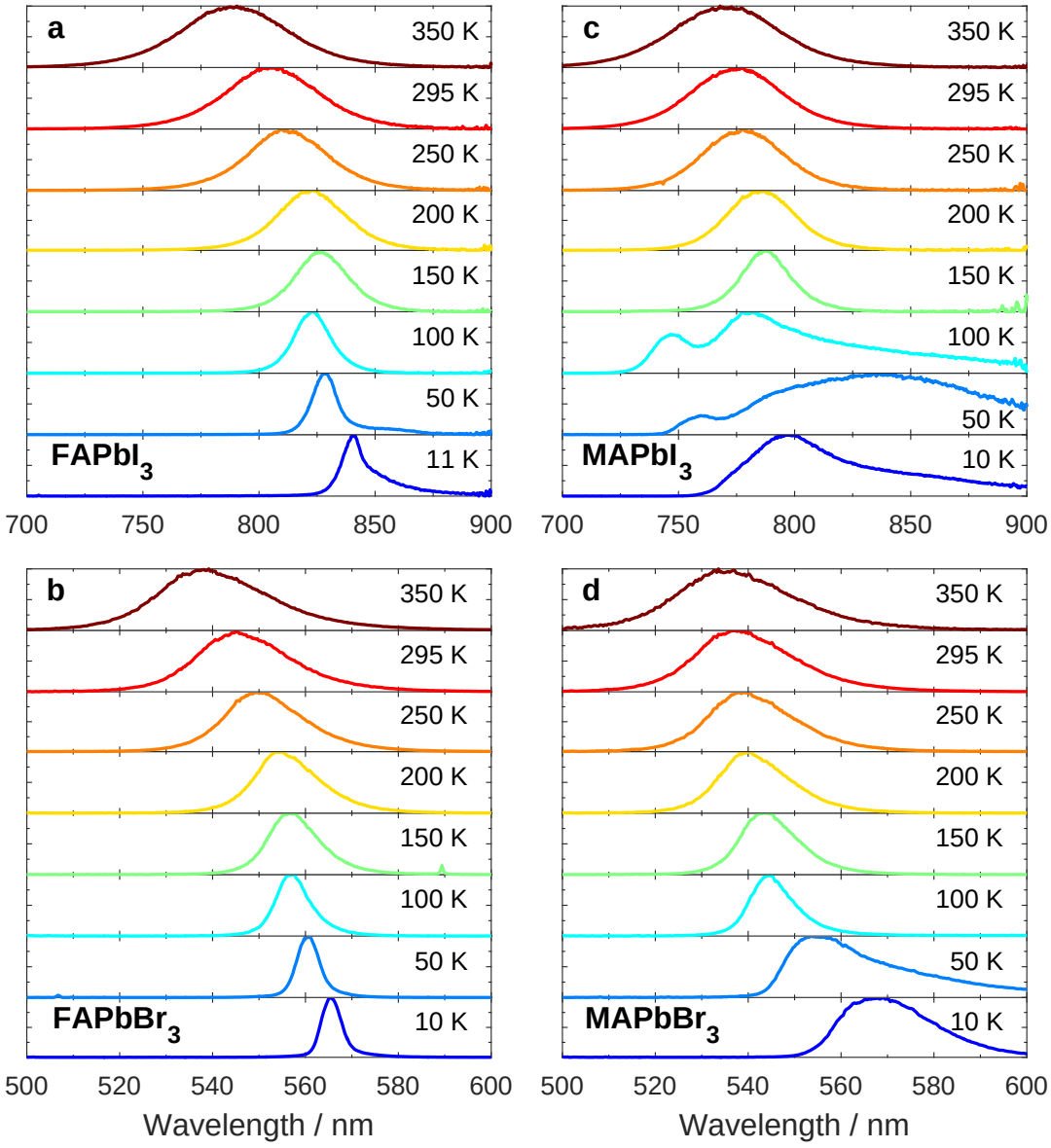

Figure 4.2: PL spectra at selected temperatures. Time-integrated PL spectra at selected temperatures for **(a)** $FAPbI_3$, **(b)** $FAPbBr_3$, **(c)** $MAPbI_3$ and **(d)** $MAPbBr_3$. The y-direction represents the normalised PL intensity.

In addition to these well-understood temperature trends, the PL spectra of MA-containing perovskites exhibit strong inhomogeneous broadening and multi-peak emission in the low-temperature orthorhombic phase. Such behaviour has been reported on many occasions [58, 73, 104, 181–183], yet a precise explanation is still outstanding. For example, the PL spectra of $MAPbI_3$ develop additional peaks at temperatures below 150 K, as can be seen clearly in Fig. 4.2, which shows spectra from the colour plots in Fig. 4.1 at selected temperatures. The emerging consensus is that these are caused by additional charge or exciton trap states that are only active in the low-temperature orthorhombic phase [58, 73, 104, 181–183]. It has been proposed that these traps could derive from a small fraction of inclusions of the room-temperature tetragonal phase that are populated through charge or exciton transfer from the majority orthorhombic phase [181]. These inclusions could be a result of strain or the proposed impossibility of a continuous structural transition from the tetragonal to orthorhombic phase in MA perovskites, as reported by Baikie *et al.* [160]. It is noteworthy that since these complicating features do not appear in the PL spectra of the equivalent FA perovskites, they are probably not intrinsic to hybrid lead halide perovskites, which re-affirms the prevailing view that they originate from trap states. Importantly, the lack of uncomplicated low-temperature spectra has to date prevented proper analysis of the linewidth broadening of MA perovskites and the associated phonon coupling to charge-carriers. As shown below, such analysis requires access to a low-temperature range over which PL spectra are dominated by intrinsic phonon broadening, rather than trap-related PL, in order for the contributions from acoustic and optical phonons to the clearly separated. The discovery that the equivalent FA lead halide perovskites do not exhibit extrinsic defect-related PL in the low temperature range, therefore allows such analysis to be carried out unhindered.

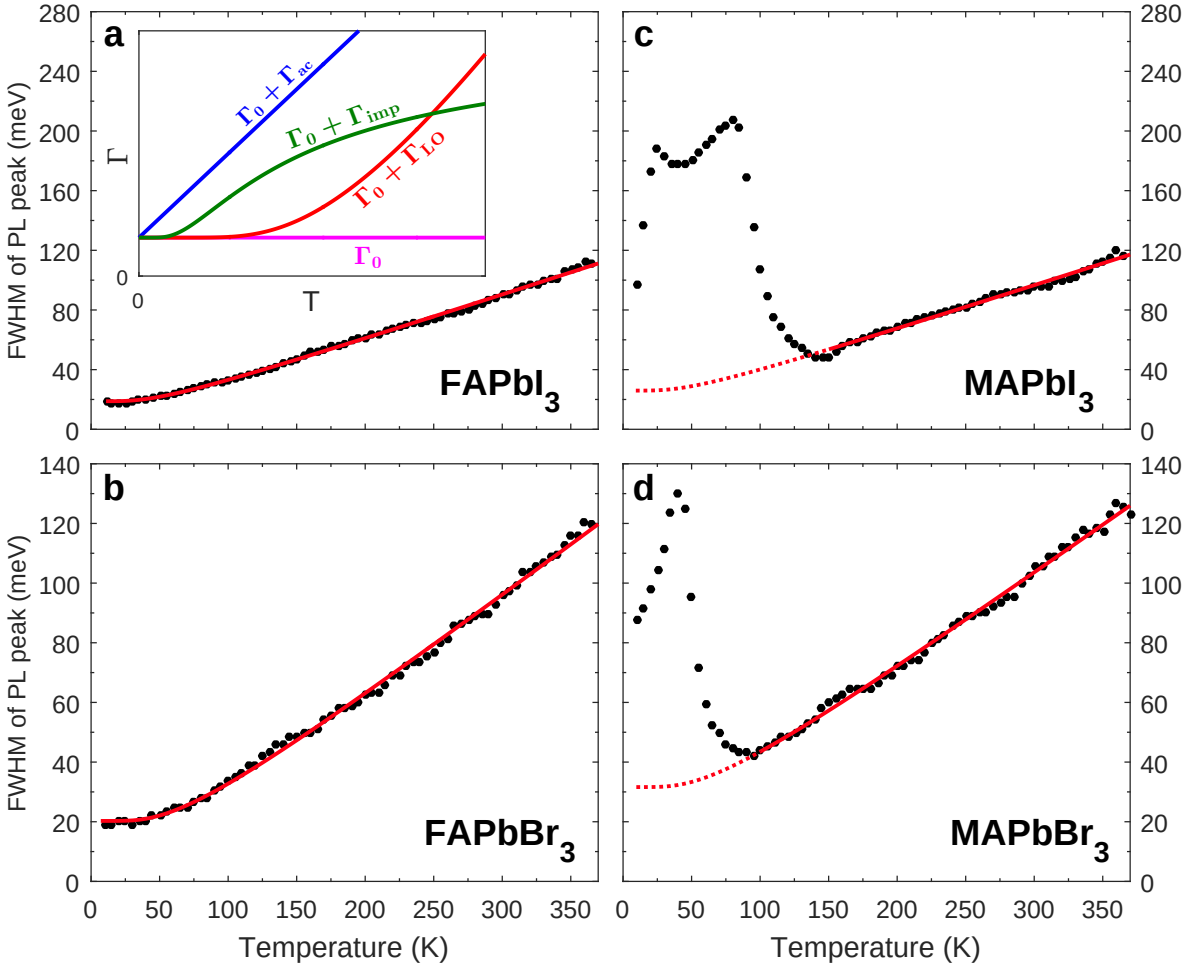

Figure 4.3: Temperature dependence of linewidth. Full width at half maximum (FWHM) of the time-integrated PL spectra as a function of temperature for **(a)** $FAPbI_3$, **(b)** $FAPbBr_3$, **(c)** $MAPbI_3$, and **(d)** $MAPbBr_3$ thin films plotted as black dots. The solid red lines are fits of $\Gamma(T) = \Gamma_0 + \Gamma_{LO}$, which account for contributions from inhomogeneous broadening and Fröhlich coupling with LO phonons. For the perovskites containing MA, the fits are extrapolated into the low-temperature region in which the model does not hold, as indicated by dashed red lines (actual fits were carried out between 150 K – 370 K for $MAPbI_3$ and 100 K – 370 K for $MAPbBr_3$). The inset shows the functional form of the temperature dependence of the contributions to PL linewidth in semiconductors from inhomogeneous broadening (Γ_0, magenta), Fröhlich coupling between charge-carriers and LO phonons (Γ_{LO}, red) and acoustic phonons (Γ_{ac}, blue), and scattering from ionised impurities (Γ_{imp}, green), as given by the terms of Equation (4.1).

4.2.2 Analysis of PL linewidth broadening

Analysis of temperature-dependent emission broadening has long been used to assess the mechanisms of electron-phonon coupling in a wide range of inorganic semiconductors [184] (see Table 4.1 for a literature overview of the results). These methods are here applied to hybrid lead halide perovskites by first extracting the full width at half-maximum (FWHM) of the PL spectra shown in Fig. 4.1 and then analyzing its temperature-dependence (plotted in Fig. 4.3). For most inorganic semiconductors, different mechanisms of scattering between charge-carriers and phonons or impurities are associated with different functional dependencies of the PL linewidth $\Gamma(T)$ on temperature, which can be expressed as the sum over the various contributions [184, 185]:

$$\begin{aligned}\Gamma(T) &= \Gamma_0 + \Gamma_{\mathrm{ac}} + \Gamma_{\mathrm{LO}} + \Gamma_{\mathrm{imp}} \\ &= \Gamma_0 + \gamma_{\mathrm{ac}} T + \gamma_{\mathrm{LO}} N_{\mathrm{LO}}(T) + \gamma_{\mathrm{imp}} e^{-E_{\mathrm{b}}/k_{\mathrm{B}}T}.\end{aligned} \tag{4.1}$$

Here, Γ_0 is a temperature-independent inhomogeneous broadening term, which arises from scattering due to disorder and imperfections [184, 186]. The second and third terms (Γ_{ac} and Γ_{LO}) are homogeneous broadening terms which result from acoustic and LO phonon (Fröhlich) scattering [106, 184, 186] with charge-carrier–phonon coupling strengths of γ_{ac} and γ_{LO}, respectively. Electron-phonon coupling is in general proportional to the occupation numbers of the respective phonons, as given by the product of the phonon density of states (incorporated into the γ_{LO} term) and the Bose-Einstein distribution function [187, 188], taken as $N_{\mathrm{LO}}(T) = 1/[e^{E_{\mathrm{LO}}/k_{\mathrm{B}}T} - 1]$ for LO phonons, where E_{LO} is an energy representative of the frequency for the weakly dispersive LO phonon branch [17, 189]. For acoustic phonons whose energy is much smaller than $k_{\mathrm{B}}T$ over the typical observation range, a linear dependence on temperature is generally assumed [188, 190]. *Ab initio* calculations of the relevant phonon energies and occupation numbers are shown in Figure 4.4 confirm that the linear approximation to the acoustic phonon population used in Eqn. 4.1 is appropriate. The final term, Γ_{imp}, phenomenologically accounts for scattering

from ionised impurities with an average binding energy E_b [185]. These impurities contribute γ_{imp} of inhomogeneous broadening to the width when fully ionised [185, 187].

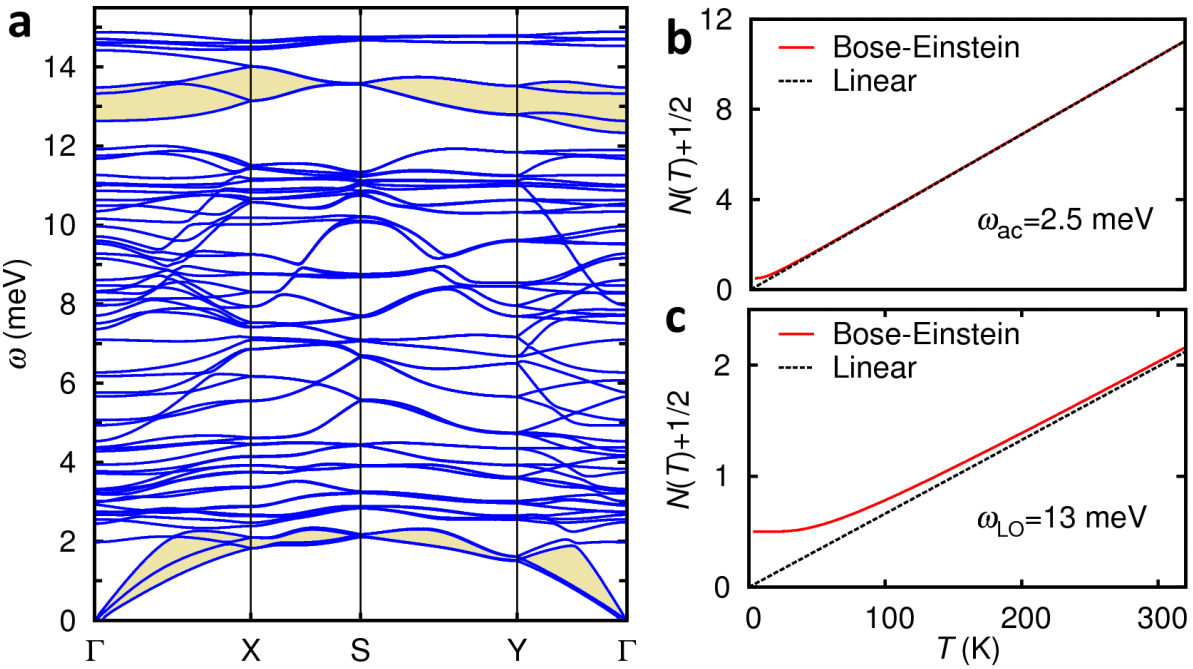

Figure 4.4: Phonon dispersion and population relations from *ab initio* calculations. The calculated phonon dispersion relation for $MAPbI_3$ is shown in **(a)**, with the acoustic modes (bottom) and the polar optical modes (top) highlighted in orange. Here we see that the frequency of the acoustic modes is always smaller than 2.5 meV, while the polar optical modes are centred on 13 meV. On the right, the phonon population according to the Bose-Einstein function, $N(T)$, is plotted in red as a function of temperature for **(b)** the acoustic modes and **(c)** the polar optical modes. The Bose-Einstein phonon population is offset vertically by $+1/2$ to allow direct comparison with linear approximations to the phonon population, which are plotted as dotted black lines. The linear temperature dependence used in Eqn. 4.1 in the main text for the linewidth broadening due to acoustic phonons is therefore very accurate in the case of $MAPbI_3$ for all temperatures above 10 K, while the Bose-Einstein function is necessary to model the broadening due to optical phonons.
[produced by C. Verdi, Department of Materials, University of Oxford]

Table 4.1: Linewidth parameters for perovskites and inorganic semiconductors. Collated values of linewidth parameters for inorganic semiconductors reported by other experimental studies, along with those obtained from this one . The FWHM definition of linewidth is used here, but some papers, indicated by an asterisk (*) in the materials column, define it as the HWHM (Half Width at Half Maximum); the values of Γ_0, γ_{ac}, γ_{LO} and γ_{imp} values from these papers are multiplied by two. Blank cells indicate parameters which were not considered in a paper. When a parameter used in a fit was fixed, that value is underlined in the table. Materials were studied in the bulk, except for those at the bottom of the table, which were studied as quantum wells (indicated by §), or epilayers (‡).

Material	Technique	Source	Γ_0 (meV)	γ_{ac} (μeV K^{-1})	γ_{LO} (meV)	E_{LO} (meV)	γ_{imp} (meV)	E_b (meV)
$FAPbI_3$	PL		19±1		40±5	11.5±1.2		
$FAPbBr_3$	PL		20±1		61±7	15.3±1.4		
$MAPbI_3$	PL		26±2		40±2	11.5		
$MAPbBr_3$	PL		32±2		58±2	15.3		
CdS	A	[191]*	0.32	29.0	212	38		
CdSe	E	[192] †*	4.6±0.6		46±2	25.9		
CdTe	R	[184]*			34±14			
GaAs	PL	[193]	0.32	13±3	30.4±4			
	A	[194]*		14	17.4	36.6		
	R	[195]*			40±2	36		
ZnO	PL	[196]	10.3		962.7	71	13.8	9.2
ZnSe	R	[184]*			60±14			
	FWM	[197]	1.3	11	81			
$CdTe/Cd_{1-x}Mn_xTe$	FWM	[198]§	0.89±0.05	13.7±1.8				
$CdTe/Cd_{1-x}Zn_xTe$	PL	[199]§	75		400	22	500	92
$GaAs/Al_xGa_{1-x}As$	PL	[185]§HH *	0.9	2.94	8	36	1.5	10
	PL	[185]§LH *	0.6	2.38	4.9	36	0.4	10
GaN	PL	[106]‡†*	5.6	42	1050	91.5		
$Zn_{0.56}Cd_{0.44}Se$	R	[186] ‡ *	12±4	2.2	34±12	28.8		
ZnSe	R	[186]‡*	13±5	4.0	48±16	31		

A	Absorption
E	Ellipsometry
FWM	Four-wave mixing
PL	Photoluminescence
R	Reflectance
*	Original linewidth stated in terms of HWHM
†	Linewidth of exciton A
HH	Heavy hole exciton
LH	Light hole exciton
§	Quantum well
‡	Epilayer

In general (as detailed in Section 2.6), the two major mechanisms governing the electron-phonon coupling in inorganic semiconductors are deformation potential scattering, in which distortions of the lattice change the electronic bandstructure, and electromechanical or piezoelectric interactions, in which lattice-related electric fields modify the electronic Hamiltonian [17]. Specifically, the LO phonon term in Equation (4.1) accounts for the Fröhlich interaction between LO phonons and electrons, which arises from the Coulomb interaction between the electrons and the macroscopic electric field induced by the out-of-phase displacements of oppositely-charged atoms caused by the LO phonon mode [17]. While both transverse optical and LO phonons interact with electrons via nonpolar deformation potentials, Equation (4.1) only accounts for LO phonons because of the dominant influence of their Fröhlich interaction with electrons in polar crystals at higher temperatures [200]. Since optical phonons in semiconductors typically have energies of the order of tens of meV [17], their population at low temperatures ($T < 100$ K) is very small, so homogeneous broadening in this regime predominantly results from acoustic phonons [17, 200]. Therefore, careful examination of the low-temperature regime allows separation of the contributions from optical and acoustic modes. Long-wavelength acoustic phonons induce atomic displacements, which can correspond to macroscopic crystal deformation, affecting electronic energies via either the resultant deformation potential or a piezoelectrically induced electric field [17].

To establish qualitatively which electron-phonon scattering mechanisms contribute in hybrid lead halide perovskites, the temperature-dependent PL linewidths plotted in Fig. 4.3 are compared with the functional form of the terms in Eqn. 4.1. To aid comparison, the inset to Fig. 4.3(a) shows example functions for the separate components. First, the possibility is assessed of electron scattering with ionized impurities playing a significant role. Comparison of the curves in the inset with the data in the main Fig. 4.3 makes it apparent that the shape of the ionised impurity scattering term Γ_{imp} could not

produce the observed linear variation with T of the linewidths at high temperatures. This leads to the conclusion that scattering with ionized impurities does not play any major role here, in agreement with findings based on recent analyses of the temperature-dependence of the charge-carrier mobility in this regime [58, 102–104]. The assumption that $\Gamma_{\mathrm{imp}} \approx 0$ is therefore made for the rest of this analysis.

To separate the contributions from acoustic and optical phonon modes, consideration is first given to an analysis of the PL linewidth for perovskites containing FA as the organic cation. As Figs. 4.3(a)&(b) show, these materials exhibit smooth variation of the linewidth, while for MA-containing perovskites the presence of the impurity emission discussed above leads to additional emission broadening in the low-temperature phase (Figure 4.3(c)&(d)). Both $FAPbI_3$ and $FAPbBr_3$ approach a PL linewidth of the order of 20 meV towards T=0, which can therefore be identified as the temperature-independent inhomogeneous broadening term Γ_0 arising from disorder. To qualitatively assess the relative importance of acoustic versus optical phonon contributions, an inspection of the gradient of these curves in the low-temperature regime is essential. While the optical phonon terms lead to a gradient of zero in the regime for which $k_{\mathrm{B}}T < E_{\mathrm{LO}}$, the smaller energies of acoustic phonons should result in a non-zero gradient given by γ_{ac} here. However, visual inspection of the graphs in Figs. 4.3(a)&(b) shows that the gradient of the FWHM versus temperature approaches zero at low temperature, suggesting negligible acoustic phonon contribution ($\gamma_{\mathrm{ac}}\approx 0$). Indeed, fits of Equation (4.1) to these curves converge with $\gamma_{\mathrm{ac}}\rightarrow 0$. This result is not surprising, given that in polar inorganic semiconductors the contribution of acoustic phonons to the broadening at room temperature is typically dwarfed by that of the LO phonons, and indeed several studies ignore the contribution of acoustic phonons in such systems [200]. We may however obtain an upper limit to γ_{ac} by careful examination of the data in the low-temperature regime in which acoustic phonons are still expected to contribute significantly. Here we

may fit $\Gamma(T) = \Gamma_0 + \gamma_{ac}T$ to the data in the low-temperature ($T < 60K$) region[194] or, as an alternative method, obtain the gradient of the data near T=0 K from differentiation. Both methods yield upper limits around $\gamma_{ac} = 60 \pm 20$ µeV K^{-}1 for $FAPbI_3$ and $FAPbBr_3$, therefore, acoustic phonons will only contribute up to approximately 18 meV to the linewidth broadening at 300 K. This analysis hence illustrates that the majority of broadening in the room-temperature regime arises from charge-carrier interactions with optical phonons, as would be expected for a polar semiconductor.

To further quantify the dominant Fröhlich coupling in these systems, the linewidth data are fitted including only the mechanisms based on temperature-independent inhomogeneous broadening and Fröhlich coupling to LO phonon modes. For perovskites containing FA cations, fits of $\Gamma(T) = \Gamma_0 + \Gamma_{LO}$ to the PL linewidth data are plotted in Figs. 4.3(a) and (b) (red lines), and the extracted fitting parameters are presented in Table 4.2. Apart from Fröhlich coupling strengths, it is also possible to determine the energy of LO phonon modes that play the dominant role in electron-LO-phonon coupling. A value of E_{LO}= 11.5 meV is found for $FAPbI_3$, with the value for $FAPbBr_3$ (15.3 meV) being 1.3 times larger, which is only slightly greater than the factor of 1.2 expected from a crude model of the frequency of a diatomic harmonic oscillator. These LO phonon energies of hybrid lead halide perovskites are somewhat lower than those typically measured for a range of inorganic semiconductors (see Ref. [72] for an overview), however, they agree well with a recent combined experimental and density functional theory study assigning LO phonon modes of the Pb-I lattice in $MAPbI_3$ with energies near 10 meV [166] and with first-principles calculations based on many-body perturbation theory (see 4.2.3 below).

As noted above, the situation is more complex for MA perovskites owing to the additional trap-related emission in the low-temperature orthorhombic phase that gives rise to sizeable (>100 meV) additional broadening (see Figs. 4.3(c)&(d)). However, in the high-temperature regime, PL linewidths of the MA perovskites vary much in the

same fashion as that of their FA counterparts, suggesting very similar mechanisms. This may be expected, as the organic cation has relatively little influence on the vibrations of the lead-halide lattice. Hence it is reasonable to model the linewidth broadening of MA perovskites in the high-temperature regime again using $\Gamma(T) = \Gamma_0 + \Gamma_{\mathrm{LO}}$ (solid red lines in Figs. 4.3(c) and (d)) using the LO phonon energies determined previously for FA perovskites. The resultant γ_{LO} values are, as expected, very similar to those for the corresponding FA perovskites (Table 4.2). These fits may be extrapolated down through the low-temperature regime (dashed red lines), where they do not reflect experimental reality, but rather show the broadening that would be present if the additional defects in the orthorhombic phase were absent. As such, values extracted for the parameter Γ_0 here therefore mostly reflect inhomogeneous disorder present in the high-temperature phases of $MAPbI_3$ and $MAPbBr_3$ at temperatures above 150 K and 100 K, respectively.

Sample	Γ_0 / meV	γ_{LO} / meV	E_{LO} / meV
$FAPbI_3$	19 ± 1	40 ± 5	11.5 ± 1.2
$FAPbBr_3$	20 ± 1	61 ± 7	15.3 ± 1.4
$MAPbI_3$	26 ± 2	40 ± 2	*[11.5]*
$MAPbBr_3$	32 ± 2	58 ± 2	*[15.3]*

Table 4.2: Extracted linewidth parameters. Linewidth broadening parameters extracted from fits of $\Gamma(T) = \Gamma_0 + \Gamma_{\mathrm{LO}}$ to the PL linewidth data for the four hybrid perovskite films. Γ_0 is the inhomogeneous broadening (the linewidth at 0 K), γ_{LO} is the strength of the LO phonon–charge-carrier Fröhlich coupling, and E_{LO} is the relevant LO phonon energy. For fits to the data from MA-containing perovskites, the values of E_{LO} extracted previously for the FA-containing perovskites were used (hence they are italicized and enclosed in square brackets). Because of the additional defect luminescence present in the orthorhombic phase of the MA-containing perovskites, fits were only carried out between 150 K – 370 K for $MAPbI_3$ and 100 K – 370 K for $MAPbBr_3$ (see solid lines in Figs. 4.3(c) and (d)). Therefore the extracted parameters do not reflect the lineshape broadening in the low-temperature phase of the MA-containing perovskites.

4.2.2.1 Excitons vs free charges

The extent to which excitonic effects may influence the coupling between charge-carriers and phonons is worth commenting upon. While the exact values for the exciton binding energies in these systems are still a matter of debate, most reported values

fall into the range of a few to a few tens of milli-electronvolts (see Ref. [13] for a review). These values are compatible with numerous studies demonstrating that at room temperature, following non-resonant excitation, hybrid lead halide perovskites sustain free charge-carriers as the predominant species [57, 62, 201]. Excitonic effects in the generated charge-carrier population are expected to increase as the temperature is lowered. However, infrared photoinduced transmission spectra for methylammonium lead iodide perovskite [58] have recently been found to be predominantly governed by free-charge (Drude-like) features, with localization effects (e.g. from excitons) only contributing at low temperature and not more than around 23% even at 8 K. This suggests that over the temperature-window we examine here, emission broadening is mostly governed by interactions between phonons and free charge-carriers, rather than excitons. Such predominantly free-charge behaviour of the photogenerated species may be understood for example in terms of the Saha equation or a low Mott density for these systems, and considering that the initial highly non-resonant excitation generates predominantly free electron-hole pairs [202]. We may further inspect in more detail the temperature-dependent line shapes of the emission spectra and find these to exhibit high-energy Boltzmann tails corresponding to a thermalized electron-hole density near the lattice temperature (see Fig. 4.5). These overall observations are therefore compatible with the presence of a thermalized free electron-hole charge-carrier density that scatters off mostly LO phonons whose occupancy is governed by the Bose-Einstein distribution function. Analysis of how the energies of such thermalized free electrons and holes influence the precise lineshape of the PL spectra as a function of temperature could provide additional insight into the scattering mechanisms for free charge carriers. Such additional analysis is however beyond the scope of the present investigation, which is limited to considering only the extent of linewidth broadening.

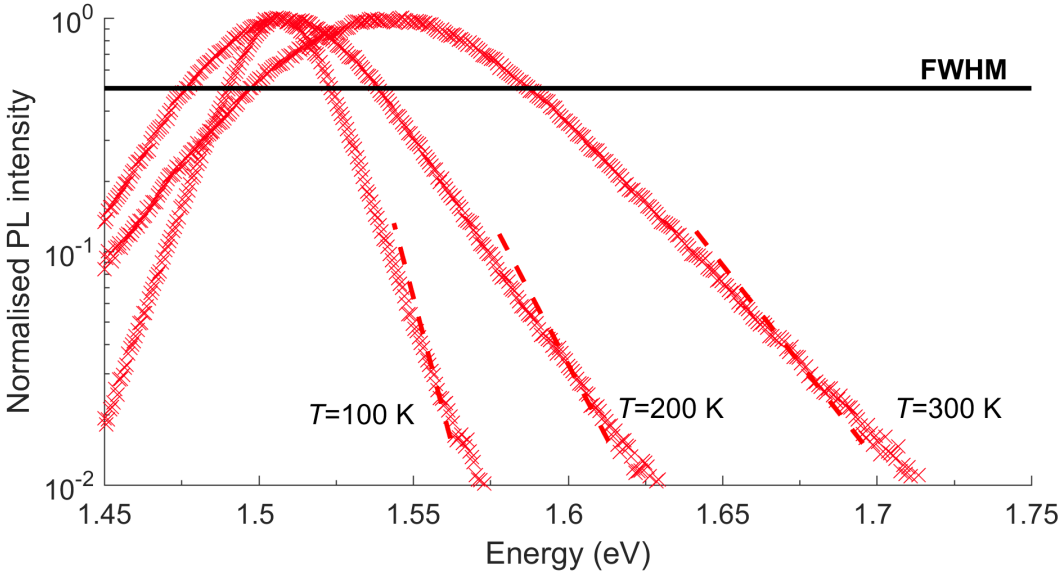

Figure 4.5: Carrier energy distribution from PL tails. Steady-state PL spectra at temperatures (T) for an FAPbI3 thin film, plotted as red crosses. The high-energy tails of the band edge PL can be approximated by the dashed red lines representing the functional form $I(E) \propto \exp\left[-(E - E_g)/k_B T_c\right]$, which describes the PL lineshape expected from thermalized charge carriers of temperature T_c following a Boltzmann energy distribution [200]. I is the PL intensity, E is the PL energy and E_g is the bandgap energy. The solid black line indicates the position on the curves at which the FWHM is measured, which lies above the high-energy tail of the band edge PL. For the shown dashed red lines, the carrier temperature T_c was set as the sample temperature T. However, slightly shallower tails (indicating T_c somewhat higher than T) are actually observed. One reason for this discrepancy may lie in the strongly non-resonant excitation at 3.1 eV which leads to an initial thermalized "hot" charge-carrier density that subsequently cools to the lattice temperature [97, 203]. Since the PL curves shown represent an average over the charge-carrier temperature during the lifetime of charge-carriers, a temperature slightly elevated above the lattice temperature may be found. However, the overall line shape is also strongly governed by electron-phonon coupling, as described in the main text, whose effects will influence the spectral shape also in the high-energy tail.

4.2.3 First-principles calculations

[carried out by C. Verdi, Department of Materials, University of Oxford]

The above analysis of the linewidth was corroborated further by first-principles calculations of the electron-phonon coupling in $MAPbI_3$ (see details in Section 3.4; the full details of the computational methods used and the results obtained are presented in Ref. [72]).

In accordance with the above discussion, the broadening arising from the interaction of phonons with free conduction-band electrons and free valence-band holes [204] are here separately considered. The combined broadening arising from both types of charge-carrier is then compared to the experimentally determined emission broadening. Fig. 4.6(a) presents a heat-map of the imaginary part of the electron-phonon self-energy, $\mathrm{Im}(\Sigma)$, projected on the quasiparticle band structure of $MAPbI_3$. $2\,\mathrm{Im}(\Sigma)$ represents the linewidth of electrons and holes arising from the electron-phonon interaction before accounting for many-body effects and is therefore directly comparable to the experimentally determined FWHM of the PL emission linewidth. Fig. 4.6(b) shows $\mathrm{Im}(\Sigma)$ as a function of electron energy, together with the density of electronic states (DOS). This figure indicates that the increase in the linewidth is linked to the phase-space availability for electronic transitions, that is, $\mathrm{Im}(\Sigma)$ increases with increasing DOS because each state can scatter into a higher number of states by absorbing or emitting a phonon. The calculations show that the dominant contribution to the electron-phonon self-energy arises from the coupling with the LO mode at $\hbar\omega_{\mathrm{LO}} \approx 13$ meV, which is shown schematically in Fig. 4.6(c). This observation is compatible with the analysis of the temperature dependence of the PL broadening, as presented in Figure 4.3, yielding similar energy for the predominantly coupling LO phonon mode in $MAPbI_3$.

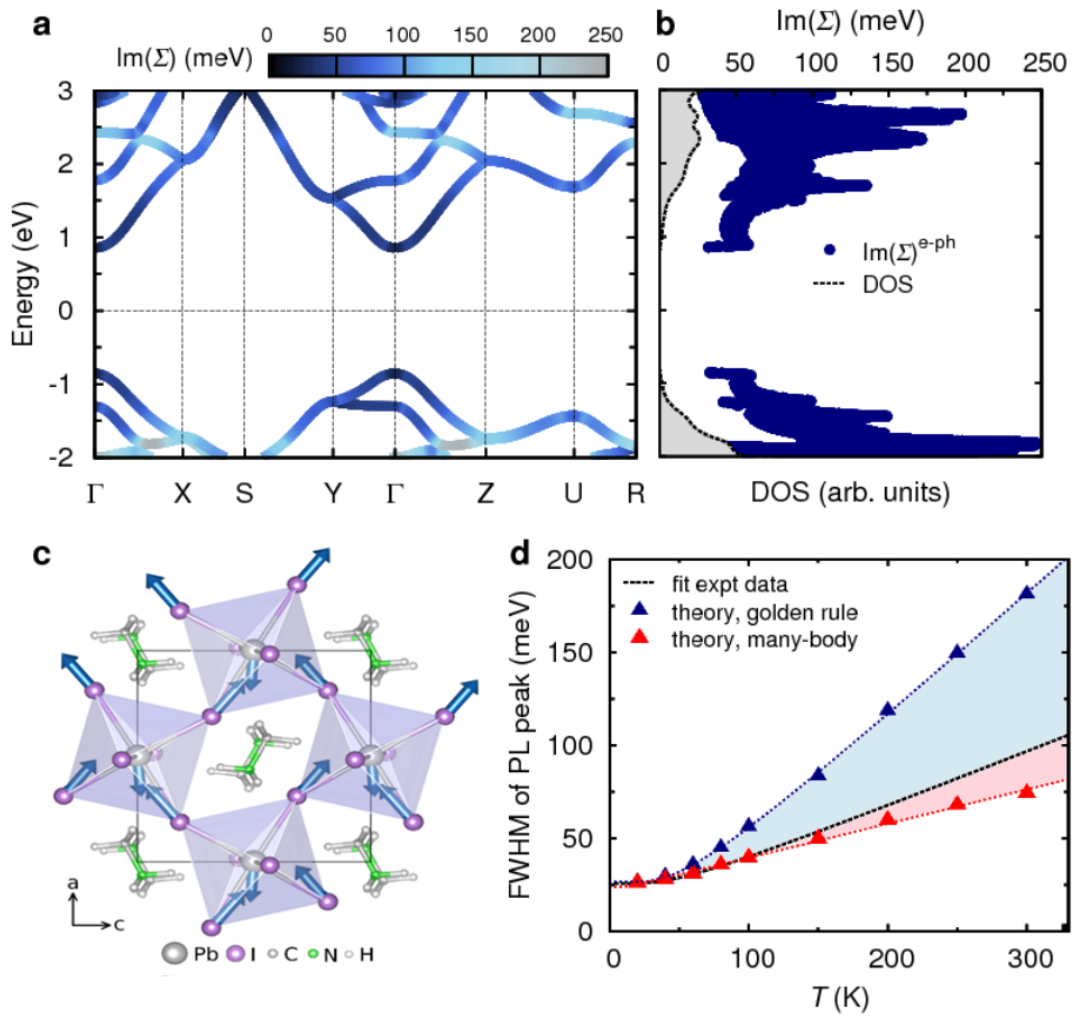

Figure 4.6: *Ab initio* calculations of electron-phonon coupling and PL broadening in $MAPbI_3$. (a) Electronic band structure of orthorhombic $MAPbI_3$, calculated within the GW approximation as in Ref. [164], combined with a heat-map of the imaginary part of the electron-phonon self-energy ($\mathrm{Im}(\Sigma)$) at T=200 K. The zero of the energy is placed in the middle of the bandgap. In **(b)** the imaginary part of the electron-phonon self-energy is shown together with the electronic density of states (DOS). $2\,\mathrm{Im}(\Sigma)$ corresponds to the electron/hole linewidth arising from electron-phonon coupling (apart from the quasiparticle renormalization factor Z). **(c)** Ball-and-stick representation of the LO vibration responsible for the broadening of the PL peaks. The blue arrows indicate the displacements of Pb and I atoms, for the phonon wavevector $\mathbf{q} \to 0$ along the [100] direction. This is a Pb−I stretching mode with B_{3u} symmetry [166]. **(d)** Temperature dependence of the FWHM of the PL peak in $MAPbI_3$: fit to the experimental data (dashed black line) and theoretical calculations using Fermi's golden rule (blue triangles) and the more accurate Brillouin-Wigner perturbation theory (red triangles). The theoretical broadening is obtained as the sum of $2\,\mathrm{Im}(\Sigma)$ at the valence and conduction band edges in the case of Fermi's golden rule, and the sum of $2\,Z\,\mathrm{Im}(\Sigma)$ when including many-body quasiparticle renormalization, rigidly shifted by the FWHM at $T = 0$ K (25.72 meV) to account for inhomogenous broadening. The lines are guides to the eye.
[produced by C. Verdi, Department of Materials, University of Oxford]

Figure 4.6(d) shows that the calculated temperature-dependence of the PL broadening is in good agreement with experiment. In this figure the calculations are compared with the experimental trends obtained from the fit shown in Figure 4.3 (which does not account for the anomalous broadening below 150 K, as discussed above). The blue triangles represent the data calculated based on Fermi's golden rule, which is equivalent to using the imaginary part of the electron-phonon self-energy, $2\,\mathrm{Im}(\Sigma)$, while the red triangles were obtained by using Brillouin-Wigner perturbation theory [205], which corresponds to scaling the self-energy by the quasiparticle renormalization factor Z, that is $2\,Z\,\mathrm{Im}(\Sigma)$ The comparison between calculations and experiments shows that the experimental data are most accurately described by fully taking into account the many-body renormalization of the electron lifetime. Taken together, the impressive agreement between firstly the measured and calculated characteristic phonon energy scale (11.5 and 13 meV respectively), secondly the magnitude of the measured and calculated linewidth broadening at room temperature (90 and 75 meV respectively), and thirdly the phonon energy scale identified here and the LO phonon identified between 10-13 meV in our previous IR study [166], strongly support the notion that the broadening of the PL spectra reflects the interaction between free carriers and LO phonons.

In addition, it is possible to use first-principle calculations to elucidate why the lead bromide perovskites exhibit Fröhlich coupling constants that are larger than those of the lead iodide system by a factor of 1.5. In order to investigate this trend, DFT calculations were performed for $MAPbBr_3$ to compare the associated Born effective charges between the two systems. The results indicate that the electron-phonon coupling in the bromide perovskite is 40% stronger than in the iodide perovskite, in excellent agreement with our measurements. It was found that the increased Fröhlich coupling in $MAPbBr_3$ is primarily connected with the smaller high-frequency value of the dielectric function compared to $MAPbI_3$, as presented in Table 4.3.

Table 4.3: Calculated electrical parameters. Calculated Born effective charges (Z^*), high-frequency and static dielectric constants (ϵ^∞ and ϵ^0 respectively) of $MAPbI_3$ and $MAPbBr_3$ in the orthorhombic phase. The isotropic average of the tensors is reported, and the dielectric constants are compared to experiment.
[obtained by C. Verdi, Department of Materials, University of Oxford]

	Z^*				ϵ			
	Pb	I/Br	C	N	ϵ^∞	ϵ^∞_{exp}	ϵ^0	ϵ^0_{exp}
$MAPbI_3$	4.42	-1.88	0.03	-0.95	5.86	6.517 [206]	25.3	30.518 [30]
$MAPbBr_3$	4.11	-1.78	0.09	-0.8	4.71	4.819 [207]	23.9	26.218 [30]

4.3 Discussion

The combined analysis of the experimentally determined emission linewidth broadening and first-principles calculations strongly support the notion that Fröhlich coupling to LO phonons is the predominant charge-carrier scattering mechanism in hybrid lead halide perovskites. As already discussed above, such behaviour is in many ways to be expected for these materials because the lead-halide bond is sufficiently polar (see the calculated Born effective charges in Table 4.3) to lead to macroscopic polarizations from LO phonon modes that modify the electronic energies, causing electron-phonon scattering. Coupling of charge-carriers to phonons with energies in the meV range has also been postulated from the signature of such modes in the room- and low-temperature photoconductivity spectra [58, 208].

However, the predominance of Fröhlich coupling appears at first sight to contradict the measured [58, 102–104] temperature-dependence of the charge-carrier mobility which has been stated [64, 96, 104] to approach the expected form for acoustic deformation potential scattering ($\mu \propto T^{-3/2}$). Nonetheless, while electron-phonon coupling generally leads to charge-carrier mobilities that increase with decreasing temperature, the exact functional dependence is usually a composite of many different scattering mechanisms that can be hard to attribute uniquely [17]. Thus, while acoustic phonon deformation potential scattering may result in $\mu \propto T^{-3/2}$, the converse may not necessarily also hold.

In addition, the rapid energy loss of electrons observed following non-resonant excitation [97, 203] can only sensibly be explained by a succession of high-energy optical phonon emissions [209], as is typically observed in inorganic semiconductors [13, 210].

It is therefore concluded that Fröhlich coupling to LO phonons, rather than acoustic phonon deformation potential coupling, is the dominant charge-carrier scattering mechanism at room temperature in these hybrid lead halide perovskites. While our findings themselves do not explain the temperature dependence of the charge-carrier mobility in these materials, they support the hypothesis that the observed $\mu \propto T^{-3/2}$ relationship is not wholly attributable to acoustic deformation potential scattering. It is also clear that for these high-quality materials, scattering from ionized impurities is a negligible component at room temperature, with both the PL linewidth data presented here and earlier charge-carrier mobility measurements [58, 102, 103] indicating a complete absence of such contributions.

In addition, these findings give early answers to the question of how perovskite composition affects Fröhlich interactions between charge-carriers and phonons. Such interactions determine the maximum charge-carrier mobilities intrinsically attainable which in turn affects charge-carrier extraction in solar cells. It is shown here that Fröhlich coupling in hybrid lead bromide perovskites appears to be stronger because of the lower dielectric function in the high-frequency regime. Indeed, the THz charge-carrier mobility for $FAPbBr_3$ thin films has recently been shown to be somewhat lower than that for $FAPbI_3$ films [18], which could be related to decreased momentum scattering time resulting from increased scattering with LO phonons. However, it may also be partly related to a higher propensity towards disorder in the bromide perovskites as the inhomogeneous broadening parameter Γ_0 appears to be somewhat higher for bromide than iodide perovskites here. Similarly, higher Urbach energies have previously been reported for $MAPbBr_3$ compared to $MAPbI_3$ in accordance with larger energetic disorder in the

former [124]. It is also shown here that Γ_0 tends to be lower for the perovskites containing FA as the organic cation, which points to larger material uniformity as one reason behind this material's recent success in the highest efficiency perovskite solar cells [51, 171].

It is also possible to compare these findings with those of other polar inorganic semiconductors for which Fröhlich coupling is known to be active. Table 4.1 provides a detailed literature survey of values established for γ_{LO} in other inorganic semiconductors. It has been pointed out [64] that charge-carrier mobilities established for lead-halide perovskites (typically $\leq$100 $\mathrm{cm}^2\ (\mathrm{V\ s})^{-1}$) [19, 64] are relatively modest compared with those achieved in high-quality GaAs despite the effective charge-carrier masses in perovskites being only slightly elevated above those in GaAs. The values of $\gamma_{\mathrm{LO}} \approx 40$ meV and $\gamma_{\mathrm{LO}} \approx 60$ meV extracted from the data in this study for the respective iodide and bromide perovskites (see Table 4.2) are somewhat higher than the range reported for GaAs (see comparison in Table 4.1) which may partly explain these discrepancies. However, they are significantly lower than those typically found in highly polar materials such as GaN and ZnO where they can be over an order of magnitude higher [106]. Further theoretical modelling of charge-carrier mobility in these systems based on our findings will most likely allow more quantitative explanations and predictions to be made.

5

Band-tail recombination in hybrid lead iodide perovskite

Initially published in Ref. [71].

This study investigates the distribution of sub-bandgap trap states in formamidinium lead triiodide ($FAPbI_3$), a perovskite material used in some of the most efficient and stable perovskite solar cells [51, 211]. By judicious measurement of the low-temperature PL over six decades of time and intensity, it was possible to identify for the first time a power-law intensity decay, which is a known signature of band-tail mediated recombination. This analysis is supported by the observation of a Stokes-shifted emission peak at low temperatures that exhibits an anomalous temperature-dependence, in accordance with the temperature-activated movement of charge within a distribution of localized states. The anomalous relative Stokes shift was qualitatively reproduced using both a rate-equation model and a Monte Carlo simulation, demonstrating the presence of a band tail with characteristic energy $\approx$3 meV. It is further shown that this distribution of sub-bandgap states can yield emission several tens of meV below the bandgap energy when it originates from states deep in the tail. The possibility is suggested that these band tail states result from variations in local structure or electrostatic potential caused

e.g. by difference in orientation of the FA cation dipole. Altogether, these results provide new insight into the fundamental cause and nature of trap states in $FAPbI_3$, which are demonstrated to be governed by a continuous energy distribution of trap states that may arise e.g. from structural disorder. As a result, it is shown that trap states associated with a discrete energetic origin, such as elemental vacancies, substitutions or interstitials, or an indirect energy gap with well-defined single gap energy, cannot be a dominant cause of charge-carrier trapping in $FAPbI_3$.

5.1 Experimental details

Thin film samples of $FAPbI_3$ were spin-coated according to the procedure described in Subsection 3.3.1. The samples were mounted under vacuum ($P < 10^{-6}$ mbar) in a cold-finger liquid helium cryostat. For the temperature-dependent measurements PL spectra were taken with the iCCD as the sample was heated in increments of 2 K between 10 and 50 K. A pulse repetition rate of 10 kHz was used for the 390 nJ cm^{-2} measurements, and 1kHz for the 110 and 10 nJ cm^{-2} measurements. For the time-dependent measurements, TCSPC data from 1 to 100 ns after excitation was meshed with iCCD data from 3 ns to 1 ms after excitation. A repetition rate of 1 kHz and a fluence of 390 nJ cm^{-2} were used. For the power-dependence measurements, the laser was used in continuous wave mode, and attenuated with a combination of neutral density filters, resulting in excitation intensities from 260 W cm^{-2} to 10 μW cm^{-2}. Monte Carlo simulations were carried out in MATLAB according to the algorithm described in Ref.[212] and summarized in Subsection 5.2.4.2.

5.2 Results

5.2.1 Time dependence of PL

To explore the nature of trap states in hybrid lead halide perovskites, the time-dependent PL spectra of solution-processed $FAPbI_3$ thin films were first recorded between 1 ns and

1 ms after excitation and over temperatures from 10 to 100 K. At these low temperatures, the charge carriers have relaxed to the bottom of any trap distribution and non-radiative recombination pathways are suppressed [58, 69], allowing PL to provide a probe of the full energetic distribution. Over most of this temperature range, these charge carriers most likely exist as excitons since the thermal energies for these temperatures are below the exciton binding energy (14 meV) [213] for the low temperature phase of $FAPbI_3$, though towards the upper end of the range (i.e. the data at 100 K shown in Fig. 5.7) free carrier recombination will play a larger role. Transients of the spectrally-integrated PL intensity at 10 K, 20 K and 30 K are shown in Fig. 5.1a. These transients appear straight on the log-log scale, i.e. the decay remarkably seems to follow a power law over six decades of time after excitation.

5.2.1.1 Attempts to fit the PL transients

Previously, PL transients from hybrid lead halide perovskites have generally been recorded over much shorter time intervals, over which they are often fitted with monoexponential [75, 76] or biexponential [41, 77] functions, representing one or two monomolecularly decaying charge-carrier ensembles, respectively [58]. For example, biexponential fits have been applied to PL transients with both an initial fast and subsequent slow component, which have been respectively attributed to recombination at defects at the surface and in the bulk of the material [77, 214]. Alternatively, stretched exponentials and functions including the bimolecular band-to-band recombination of charge carriers have been used [79, 83], as detailed in Section 2.4. In order to confirm that the transients in Fig. 5.1a were best described by power-law decays, the following procedures were used to obtain the fits to the 10 K PL transient depicted in Fig. 5.1b of the main text:

- $I_{\mathrm{me}}(t)$ in Equation 2.3 was fitted between 20 and 100 ns, over which the data appeared to follow a roughly linear trend when depicted on a logarithmic intensity

scale, resulting in $k_1 = 1.96 \times 106$ s^{-1}.

- $I_{\mathrm{be}}(t)$ in Equation 2.4 was fitted between 1 and 100 ns, beyond which the fit did not converge well. The resultant decay lifetimes were τ_1= 2.22 ns and τ_2 = 39.8 ns.

- $I_{\mathrm{se}}(t)$ in Equation 2.5 was fitted to the data up to 1 μs, beyond which the fit did not converge well. The fit converged with β=0.1939 and τ_c=1.51$\times$ 10-2 ns.

- With k_2 fixed at 10^{-10} cm^3 s^{-1} [19], Equation 2.7 was fitted between 1 ns and 100 μs, beyond which the fit did not converge well. The fit converged with $k_1 = 2.21 \times 10^4$ s^{-1} and n_0 at its upper bound of 10^{18} cm^{-3} .

- $I_{\mathrm{pl}}(t)$ from Equation 2.8 was fitted to the data over the entire time range, with α = -1.027 $\pm$ 0.003. For the 20 and 30 K data, α = -1.071 $\pm$ 0.004 and -1.19 $\pm$ 0.01 respectively.

As shown in Fig. 5.1b, other than $I_{\mathrm{pl}}(t)$ these functions are unable to describe adequately the power-law PL decay at 10 K over the six decays of time, despite appearing to fit credibly on a semi-logarithmic scale over a shorter temporal range (as shown in the inset). Hence this novel measurement of the PL dynamics for a hybrid perovskite over six decades of time reveals the power-law nature of the charge-carrier recombination dynamics.

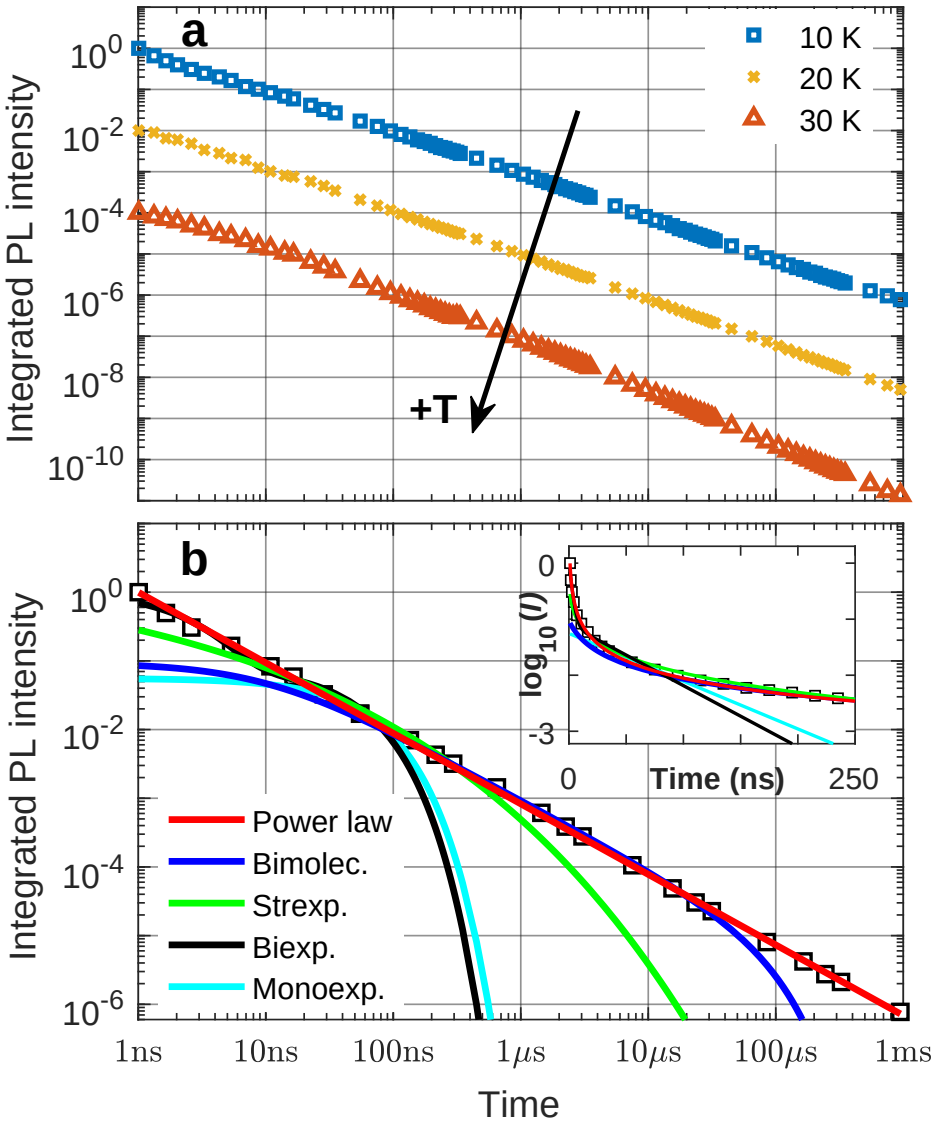

Figure 5.1: Power-law time dependence of PL intensity. **(a)** Spectrally integrated PL intensity transients of $FAPbI_3$ at 10 K, 20 K and 30 K over six decades of time after excitation, measured for an excitation fluence of 390 nJ/cm^2. The curves are displaced vertically by factors of 100 for clarity. **(b)** Comparison of power-law fit to PL transient recorded at 10 K with fits of the other functions commonly used to describe PL time decay in hybrid perovskites (combined mono- & bi-molecular decay, blue; stretched exponential decay, green; bi-exponential decay, black; mono-exponential decay, cyan). Details of the fits are given in Section 2.4. The inset shows the difficulty in distinguishing between these fitting functions on a semi-logarithmic scale over shorter timescales, where I is the spectrally integrated PL intensity.

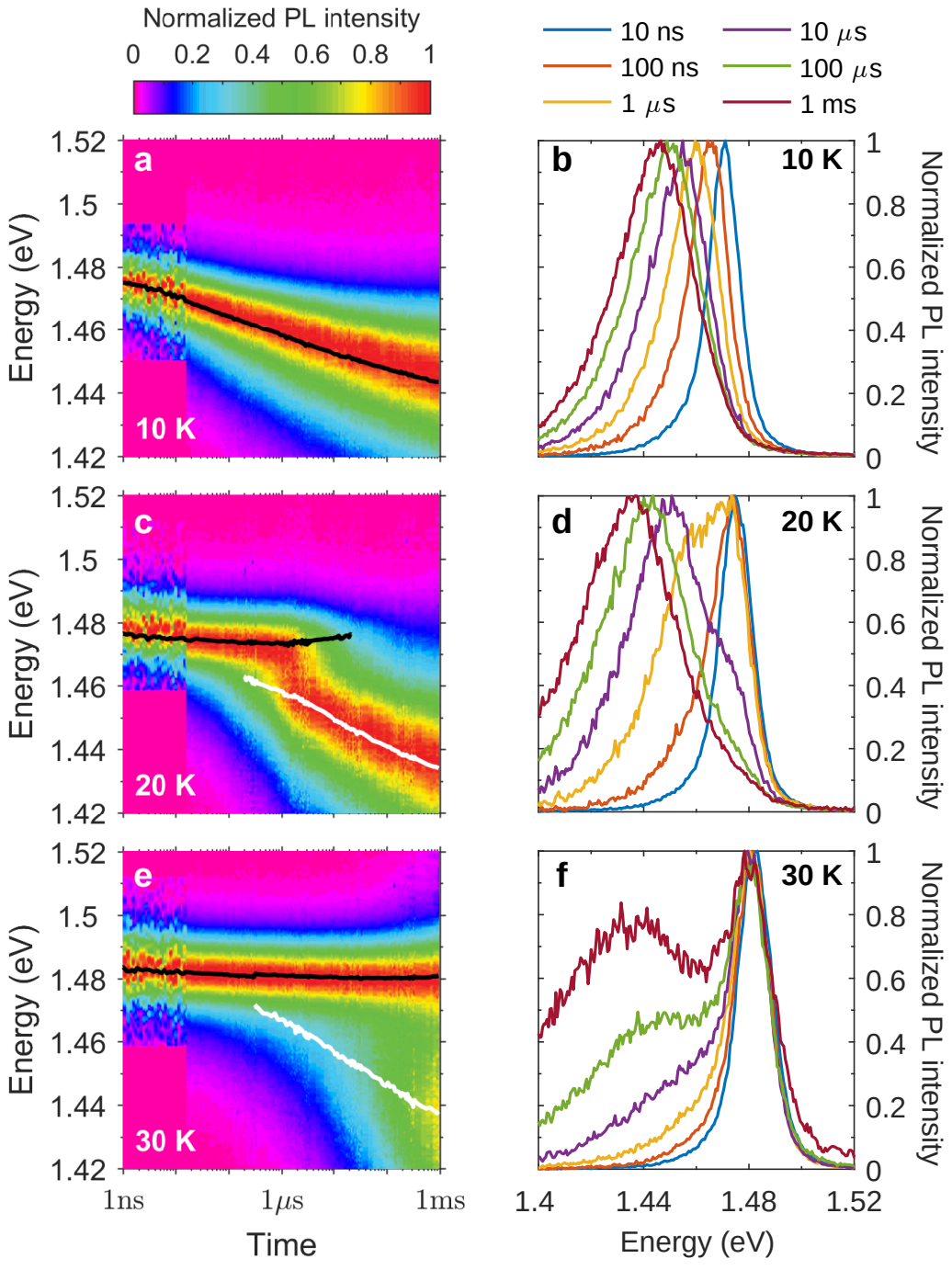

Figure 5.2: Colour plots of the normalized time-dependent PL spectra of $FAPbI_3$ at times between 1 ns and 1 ms and under an excitation fluence of 390 nJ/cm^2, with selected spectra, at temperatures of **(a,b)** 10 K, **(c,d)** 20 K and **(e,f)** 30 K. The spectra were fitted with one or two Gaussian peaks, whose central energies are indicated by the solid black and white lines.

Power-law luminescence decays have previously been identified in a wide range of materials other than hybrid perovskites [89] and are indicative of the involvement of localized trap states in charge-carrier recombination [91]. Such decays mathematically arise from the superposition of many exponentially decaying components [85], which can physically result from the dependence of the depopulation rate of traps on their energetic depth or spatial separation [85, 87, 91]. Whereas a biexponential fit may account for two decay components, a power law expresses the limit if there is a continuous distribution of recombination rates.

As detailed in Section 2.5, models in which the distribution of traps is either exponential in energy or spatially random analytically yield a power-law PL intensity decay to a very good approximation over several decades of time [85, 87]. The presence of an energetic distribution of traps is also validated by the observation of a redshift of the PL spectrum with time (Fig. 5.2), which is consistent with the relaxation and thermalization of charge-carriers within a tail of sub-bandgap trap states [215]. Thus, the time-dependence of the PL intensity and spectra at 10 K suggests that the traps in these materials form a band tail (as depicted in Fig. 2.7), rather than energetically discrete levels. Such band tails have been shown to be a common feature in a wide range of other semiconductors [216, 217], where they result from structural disorder due to defects, doping or non-uniformity of composition. This disorder causes local potential minima in the conduction or valence bands, which form a density of band tail states [123] that is typically modelled as either Gaussian or exponential [212]. The observation of Urbach tails [122, 123, 125] in the absorption spectrum of $MAPbI_3$ suggests that sub-bandgap states may be best described by an exponential distribution for hybrid lead iodide perovskites.

5.2.2 Temperature dependence of PL

To establish the energy landscape of the trap distribution, the temperature dependence of the time-integrated PL spectra of $FAPbI_3$ was investigated for a range of excitation fluences (Fig. 5.3). At higher temperatures, the PL spectra display a single dominant peak (black line, Fig. 5.3) whose energy is independent of excitation fluence. This peak shifts monotonically upwards in energy from about 1.475 eV at 10 K to 1.495 eV at 50 K in accordance with the intrinsic behaviour of the bandgap energy, which is known to blueshift with increasing temperature in hybrid lead halide perovskites [72, 180]. This blueshift is the opposite of that expected for typical semiconductors such as Si, Ge and GaAs [179], and has been attributed to the stabilization of band-edge states during thermal expansion of the lattice [114, 180]. Indeed, the same atypical trend has been observed in the bandgaps of lead chalcogenides [218]. The blueshift of the higher-energy peak with temperature and its absence of saturation behaviour suggest that this emission arises from the recombination of charge-carrier pairs delocalized in the band states of the semiconductor. These charge pairs most likely exist as free excitons since the thermal energies for the data shown in Fig. 5.3 are below the exciton binding energy (14 meV) [213] for the low temperature phase of $FAPbI_3$.

A second, very apparent feature in the PL at very low temperatures is a broad, lower-energy peak (white line, Fig. 5.3) which exhibits saturation behaviour, appearing less intense and higher in emission energy as the excitation fluence is increased (see also Fig. 5.5). The appearance of low-energy PL emission peaks in hybrid lead halide perovskites has been ascribed in previous studies to charge-carrier recombination at localized states [73, 176, 208, 219–222]. Remarkably, it is here found that such trap-mediated emission exhibits an anomalous energy shift with increasing temperature: while the peak energy of the band-edge emission from hybrid lead halide perovskites (black line) blue-shifts with increasing temperature [114], that of the trap-related emission (white

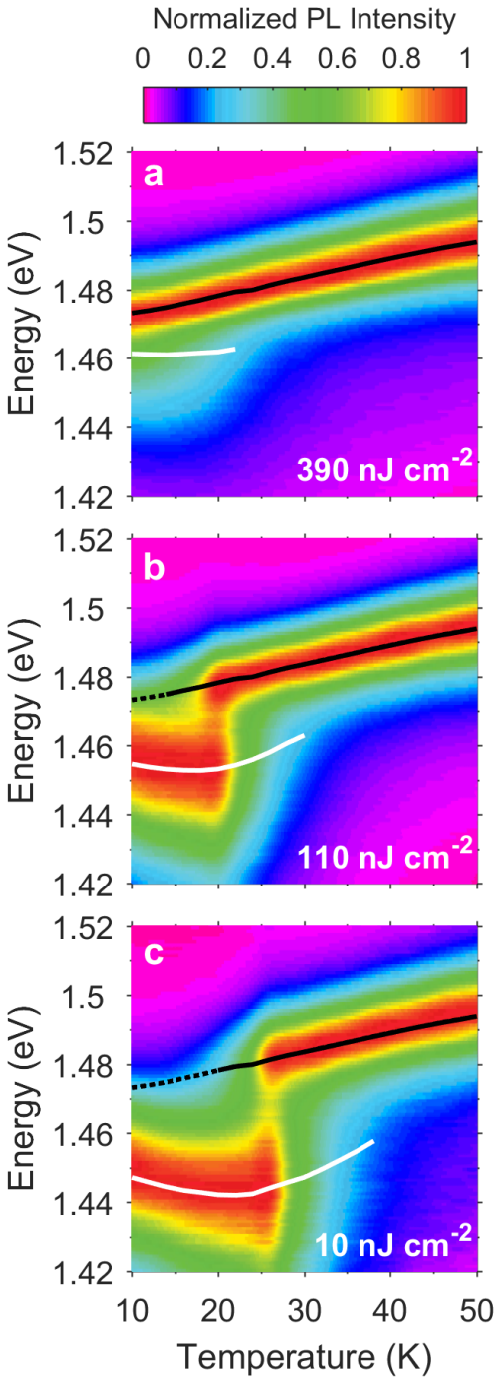

Figure 5.3: Temperature dependence of PL at different excitation fluences. Colour plots of the normalized time-integrated PL spectra of $FAPbI_3$ at temperatures between 10 and 50 K, under excitation fluences of **(a)** 390 nJ/cm^2, **(b)** 110 nJ/cm^2 and (c) 10 nJ/cm^2. The spectra were fitted with two Gaussian peaks, whose central energies are indicated by the solid black and white lines. The position of the higher energy peak at the lower fluences is inferred from the highest fluence data and plotted as dotted black lines. PL spectra at selected temperatures from these colour plots are presented in Fig. 5.4.

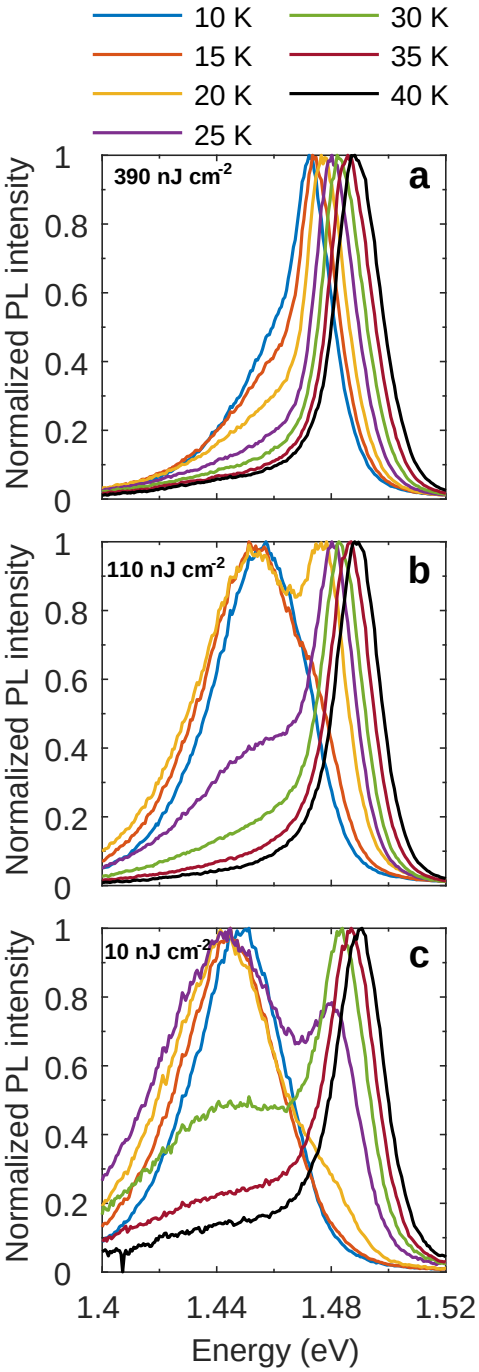

Figure 5.4: Time-integrated PL spectra at selected temperatures for $FAPbI_3$ under excitation fluences of **(a)** 390 nJ/cm^2, **(b)** 110 nJ/cm^2 and **(c)** 10 nJ/cm^2.

line) initially exhibits a clear red-shift. With increasing temperature, this effect leads to a widening energy gap, or relative Stokes shift, of the trap-mediated emission with respect to the free-exciton emission, which begins to reverse again for temperatures above ≈25 K. The relative Stokes shift differs from the conventional Stokes shift in its use of the energy of the free exciton emission rather than the absorption onset as the reference point for the redshift [223]. Nonetheless, the fluence-independence of the free exciton PL peak over the measured range of fluences (as shown in Fig. 5.3), combined with the temperature-independence of the exciton binding energy, ensure that changes in the energy of the free exciton PL peak with temperature reflect those of the band edge. The observed trend in the relative Stokes shift is at odds with the expected behaviour of PL from discrete trap states or a well-defined indirect energy gap situated just below the band gap. In both cases, the fixed energetic offset of the trap or indirect transition from the direct band edge would be equal to the (temperature-independent) relative Stokes shift as well as the thermal energy $k_{\mathrm{B}}T$ at which the peak disappeared.

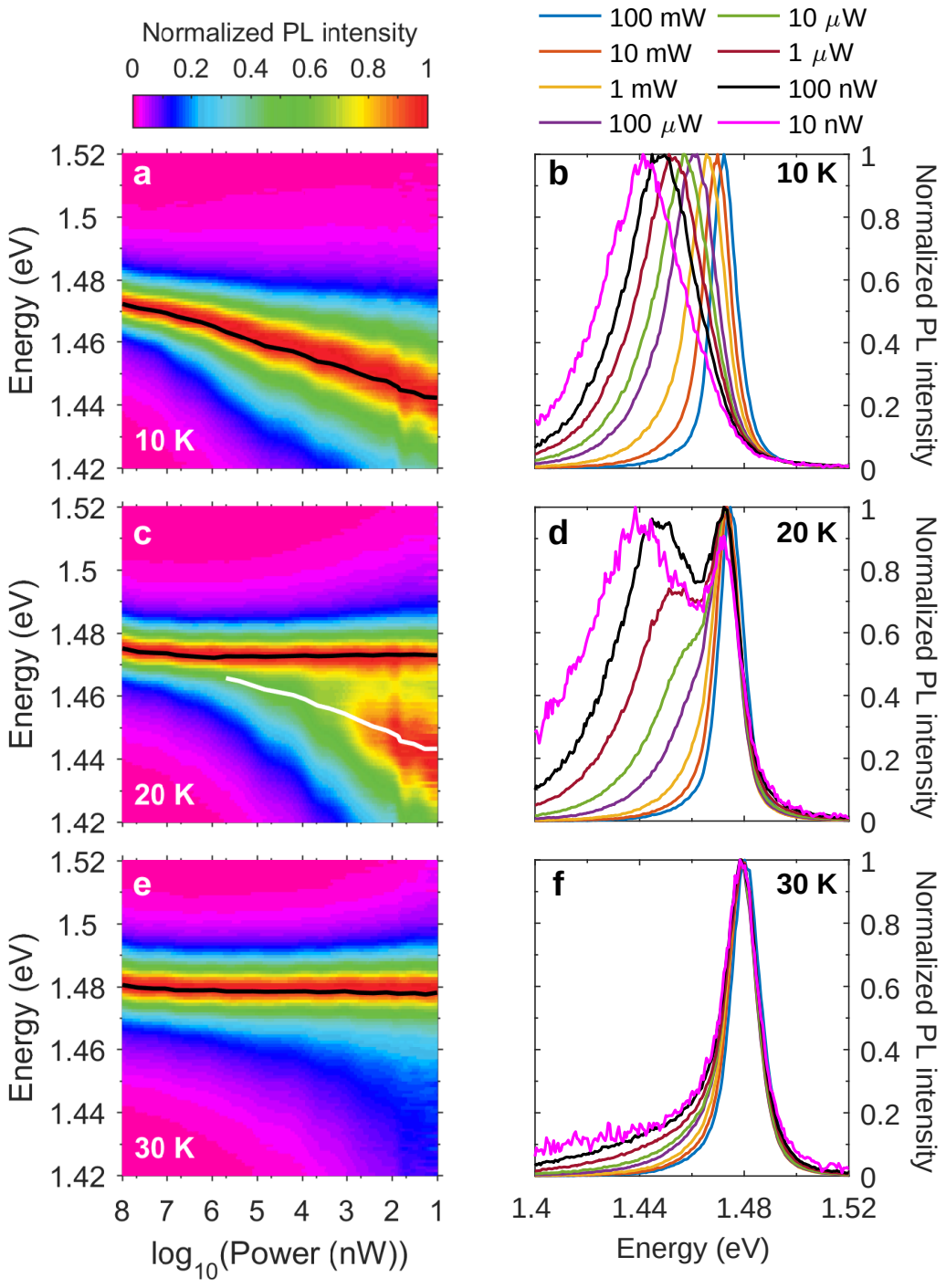

Figure 5.5: Color plots of the normalized steady-state PL spectra of $FAPbI_3$ at excitation powers between 10 nW and 100 mW, with selected spectra, at temperatures of **(a,b)** 10 K, **(c,d)** 20 K and **(e,f)** 30 K. The spectra were fitted with one or two Gaussian peaks, whose central energies are indicated by the solid black and white lines.

5.2.3 Relative Stokes shift

Here, the proposal is instead advanced that the initial anomalous redshift (increased relative Stokes shift) arises from the presence of an energetic distribution of trap levels in the hybrid perovskite. At zero temperature, charge-carriers have no thermal energy to move between sites and are therefore distributed randomly across the density of traps. With increasing temperature, sufficient thermal energy becomes available to activate the charge carriers over shallow barriers, allowing them to relax to deeper localized states before they recombine [224] thus decreasing the PL energy and increasing the relative Stokes shift. With further increase in temperature, the rate of hopping between states and phonon population both increase, resulting in the charge carriers becoming thermalized across the trap density of states (DOS) [212, 225]. The charge carriers therefore occupy a broader distribution of states with a higher average energy as the temperature increases, resulting in a blueshift [212] (decreased relative Stokes shift) and broadening [72] of the PL emission. Such phenomena have also been observed in inorganic semiconductors such as AlGaN, InGaN and AlInGaN, [224] where they have similarly been attributed to the motion of charge carriers within a band tails [212, 224, 225]. Here, this study reveals that hybrid perovskites exhibit very similar trap-mediated emission with anomalous Stokes shifts. Importantly, shown below, a quantitative analysis of this behaviour allows the direct extraction of the characteristic energy of the trap DOS that gives rise to these effects.

To enable such quantitative analysis, the relative Stokes shifts from the data in Fig. 5.3 were extracted. The free exciton and band tail PL peaks were fitted with Gaussian functions to determine the peak energies, which are indicated in Fig. 5.3 by the black and white lines, respectively. The relative Stokes shift is given by the energy difference between the peaks (i.e. the energetic separation between the black and white lines). When the free exciton peak was not visible at low temperatures and fluences, the aforementioned fluence independence of the peak allowed its position to be inferred from the spectra

taken at the highest fluence. The extracted relative Stokes shift is plotted in Fig. 5.6 as a function of temperature for three different excitation fluences. Under the lowest excitation fluence of 10 nJ cm^{-2} implemented in this study, the largest relative Stokes shift of ≈37meV is reached at a temperature of 25 K. This is a consequence of the low charge-carrier density, which allows a majority of photo-excited carriers to relax deep into the band tail before they recombine. As the excitation fluence is increased, the higher initial charge-carrier density results in the filling of trap states, and the band-tail emission originates predominantly from higher-energy states closer to the band edge.

5.2.4 Quantitative modelling of anomalous relative Stokes shift

This interpretation of the anomalous relative Stokes shift can be verified by use of quantitative models, which allow the determination of the characteristic energy scale of the trap distribution. Unlike trap states associated with energetically well-defined defects, such as vacancies, substitutions or interstitials [68, 117, 226], the energy scales at which band tail PL emission occurs is not determined by a single energetic offset from the band edge but rather the charge-carrier occupation within a broader density of trap states. Here, two different approaches are explored that have in the past been successfully used to describe the mechanisms of charge-carrier relaxation within band tails [95]. These are, first, a multiple-trapping model in which energetic relaxation occurs by thermal excitation to a shallower state followed by subsequent recapture (see Fig. 5.6a for a schematic) and, second, a hopping model in which charge-carriers tunnel directly between states (Fig. 5.6c). The two mechanisms, respectively, represent the limits of low and high overlap between band-tail states [95], and therefore to assess properly the validity of the energy distribution extracted, one model of each type is considered: an elementary multiple-trapping model which produces an analytic function describing the relative Stokes shift, and a more sophisticated Monte Carlo model, which is a more

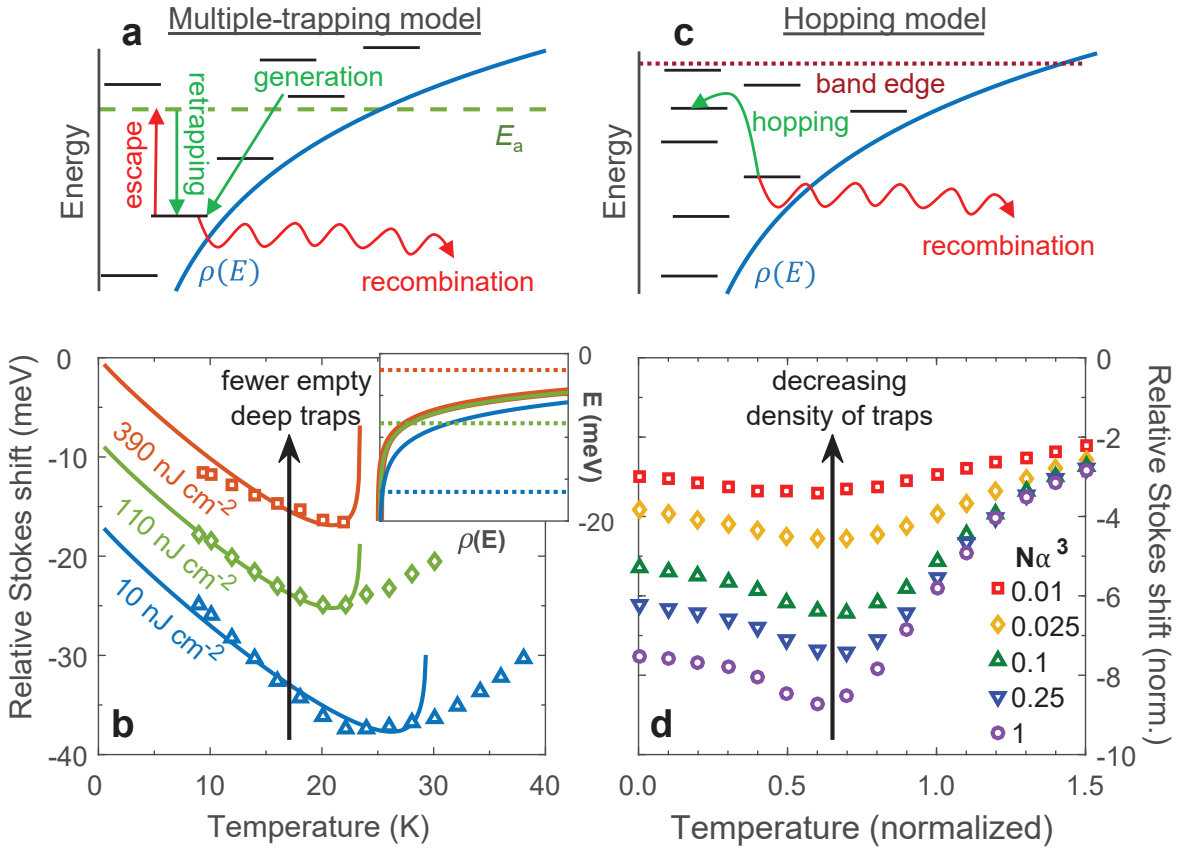

Figure 5.6: Models replicating the anomalous relative Stokes shift. **(a)** and **(c)** show schematics of the Multiple Trapping (Rate Equation) and Hopping (Monte Carlo) models of the anomalous relative Stokes shift respectively. In **(b)**, the relative Stokes shift observed in $FAPbI_3$ is plotted, for excitation fluences of 390 nJ/cm^2 (red), 110 nJ/cm^2 (green) and 10 nJ/cm^2 (blue). Fits to these data using the rate equation model are plotted as the matching coloured lines. The inset shows the trap distributions corresponding to these fits, with the dotted lines showing the E_a values. The anomalous temperature dependence of the relative Stokes shifts can also be reproduced by Monte Carlo simulation of the hopping of charges in an exponential band tail, as shown in **(d)** for a range of trap state densities (represented by $N\alpha^3$). Here, the simulated relative Stokes shift and temperature are normalized against ϵ_0 and ϵ_0/k_B respectively, where ϵ_0 is the inverse slope of the band tail. Simulated PL spectra at selected temperatures are presented in Fig. 5.8.

physically accurate mechanism but requires more intense computational effort to model the data. In both cases, it is considered that approximating the trap density of states by exponential tails is the most realistic scenario for hybrid lead iodide perovskites. These models return a value of the characteristic energy ϵ_0 corresponding to the inverse slope of the trap density of states $\rho(\epsilon) \propto e^{E/\epsilon_0}$, which is defined for trap energies below the band edge at $E = 0$. Although 63 % of the traps in the tail lie above ϵ_0, the tail naturally

extends to energies much deeper into the band gap, from where emission can still occur. As mentioned above, over the temperature range modelled in Fig. 5.6, the charge carriers are likely to be predominantly be excitons since the thermal energy below 40 K is less than the exciton binding energy in $FAPbI_3$ in this phase. Nonetheless, the two models discussed below may apply generally to either excitons, or electrons and holes, moving and recombining within a localised density of states. In the latter case, only one sign of charge carrier may be considered to be mobile (cf. Subection 2.5.2 and Ref. [85]) such that only its motion is modelled until recombination occurs when oppositely-charged carriers meet.

5.2.4.1 Multiple-trapping model

As a first approach, the multiple-trapping model [227] considers the mechanisms by which charge-carriers may arrive at and leave states in the band tail to yield a rate equation describing the carrier dynamics (see schematic in Fig. 5.6a).

This model assumes that charge-carriers may only escape traps by thermal activation (with attempt-to-escape rate ν_{e}) to unoccupied states above energy E_{a}, from which they may be recaptured before eventually recombining radiatively (with lifetime τ_{r}). The non-monotonic temperature dependence of the relative Stokes shift results from upward redistribution of charge-carriers within the band tail by thermal escape coming to dominate over the downward retrapping rate at higher temperatures.

5.2.4.1.1 Rate equation model for anomalous relative Stokes shift

Li et al. [227–229] describe the rate of change of carrier population density $n(E,T,t)$ in localized states of energy E, at time t after excitation and at temperature T by the following rate equation [227]:

$$\frac{dn(E,T,\ t)}{dt} = G\left(E,t\right)\ - \frac{n\left(E,T,t\right)}{\tau_{\mathrm{r}}} - n\left(E,T,t\right)\nu_{\mathrm{e}}e^{\,-\,E_{\mathrm{a}}/k_{\mathrm{B}}T} + \gamma_{\mathrm{c}}\frac{\rho(E)}{P}\lambda_{\mathrm{a}}(T,t). \quad (5.1)$$

The first term on the right is the carrier generation rate, given by $G(E) = \kappa\ \rho(E)$, where κ is a constant of proportionality and $\rho(E)$ is the band tail density of states. The second term on the right describes the depopulation due to radiative recombination, which the carriers undergo with typical lifetime τ_{r} (higher-order recombination processes are neglected in this treatment). The third term on the right gives the rate of thermal escape to the unoccupied states above energy E_{a}, where ν_{e} is the attempt-to-escape rate. The final term represents the rate of carrier recapture at localized states, where λ_{a} is the rate at which carriers are thermally activated away from all the localized states, as given by

$$\lambda_{\mathrm{a}}(T) = \int_{-\infty}^{\infty} n(E', T)\nu_{\mathrm{e}} e^{-(E_{\mathrm{a}} - E')/k_{\mathrm{B}}T}\mathrm{d}E'. \tag{5.2}$$

Some proportion (given by the recapture coefficient, γ_{c}) are recaptured by localized states, of which a fraction $\frac{\rho(E)}{P}$ are at energy E, where $P = \int_{-\infty}^{\infty} \rho(E')\ \mathrm{d}E'$. E_{a} is an energy below which the localized states are all occupied by carriers, analogous to the quasi-Fiermi level of the localized state distribution [229].

Li et al. consider steady state $\left(\frac{\mathrm{d}n(E,T,t)}{\mathrm{d}t} = 0\right)$ conditions involving continuous carrier generation in order to derive the peak position of $n(E, T)$ at different temperatures, which represents the peak PL energy from the localized states. However, here the PL was measured under pulsed excitation conditions. The following treatment shows that the time-integrated PL peak has the same temperature dependence as in the steady-state case.

Under pulsed excitation, the time between pulses can be divided into two periods: δt, during which the excitation occurs, and Δt, which represents the rest of the pulsation period. It is assumed that δt is sufficiently short that all carrier generation occurs during this period, while the processes of recombination, thermal escape and recapture are confined to Δt. The net result of the three processes occurring during Δt is to remove all of the carriers generated in the localized states at energy E during δt, which

can be expressed in the following equality:

$$N_{\text{generated}}(E,T) = N_{\text{radiated}}(E,T) + N_{\text{escaped}}(E,T) - N_{\text{captured}}(E,T) \tag{5.3}$$

where N_x is the absolute value of the carrier population density added or removed from localized states of energy E by process x during the course of an excitation cycle.

Considering each term in Equation 5.3 in turn:

$$N_{\text{generated}}(E,T) = \int_{\delta t} G(E)\,\mathrm{d}t = \mu\rho(E), \text{where } \mu \text{ is a constant of proportionality.} \tag{5.4}$$

$$N_{\text{radiated}}(E,T) = \frac{1}{\tau_{\text{r}}}\int_{\Delta t} n(E,T,t)\mathrm{d}t \tag{5.5}$$

$$N_{\text{escaped}}(E,T) = \nu_{\text{e}} e^{-(E_{\text{a}}-E)/k_{\text{B}}T}\int_{\Delta t} n(E,T,t)\mathrm{d}t \tag{5.6}$$

$$N_{\text{captured}}(E,T) = \int_{\Delta t} \gamma_{\text{c}}\lambda_{\text{a}}(T,t)\frac{\rho(E)}{P}\mathrm{d}t \tag{5.7}$$

$$= \gamma_{\text{c}}\frac{\rho(E)}{P}\int_{-\infty}^{\infty}\nu_{\text{e}} e^{-(E_{\text{a}}-E')/k_{\text{B}}T}\int_{\Delta t} n(E,T,t)\mathrm{d}t\mathrm{d}E' \tag{5.8}$$

Now let $m(E,T) = \int_{\Delta t} n(E,T,t)\mathrm{d}t$, which is the mean charge-carrier distribution over the period Δt, so Equation 5.3 becomes

$$\mu\,\rho(E) = \left(\frac{1}{\tau_{\text{r}}} + \nu_{\text{e}} e^{-(E_{\text{a}}-E)/k_{\text{B}}T}\right) m(E,T) - \gamma_{\text{c}}\frac{\rho(E)}{P}\int_{\infty}^{\infty}\nu_{\text{e}} e^{-(E_{\text{a}}-E)/k_{\text{B}}T} m(E',T)\mathrm{d}E' \tag{5.9}$$

$$= \left(\frac{1}{\tau_{\text{r}}} + \nu_{\text{e}} e^{-(E_{\text{a}}-E)/k_{\text{B}}T}\right) m(E,T) - \gamma_{\text{c}}\frac{\rho(E)}{P}\lambda'(T) \tag{5.10}$$

Where $\lambda'(T)$ represents the total number of carriers which escaped from localized states over the course of Δt. Therefore, $m(E,T) = A(T)\,B(E,T)$, where

$$A(T) = \mu + \frac{\gamma_{\text{c}}}{P}\lambda'(T) \tag{5.11}$$

$$B(E,T) = \frac{\rho(E)}{\frac{1}{\tau_{\text{r}}} + \nu_{\text{e}} e^{-(E_{\text{a}}-E)/k_{\text{B}}T}} \tag{5.12}$$

Since $A(T)$ is a function of T only, $B(E,T)$ describes the shape of the PL spectrum. This is the same result obtained for the steady-state, continuous excitation case by Li *et al.*. The peak of the spectrum occurs when $\partial B(E,T)/\partial E = 0$.

Li *et al.* consider the more involved case of a Gaussian density of states, but here an expression is derived for the peak energy for an exponential density of states (DOS) of the form $\rho(E) \propto e^{E/\epsilon_0}$, where ϵ_0 represents the energy scale for the depth of the trap DOS. In this case, when $\partial B(E,T)/\partial E = 0$:

$$\frac{1}{\epsilon_0}\left(e^{-(E_a - E)/k_B T} + \frac{1}{\nu_e \tau_r}\right) = \frac{1}{k_B T} e^{-(E_a - E)/k_B T} \tag{5.13}$$

$$e^{-(E_a - E)/k_B T}\left(1 - \frac{\epsilon_0}{k_B T}\right) = -\frac{1}{\nu_e \tau_r} \tag{5.14}$$

$$E_{peak} = E_a + k_B T \ln\left[\frac{1}{\nu_e \tau_r}\frac{k_B T}{\epsilon_0 - k_B T}\right] \tag{5.15}$$

The model is divergent for $\epsilon_0 \leq k_B T$.

5.2.4.1.2 Application of the multiple-trapping model

In Fig. 5.6b, Equation 5.15 is fitted to the relative Stokes shifts derived from Fig. 5.3, with fitting parameters presented in Table 5.1. As shown in the inset to Fig. 5.6b, the lower charge-carrier concentration at lower fluence results in more traps deep in the band tail being left empty, corresponding to a deeper effective band tail energy scale ϵ_0 and deeper energy E_a up to which state-filling occurs. The value of $\epsilon_0 = 2.5$ meV under the lowest excitation fluence provides the best estimate of the characteristic energy scale of the band tail, though as can be seen from the inset to Fig. 5.6b the occupied states below the dotted line are in fact located far deeper. Indeed, it is not unusual for the deepest states in a band tail to exert a disproportionate influence on charge-carrier behaviour [230], since the tail theoretically descends indefinitely, allowing for broad PL emission from deep states even in a 'shallow' tail. However, as expressed in Equation 5.15, ϵ_0 quantifies the thermal energy above which escape from the band tail states becomes dramatically easier, such that charge-carriers spend most of their time as free excitons and the trap emission fades [231]. Thus, a multiple-trapping model of charge-carrier

recombination within a band tail is able to rationalize the disparity between the energy scales of the maximum relative Stokes shift observed here at the lowest fluences (≈40 meV) and the disappearance of the band-tail PL peak at temperatures corresponding to thermal energies $k_{BT} \approx 3$ meV. Such a shallow band tail is also consistent with the fading of clear power-law decay dynamics and trap-related emission peaks at an increased temperature of 100 K (Fig. 5.7), when charge-carriers (likely free carriers rather than excitons at this temperature) are thermally elevated to the upper levels of the DOS.

Fluence [J cm^{-2}]	ϵ_0 [meV]	E_a [meV]	$\nu_e\tau_r$
390	2.0	-0.7	*[10^5]*
110	2.0	-8.3	*[10^5]*
10	2.5	-16.5	*[10^5]*

Table 5.1: Extracted band tail parameters for rate equation model. Fitted values of band tail depth (σ), filling level (E_a) and ratio of charge-carrier transfer and recombination timescales ($\nu_e\tau_r$). $\nu_e\tau_r$ is assumed to be is independent of excitation fluence and is fixed at 10^5 in the fits here, based on estimates of ν_e and τ_r being of the order of the Debye frequency [232]($\sim 10^{12}$ s^{-1} for $MAPbI_3$) [177], and inverse of the monomolecular rate constant ($k_1 \sim 10^7$ s^{-1} for $FAPbI_3$) [18] respectively.

5.2.4.2 Hopping model

As a second approach, the anomalous relative Stokes shift is modelled as part of a charge hopping mechanism, using a more sophisticated Monte Carlo simulation to follow the relaxation of individual charge-carriers within the band tail [212]. In outline, the charge-carriers are introduced independently to a volume of localized states with randomly distributed positions and energies distributed according to the exponential band tail DOS. When occupying a site, a charge-carrier can either recombine radiatively, or tunnel to an empty site according to the Miller-Abrahams rate in Equation 5.17 [233]. By generating random numbers, the stochastic behaviour of each exciton is simulated, hopping between sites until it eventually undergoes radiative recombination. A histogram of the energies of the sites at which the excitons recombined produces the band-tail PL spectrum.

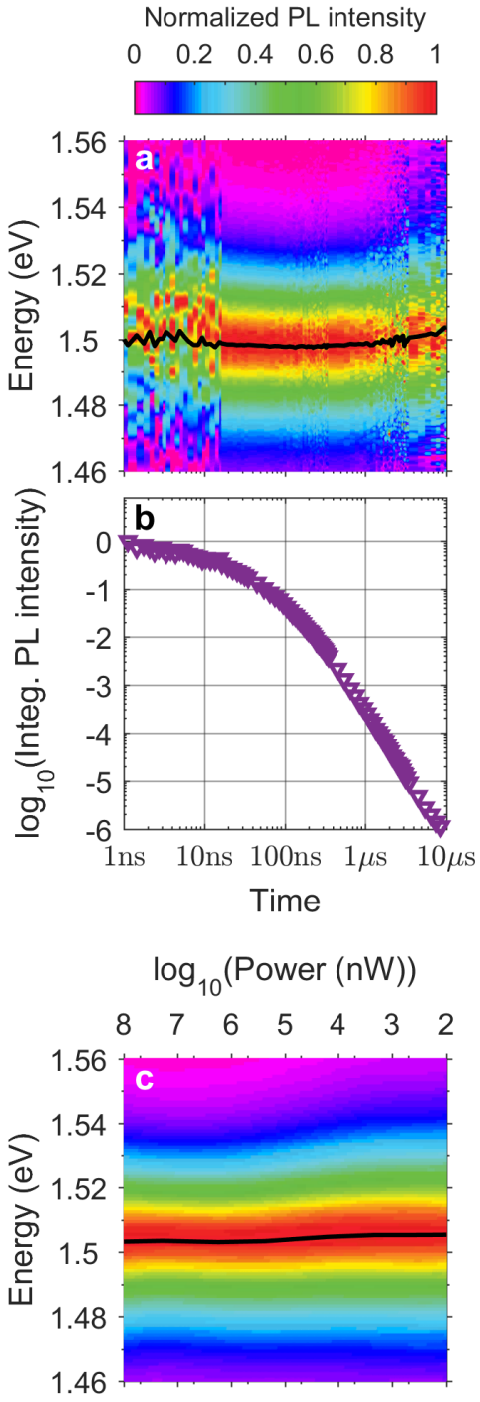

Figure 5.7: **(a)** Colour plot of the normalized time-dependent PL spectra of $FAPbI_3$ at a temperature of 100 K and at times between 1 ns and 1 ms. **(b)**The corresponding spectrally integrated PL intensity transient. **(c)** Colour plot of the normalized steady-state PL spectra of $FAPbI_3$ at a temperature of 100 K and excitation powers between 10 nW and 100 mW. In both colour plots, the spectra were each fitted with a single Gaussian peak, whose central energies are indicated by the solid black line. At 100 K, recombination is likely to be primarily a free carrier process.

5.2.4.2.1 Monte Carlo model of the anomalous relative Stokes shift

Baranovskii et al. simulate the relaxation of excitons within a distribution of localized states using a Monte Carlo technique [212, 234]. Here, the simulation algorithm described in Ref. [212] is used, adapted for a three-dimensional material.

Within the simulation algorithm, the excitons are modelled as single particles moving between localized states, which are randomly distributed in a cube with sides of length $N_0^{1/3}$ containing N_0 sites. The energies of the states are distributed according to the DOS of the band tail, which for an exponential density of states is

$$\rho\left(E\right) = \frac{N}{\epsilon_0} \exp\left(\frac{E}{\epsilon_0}\right) \tag{5.16}$$

where ϵ_0 is the characteristic energy scale for the depth of the trap DOS, E is the trap energy (on a scale where the band edge is at $E = 0$) and N is the concentration of localized states (1 per unit volume).

An exciton occupying site i (with energy E_i) can either recombine radiatively, with characteristic lifetime τ_r (assumed to be independent of temperature or E), or tunnel to an empty site j (with energy E_j) at distance r_{ij} according to the Miller-Abrahams tunnelling rate [233]

$$\nu_{ij} = \nu_\mathrm{e} \exp\left(-\frac{2r_{ij}}{\alpha} - \frac{E_j - E_i + |E_j - E_i|}{2k_\mathrm{B}T}\right) \tag{5.17}$$

where ν_e is the attempt-to-escape frequency and α is the decay length of the localized exciton centre-of-mass wavefunction. Therefore, the total rate of escape from a given site i is $\nu_i = \frac{1}{\tau_r} + \sum_j \nu_{ij}$, where the summation index j runs over all possible hopping sites. Since ν_{ij} falls exponentially with distance and the difference in energy between sites, only the 32 largest terms in the sum were used in the computation.

Excitons are introduced one to the grid of sites at a time, starting from a random site. It is assumed that the charge-carrier density is sufficiently low that excitons

relax independently. For an exciton at site i, a random number ξ_i from a uniform distribution between 0 and 1 is generated to determine the time $t_i^{-1} = -\nu_i \ln(\xi_i)$ until the exciton leaves the site. A second random number then determines whether this is by tunnelling to another site in the band tail, or by recombining. In the former case, t_i is added to the time counter, and the process repeated. In the latter case, the time and energy of the exciton at recombination are recorded, and a new exciton considered, until all n excitons have recombined.

The parameters of the model can be expressed as the dimensionless quantities $\nu_e\tau_r$, $N\alpha^3$ and k_BT/ϵ_0. $\nu_e\tau_r$ describes the degree to which hopping is faster than recombination, $N\alpha^3$ is the fraction of the volume per site which is occupied by the exciton wavefunction, and k_BT/ϵ_0 is the thermal energy normalized by the band tail depth.

For the simulations shown in Fig. 5.6d, $\nu_e\tau_r = 10^5$ (as justified in Table 5.1), $N_0 = 35^3$ and $n = 10^4$. The mean value of the PL energy was treated as the relative Stokes shift [212, 223], and simulated PL spectra at selected temperatures are presented in Fig. 5.8.

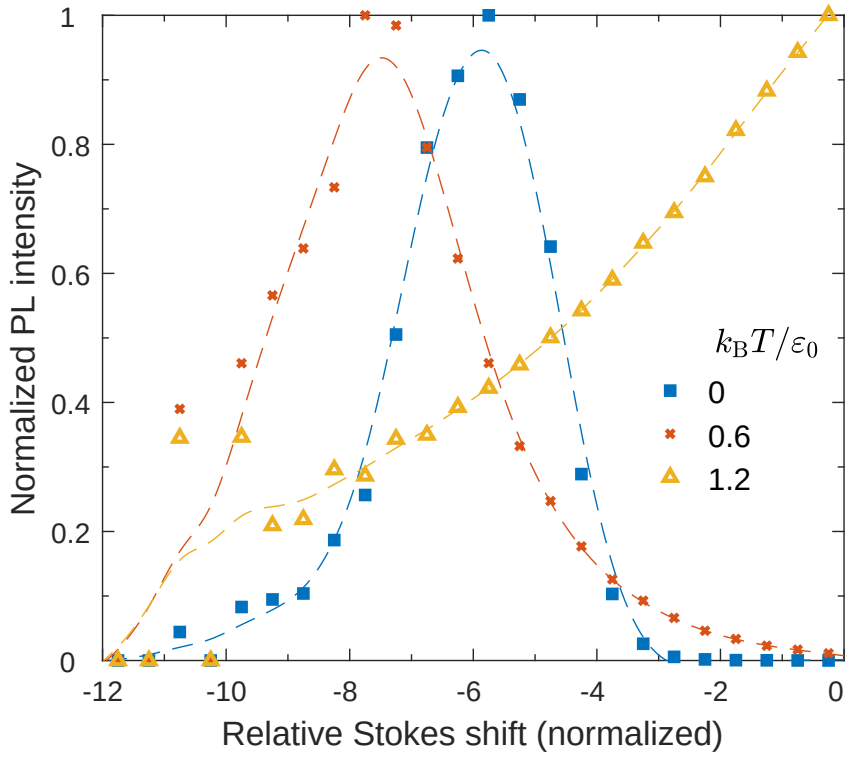

Figure 5.8: Temperature dependence of simulated band-tail PL spectra. PL spectra from Monte Carlo simulations of band-tail recombination at selected values of the normalized temperature k_BT/ϵ_0, where T is the temperature and ϵ_0 is the inverse slope of the band tail. The dashed lines are a guide to the eye for the simulated spectra. The PL energy is expressed as a relative Stokes shift, normalized against ϵ_0. For these simulations, $N\alpha^3 = 0.25$, $\nu_e\tau_r = 105$, $N_0 = 35^3$ and $n = 5 \times 10^5$.

5.2.4.2.2 Application of the hopping model

Simulations of the temperature-dependence of the relative Stokes shift are shown in Fig. 5.6d, for an exponential band tail, again of the form e^{E/ϵ_0}. The relative Stokes shift and temperature are both normalized, against ϵ_0 and ϵ_0/kB respectively. Each data series represents simulations for different values of the dimensionless parameter $N\alpha^3$, which quantifies the fraction of the volume per trap site that is occupied by the exciton wavefunction. The simulations reproduce the non-monotonic temperature dependence of the relative Stokes shift observed in Fig. 5.3. Decreasing $N\alpha^3$ represents a reduction in the concentration of localized states, corresponding to the lower availability of unoccupied sites for charge-carriers to hop to when the excitation fluence is higher. Indeed, the

experimentally observed reduction in magnitude of the anomalous relative Stokes shift with increasing fluence is also observed at lower $N\alpha^3$. Notably, the maximum simulated relative Stokes shift occurs at approximately 0.6 ϵ_0/k_B, independently of the choice of $N\alpha^3$ or other parameters [223]. Since the maximum experimental relative Stokes shift occurs at between 20 and 25 K, this allows the band tail depth to be estimated from the Monte Carlo model as $\epsilon_0 \approx 3$ meV, in excellent agreement with the rate equation model.

5.3 Conclusion

These results provide strong evidence that there is an exponential band tail of states in $FAPbI_3$ with a characteristic energy of 3 meV, obtained for both models irrespective of their opposing limits of low and high overlap between band-tail states. Power-law PL decays and anomalous Stokes shift are both features which necessitate the presence of an energetic distribution of trap states rather than well-defined defect levels. Band tails arise from continuous energetic disorder, which is not entirely unexpected in hybrid perovskites whose bandgaps are known to vary between films fabricated under different conditions [235, 236]. By drawing together previous findings, it is proposed that the origin of the band tail states in $FAPbI_3$ may lie in the rotational freedom of the polar organic cation [178], which has been identified as a source of structural disorder in $MAPbI_3$ [237]. Though less polar, the FA cation is larger than the MA cation and so distorts the perovskite lattice more [180]. In the low-temperature orthorhombic phase [213] of these materials, the *dynamic* rotational motion of the cations is frozen out, [160, 213, 238], but there remains *static* disorder and a shallow, varying potential from the long-range correlated orientations of the otherwise randomly oriented cation dipoles [238, 239]. The local band minima and maxima resulting from these electrostatic potential fluctuations are prime candidates for localised states which form band tails [239, 240]. Such a model can also account for the power-law decay of the PL, since oppositely-charged carriers are spatially separated

within localized states randomly distributed in space, and can therefore only recombine after tunnelling [240]. The degree of the energetic disorder in this model could be tuned by substitution for the FA cation. Notably, this analysis can rule out the dominance of alternative trapping mechanisms that would be associated with discrete energy levels, such as specific elemental vacancies, substitutions or interstitital, or the presence of a specific (discrete) indirect energy gap situated energetically just below the direct gap.

This study reveals analogies with other, more established materials for photovoltaic applications. Energetic band tails have been found to feature in several such semiconductors, including Si, GaAs and CIGS ($CuIn_xGa_{1-x}Se_2$) [122]. An analysis of the energetic distribution of tail states is important for assessing a material's potential for photovoltaic applications because relaxation of charge carriers into the tail states results in a loss of open-circuit voltage V_{oc} relative to the bandgap energy. In $FAPbI_3$ solar cells at room temperature, the open-circuit voltage deficit relative to the bandgap was found to be ≈540 meV, which is comparable to CIGS but a greater deficit than for GaAs [122]. The energy scale of the band tail here observed in $FAPbI_3$ is comparable to the Urbach energies of approximately 1.5 and 10 meV calculated for GaAs and crystalline Si respectively at cryogenic temperatures [241]. Given that the room-temperature Urbach energy (15 meV [122, 124]) of $MAPbI_3$ is also in the same range as other common photovoltaic materials (GaAs, 7 meV [242]; crystalline Si, 11 meV [122]: amorphous Si 40 meV [90, 243]; CIGS, 20 meV [244]), it would appear that this study's estimate of $\epsilon_0 = 3$ meV is relatively typical for an inorganic semiconductor at low temperature, where the lower thermal disorder (which scales with k_BT) results in broader band tails [122].

The relative shallowness of the band tail may also be a contributing factor to the high charge-carrier mobility observed for $FAPbI_3$ [18]. In addition, these findings can clarify the thermally-stimulated current peak observed by Baumann et al. at 27 K (corresponding to 2.3 meV) [112], and they suggest that long-lived PL components observed at room

temperature [214] may result from slow residual charge-carrier recombination deep within the band tail. The value of 3 meV determined here for the characteristic energy of $FAPbI_3$ is shallower than the typical value of 15 meV measured for the Urbach energy in thin films of $MAPbI_3$, which may partly be due to these Urbach measurements being taken at room temperature. A direct comparison at low temperature is not however possible, due to the disorder related to the incomplete phase transition which $MAPbI_3$ undergoes near 160 K which results in the formation of additional trap states in the low-temperature orthorhombic phase [58, 72, 114]. These traps most likely constitute inclusions of the high-temperature tetragonal phase [181, 221] and do not appear in $FAPbI_3$ [221]. Additional emission peaks due to these traps appear at energies ranging from ≈85 meV [69, 114, 181] to ≈300 meV [245] below the free exciton emission, showing strong inhomogeneous broadening [72] and precluding the observation of emission from a band tail of comparable characteristic energy to that observed here in $FAPbI_3$. The lower intrinsic degree of material disorder in $FAPbI_3$ may also contribute to the shallowness of the band tail [72].

6

Optoelectronic and structural properties of $Cs_2AgBiBr_6$ double perovskite

In preparation as a manuscript to be submitted as Ref. [246].

It is clear from Section 2.8 that having a direct band gap in the visible range is important for the photovoltaic success of metal halide double perovskites, and such a goal requires an understanding of the connection between the structure and optical properties of these materials. Therefore, in this study the temperature dependence of the PL and absorbance spectra of lead-free $Cs_2AgBiBr_6$ single crystals and thin films are measured, and correlated with the low-temperature structural phase transition from cubic to tetragonal at $T_S \approx 122$ K [246]. For both the single crystals and thin films, time-resolved PL measurements indicate the presence of a fast charge-carrier recombination mechanism which disappears at the transition from the tetragonal to the cubic phase, suggesting that it may be associated with strain at boundaries between crystalline twins in the tetragonal phase. The temperature-dependence of the indirect bandgap of this material is also tracked, while the novel use of high-quality evaporated thin films of $Cs_2AgBiBr_6$ allows the temperature-dependence of the direct bandgap and its associated exciton energy to be followed, which was not possible for the optically thick single crystal

samples. The exciton energy also exhibits a distinct change that correlates with T_S. Together, these results not only elucidate the behaviour of the electronic transitions in $Cs_2AgBiBr_6$ but also indicate that consideration of the structural phase of double perovskites will be necessary when trying to modify their electronic properties.

6.1 Experimental details

Thin film and single-crystal samples of $Cs_2AgBiBr_6$ were grown as described in Subsection 3.3.2. The thin films were 300 nm thick and mounted on z-cut quartz substrates, while the single crystals were approximately 1 mm long in each direction. The samples were mounted in a gas-exchange helium cryostat, and PL spectra and transients were taken as the sample was heated over temperatures from 4 to 295 K in increments of between 5 and 25 K. A laser intensity of 62 W cm^{-2} was used when obtaining the PL spectra, and a fluence of 210 nJ cm^{-2} for the PL transients. To measure the reflectance and transmittance spectra, an FTIR spectrometer was used, configured with a tungsten halogen lamp illumination source, a CaF_2 beamsplitter and a silicon detector. The samples were mounted in a gas-exchange helium cryostat.

6.2 Results

6.2.1 Temperature-dependent absorption and PL spectra

To characterise the optical properties of $Cs_2AgBiBr_6$, the absorbance spectra of a single crystal and a thin film of the material were measured over temperatures from 5 to 295 K in increments of 5 K. Sample spectra at roughly 25 K intervals are shown in Fig. 6.1a for the single crystal, and Fig. 6.1b for the thin film. The single-crystal data exhibit non-zero absorbance at low energies, which can be attributed to their thickness. At between 2.2 and 2.4 eV for the single crystal, a sharp rise in the absorbance occurs which redshifts continuously with increasing temperature. A similar sharp rise has

previously been observed for $Cs_2AgBiBr_6$ single crystals at room temperature, and has been attributed to the indirect bandgap [21, 139, 247]. In order to estimate the energy, E_g^i, of the indirect gap, the quadratic function form $A \propto (E - E_g^i)^2$, was fitted to the energy-dependent absorbance data $A(E)$ at the onset of the rise in absorbance, as shown in Fig. 6.2a and b. This functional form is characteristic of the absorbance onset due to an indirect bandgap [248], and output values of E_g^i range from 1.95 eV at 4 K to 1.9 eV at room temperature. The value extracted for the indirect gap at room temperature is in agreement with those previously reported in the literature, whose relatively large spread has been attributed to variations both in the material synthesis conditions and inherently imprecise fitting methods used [249].

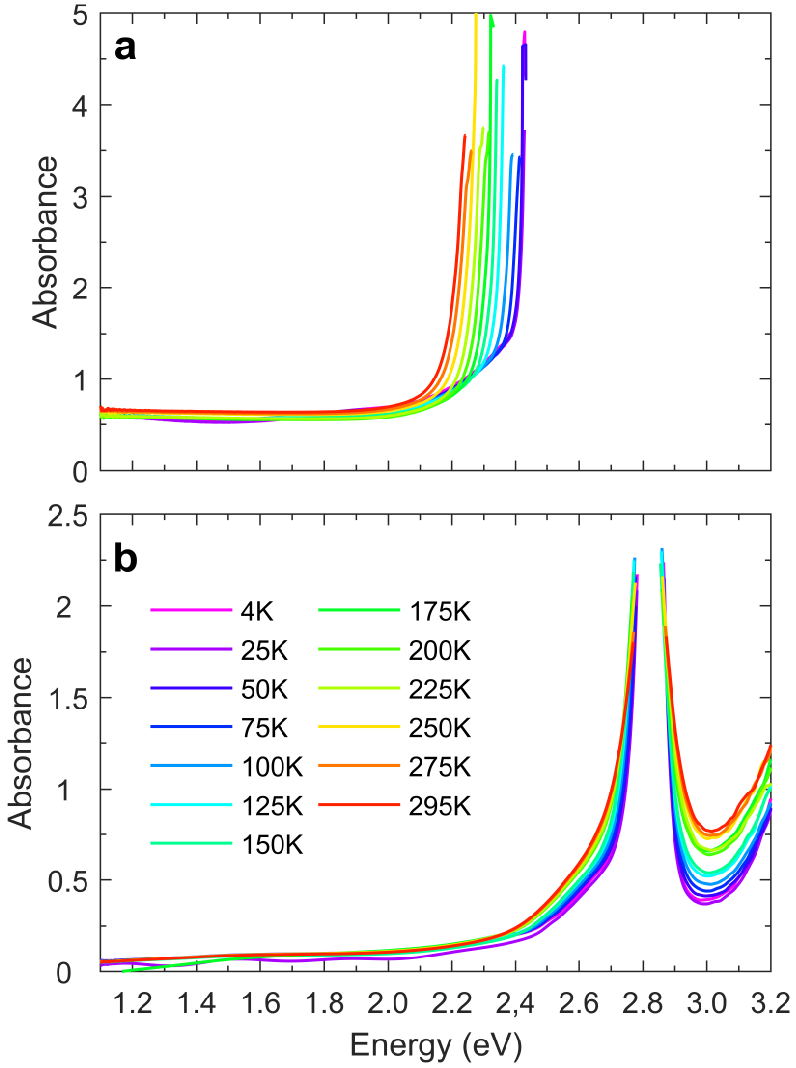

Figure 6.1: Temperature-dependent absorbance spectra of $Cs_2AgBiBr_6$. Absorbance spectra for **(a)** single crystal and **(b)** thin film $Cs_2AgBiBr_6$ are shown at roughly 25 K temperature intervals from 4 K (magenta) to 295K (red). The high-energy cut-offs to the curves occur at the limit of detector sensitivity to light transmitted through the sample, which occurs at lower energies for the single crystal due to its thickness. This limited sensitivity is also responsible for the gap in the curves for the thin films around 2.8 eV, which is attributed to strong excitonic absorption.

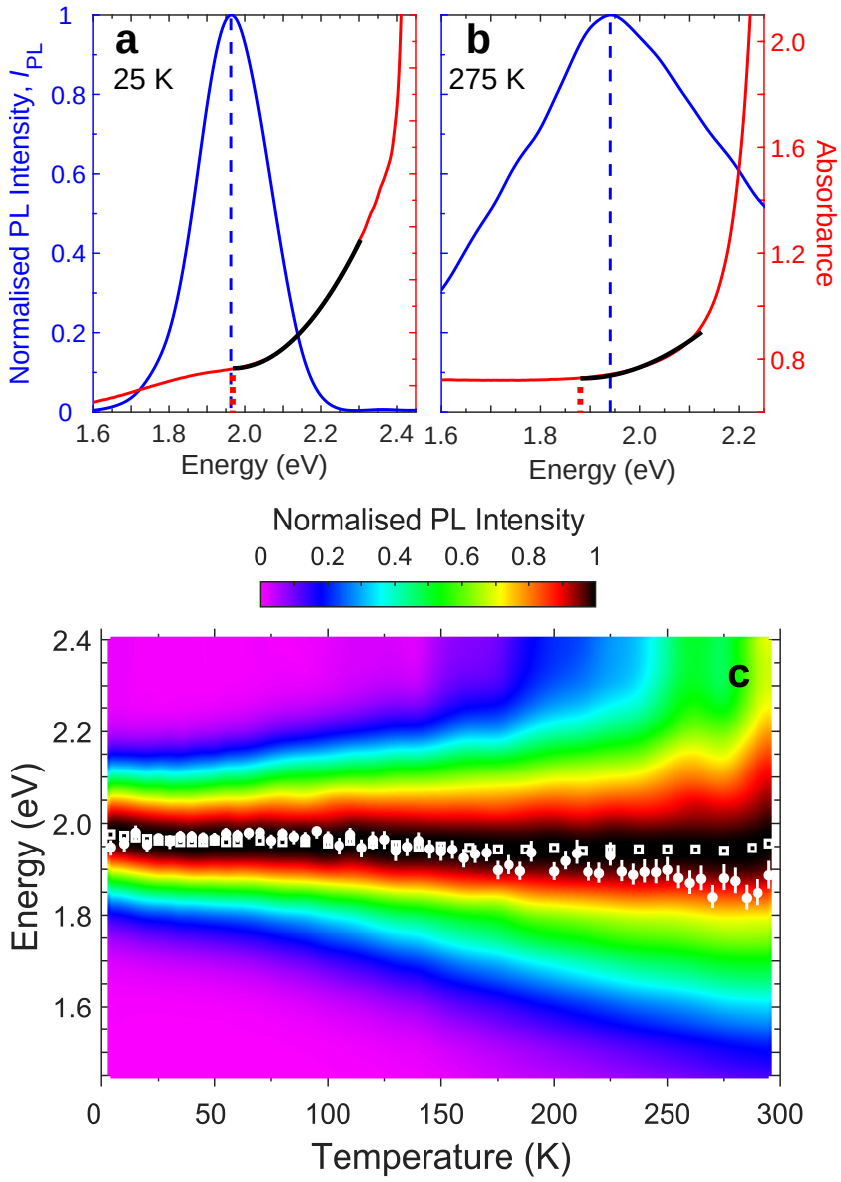

Figure 6.2: PL and absorbance measurements of single-crystal $Cs_2AgBiBr_6$. Steady-state PL (solid blue line) and absorption spectra (solid red line) at **(a)** 25 K and **(b)** 275 K are plotted as a function of photon energy E. Quadratic fits ($A\ (E - E_g^i)^2$) to the absorption onsets are plotted in black, with the minimum energy (E_g^i) indicated by dotted red lines. The dashed blue lines indicate the energy at the maximum PL intensity. These energies provide estimates of the indirect bandgap E_g^i, and are plotted as a function of temperature in **(c)** as white circles (absorption) and open squares (PL), overlaid on colour plots of the normalized PL spectra at temperatures between 4 and 295 K.

Due to being 3000 times thinner than the single crystals, the thin film absorbances in Fig. 6.1b have a much shallower baseline. Although it is not quite zero (perhaps due to scattering), the baseline is nonetheless remarkably low due to the vapour-deposition method used to prepare the thin film samples, which yields smooth, uniform films with relatively low scattering [55]. Like the single crystal spectra, those of the thin film also develop a sharp rise in absorbance which redshifts with increasing temperature. However, in this case the sharp rise occurs at least 300 meV above that of the single crystal, and is preceded by a more gradual rise at lower energies. Although for both samples the transmittance drops too much for the absorbance to be determined above the rise, in thin films the transmittance rises again at higher energies still, allowing a sharp decrease in the absorbance to be discerned at all temperatures, before a more gradual increase up to the limit of the detector sensitivity.

With the benefit of these data from an additional energy range, it is possible to interpret the absorbance spectra of $Cs_2AgBiBr_6$ in terms of an indirect gap, an excitonic absorption, and a direct gap (in ascending order of energy). Curves representing the functional form of the absorbance expected from these features are shown in Fig. 6.3a and b. The initial moderate onset may be represented by a quadratic function [248], as was used for the single crystal. The E_g^i values extracted from these fits are plotted in Fig. 6.3c and more clearly in Fig. 6.4c, lying in a similar energy range to the single crystal data, but exhibiting a blueshift with temperature rather than a redshift. The large error bars on the E_g^i values are a result of the uncertainty in the range over which the function was fitted. Meanwhile, the sharp rise and fall in the absorbance around 2.82 eV is interpreted as being the two sides of an excitonic absorption peak, whose top is missing due to the lack of sufficient transmittance data at the energies where the excitons are most absorbing. By phenomenologically fitting a Gaussian function to the two visible sides of this purported peak, it is possible to estimate the energy of the

exciton from the centre of the Gaussian, as plotted in Fig. 6.4b. Intriguingly, the trend in the excitonic energy with temperature reverses just above T_S, implying a connection with the structural phase transition. Finally, the highest-energy onset is fitted with a square-root function ($A \sim (E - E_g^d)^{1/2}$), a relationship which is characteristic of direct transitions [248] and has previously been used to estimate the room-temperature direct gap energy of single-crystal $Cs_2AgBiBr_6$ via the Tauc method, in which a straight line (with an expected gradient of two) is fitted to an absorption onset on a log plot. However, these resulted in estimates of 2.21 eV [21], 2.41 eV [249] and 2.77 eV [139], which is significantly lower than the 3.03 eV direct gap energy at 295 K obtained from the thin film data in Fig. 6.1b. A more rigorous extraction of the direct bandgap energy from the absorbance spectra would require the use of Elliott's theory [55, 250].

The temperature-dependent PL spectra of the single crystal and thin film samples are plotted in Fig. 6.2c and Fig. 6.3c respectively. In both cases, the PL spectra peak at around 1.95 eV, which is consistent with it being emission from radiative transitions across the indirect bandgap. Unsurprisingly, such indirect bandgap PL is weak (as has been observed before for this material [251]), so the side-shoulder features observed at higher temperatures may be artefacts from the measurement of very dim emission, or alternatively the result of the involvement of phonons. As shown in the figures, the PL peak energies correlate well with the values of E_g^i estimated from quadratic fits to the absorbance spectra.

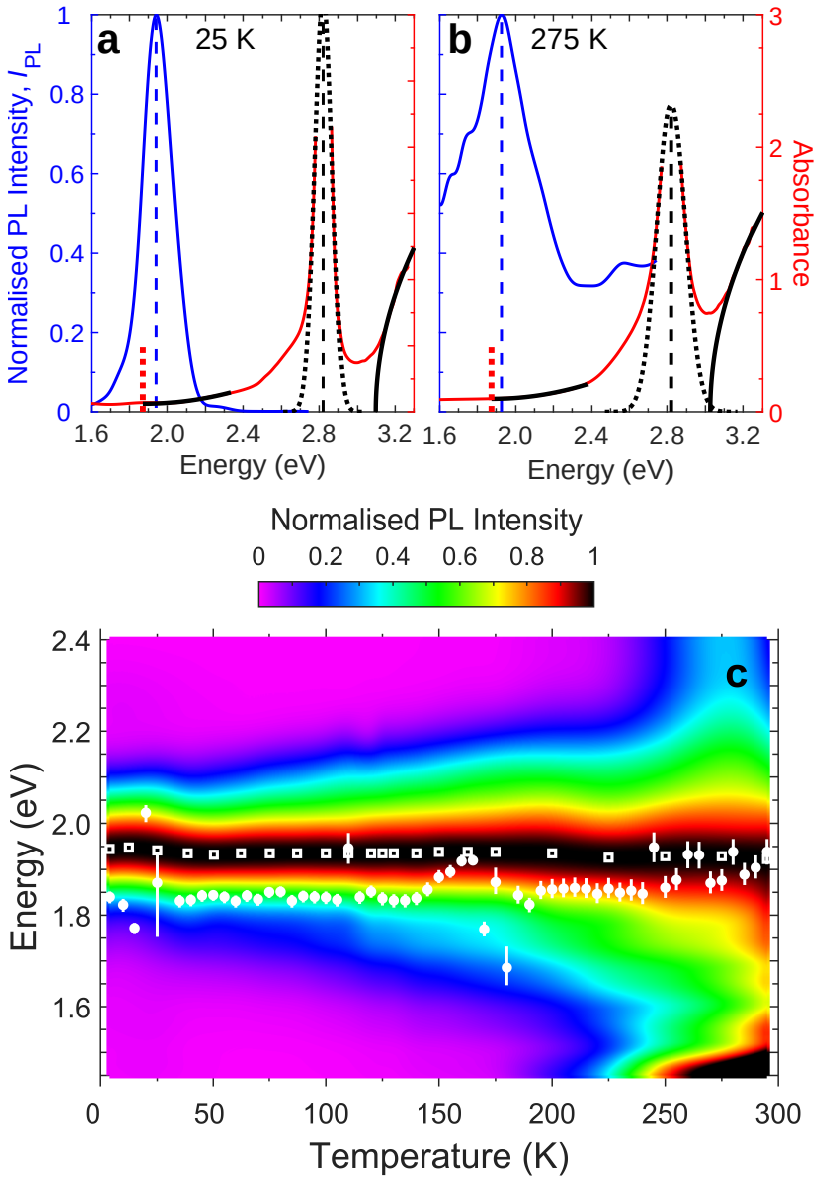

Figure 6.3: PL and absorbance measurements of thin film $Cs_2AgBiBr_6$. Steady-state PL (solid blue line) and absorption spectra (solid red line) at **(a)** 25 K and **(b)** 275 K as a function of photon energy E. As in Fig. 6.2, quadratic fits to the indirect bandgap absorption onset around 2 eV are shown as solid black lines. Additionally, Gaussian fits to the excitonic absorption peak around 2.8 eV is plotted as a dotted black line, with its central energy shown as a dashed black line. The solid black line at higher energies depicts a square-root fit ($A \sim (E - E_g^d)^{1/2}$) to the direct onset. The estimates of the indirect bandgap from the quadratic fits, E_g^i, are plotted as a function of temperature in **(c)** as white circles (absorption) and open squares (PL), overlaid on colour plots of the normalized PL spectra at temperatures between 4 and 295 K.

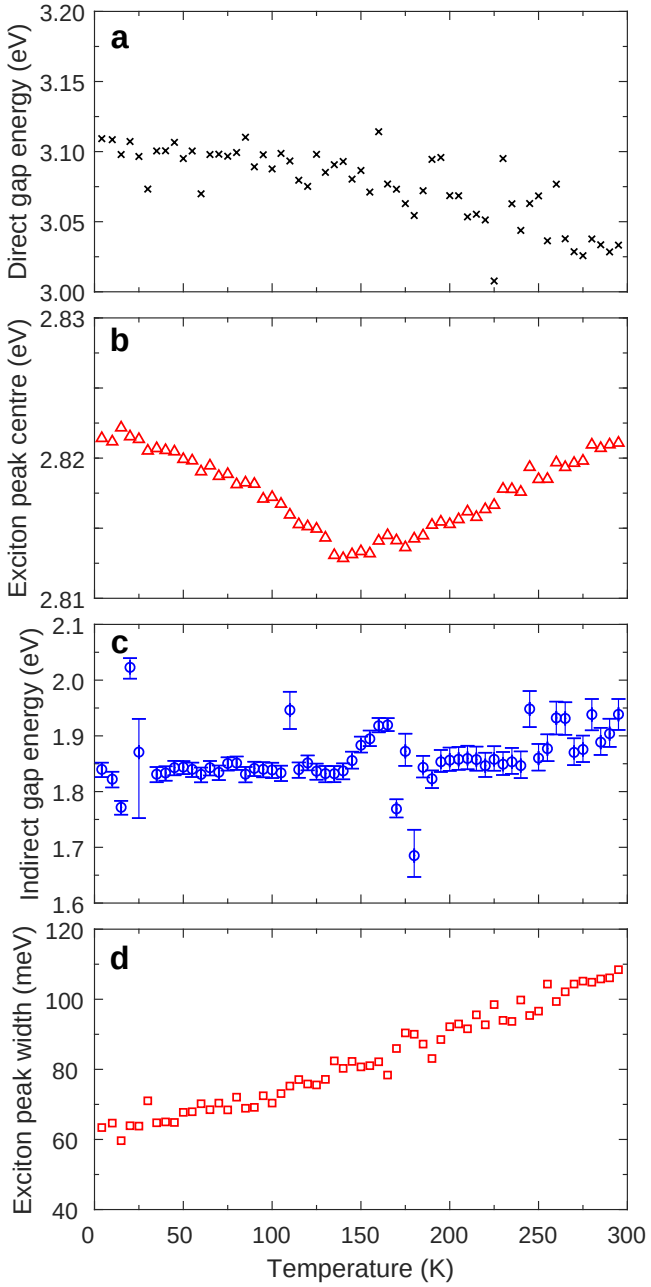

Figure 6.4: Temperature dependence of fitting parameters to absorbance of $Cs_2AgBiBr_6$ thin films. In Fig. 6.3, three fits are shown to features of the absorbance spectrum: a quadratic function is fitted to the indirect gap onset, a Gaussian function to the excitonic absorption peak, and a square root function to the direct gap onset. In **(a)** here, the temperature dependence of the direct gap energy from the square root fit is plotted as black crosses. The centre of the Gaussian fit representing the exciton energy, is shown in **(b)** by red triangles, while **(d)** shows the FWHM of the Gaussian fit with red squares. In **(c)**, the indirect bandgap energy derived from the quadratic fit is plotted as blue circles, with error bars showing the uncertainty due to the choice of the fitting range.

6.2.2 Temperature-dependence of PL transients

To characterise the temperature dependence of charge-carrier recombination mechanisms in $Cs_2AgBiBr_6$, the PL transients at the peak PL emission energy were measured using TCSPC, as shown in Fig. 6.5 for the single crystal sample and Fig. 6.6 for the thin film. The behaviour of the PL transients in both samples was very similar, which is suggestive of charge-carrier recombination in $Cs_2AgBiBr_6$ being dominated by intrinsic factors rather than ones which depend on the processing method. At temperatures up to the phase transition, $T_S \approx 122$ K [246], the transients all exhibit a very fast initial decay, followed by a much slower one, which speeds up with increasing temperature, as shown in Fig. 6.5a and Fig. 6.6a. The transients above T_S are presented in Fig. 6.5b and Fig. 6.6b: the PL decays appear smoothly curved, and speed up with temperature.

These trends can be understood in terms of two PL decay channels: a short one ('S'), present in the low-temperature tetragonal phase, and a longer one ('L'), present throughout. By modelling S as monoexponential, and L with a stretched exponential, it was possible to fit the PL transients faithfully across the entire temperature range, and to extract lifetimes for the PL decay components, as shown in Fig. 6.5c and Fig. 6.6c.

Since the distribution coefficients of the stretched exponentials tended to be very small, the usual expression for calculating the average lifetime of a stretched exponential function is not a very meaningful average (cf. Subsection 2.4.1 and Ref. [82]), so the characteristic lifetime τ_c was used instead. On warming, the lifetime of L remains much lower than that of S, while its overall intensity decreases. However, the decay of L becomes faster on warming, as is typical for MHPs [58]. The contribution of S to the fits in the tetragonal phase rapidly became ineffective as the tetragonal distortion was significantly reduced. At room temperature, the short PL lifetimes may appear at odds with the long carrier lifetimes for which $Cs_2AgBiBr_6$ has been lauded [21, 251]. However, these lifetimes had been derived from a very low-intensity tail, which has been ascribed

to recombination of charges in shallow trap states [247] and is in any case likely to be an independent PL decay channel from those considered here

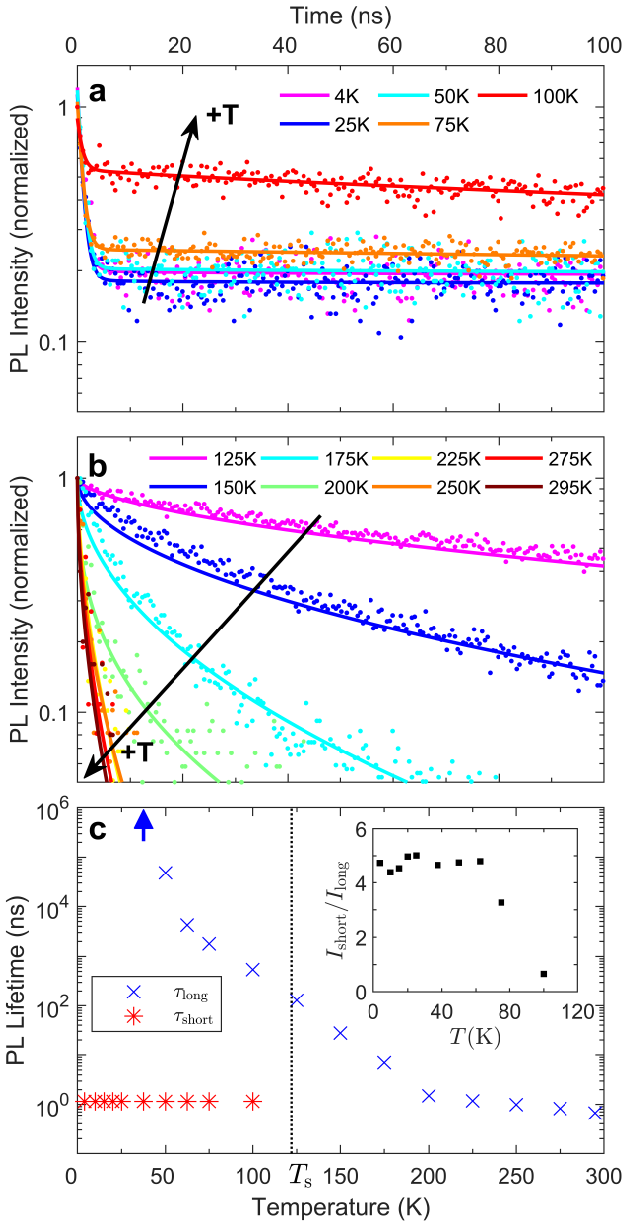

Figure 6.5: Time-dependent photoluminescence of single-crystal $Cs_2AgBiBr_6$. PL transients at temperatures between 4 and 100 K (tetragonal phase) are plotted as dots in **(a)**. Global fits of the sum of a stretched exponential (long) and a monoexponential (short) component, with the lifetime of the latter common between the temperatures, are shown as solid lines. PL transients at temperatures from 125 to 295 K (cubic phase) are shown as dots in **(b)**, with the lines now representing solely stretched exponential fits. The overall temperature trend of the shapes of the transients in both phases are indicated by black arrows. The lifetimes of the long (blue) and short (red) components are shown in **(c)**, on both sides of the phase transition temperature indicated by the dotted line labelled T_c. Below 50 K, the fitted long component lifetimes exceed the measurement capability of the system, as indicated by the blue arrow. The inset shows the temperature dependence of the ratio between the intensities of the short and long components.

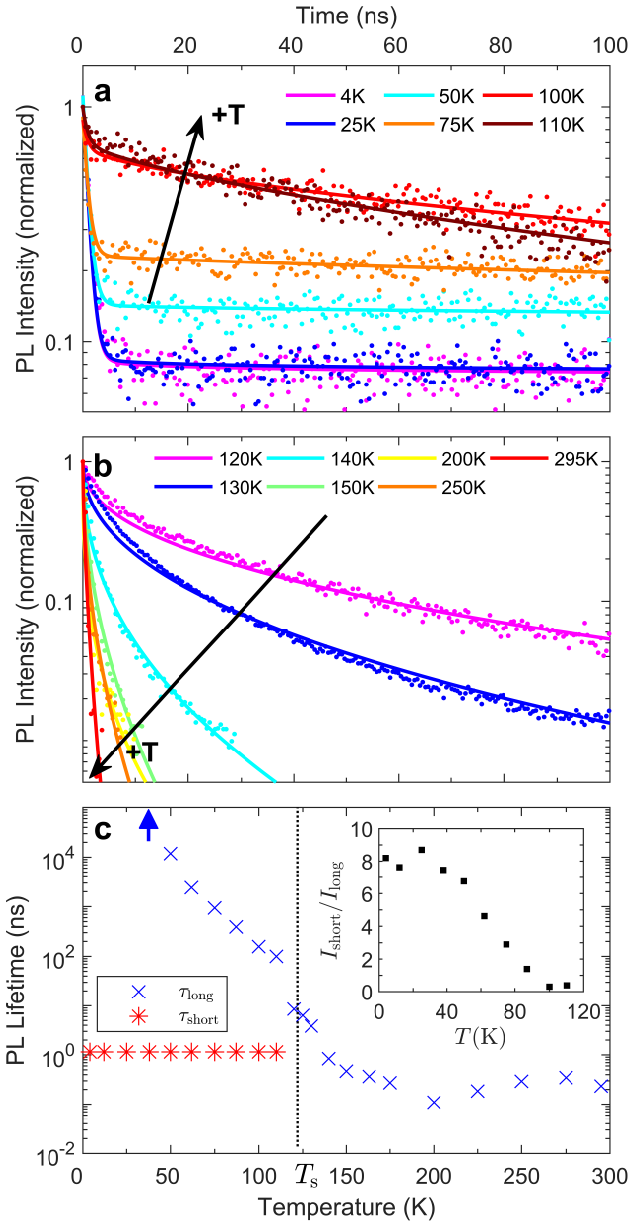

Figure 6.6: Time-dependent photoluminescence of thin film $Cs_2AgBiBr_6$. PL transients at temperatures between 4 and 110 K (tetragonal phase) are plotted as dots in **(a)**. Global fits of the sum of a stretched exponential (long) and a monoexponential (short) component, with the lifetime of the latter common between the temperatures, are shown as solid lines. PL transients at temperatures from 120 to 295 K (cubic phase) are shown as dots in **(b)**, with the lines now representing solely stretched exponential fits. The overall temperature trend of the shapes of the transients in both phases are indicated by black arrows. The lifetimes of the long (blue) and short (red) components are shown in c), on both sides of the phase transition temperature indicated by the dotted line labelled T_c. Below 50 K, the fitted long component lifetimes exceed the measurement capability of the system, as indicated by the blue arrow. The inset shows the temperature dependence of the ratio between the intensities of the short and long components.

6.3 Discussion

This study has characterised the indirect bandgap transition in $Cs_2AgBiBr_6$, and taken advantage of the extended absorbance spectrum available from thin-film samples to observe the direct exciton and direct bandgap as well. The direct gap energy obtained from fitting a square root function to the thin-film absorbance spectrum at room temperature is however hundreds of meV higher than estimates from other studies obtained from Tauc plots of single-crystal $Cs_2AgBiBr_6$ [21, 139, 249]. This discrepancy may be rationalised by noting that above the indirect bandgap onset in the single crystal absorption data presented here, the absorbance spectrum rises steeply. Whereas previous studies have attributed this rise to the direct bandgap, using a high-quality thin film sample allows the meaningful absorbance spectrum to be extended to higher energies, at which a drop in the absorbance and subsequent further onset are visible. If the thin film absorbance spectra are interpreted as containing a distinct excitonic peak, this suggests that it is the low-energy side of this which has previously been misattributed to the direct bandgap onset. The absence of this excitonic feature from previous absorbance spectra from single crystals [21, 139, 249] and solution-processed thin films [141, 251] is unsurprising given that the dip in transmitivitty above the excitonic energy (which is necessary to observe the exciton peak), is not resolvable against the overall low transmitivitty at high energies for optically thick or disordered samples: once there are some absorbing states, any higher-energy photons are likely to eventually be absorbed. Thus, it may be necessary to reconsider the consensus on the optical transitions in $Cs_2AgBiBr_6$. Notably, this observation of the exciton peak and true direct onset allows the exciton binding energy to be estimated to be 300 meV, which is too large for thermal dissociation of excitons to be possible at room temperature. However, given that the PL emission is dominated by the indirect gap, to where the majority of carriers likely relax after photoexcitation, it may be

that the indirect exciton needs to be considered instead. Ultrafast PL measurements to observe the relaxation of charge-carriers from the direct gap and more rigorous modelling of the absorption spectrum in terms of the Elliott model [55, 250] would likely clarify matters, as would more sensitive measurements of the absorbance at higher energies, in order to better characterise the postulated direct gap onset.

This study has also elucidated the relationship between the structural and optical properties of $Cs_2AgBiBr_6$. In addition to an intriguing discontinuity in the temperature dependence of the excitonic energy at the tetragonal-to-cubic phase transition, the short 'S' PL decay channel has been identified as only occurring in the tetragonal phase. One possible explanation is that S is associated with defects at the boundaries between twins in the tetragonal phase, which spontaneously form on cooling through the phase transition in crystalline materials (including MHPs [252]) as a response to applied deformation or thermal stress [253]. Twins are regions of a crystal in which the unit cells have different orientations: for MHPs, this corresponds to the orientations of the octahedra. By repeating the PL measurements on a single crystal cooled under biaxial compressive strain to promote the formation of a single tetragonal domain, this hypothesis could be tested by observing whether the S decay channel was still present.

7
Conclusions and Outlook

The work presented in this thesis has primarily been concerned with the influence of the MHP lattice on charge-carrier motion and recombination therein. An underlying theme has been that MHPs may be viewed through a classic inorganic semiconductor picture, even if they contain organic components. Emission-line broadening in hybrid MHPs was understood in terms of electron-phonon coupling, while a power-law PL time decay and additional PL emission peak were explained by the presence of a band tail of localised states in an otherwise delocalised bandstructure picture. Discontinuous changes in the optical properties of $Cs_2AgBiBr_6$ were correlated with a structural phase transition of the lattice. While these interpretations may seem 'obvious' given the parallel phenomena which have previously been reported in the inorganic semiconductor literature, the origins of MHP solar cells from a DSSC architecture, together with their association with organic photovoltaics due to the organic MA moiety in the archetypal MHP $MAPbI_3$, meant that they were not 'obvious' until after evidence had been gathered for them. Photoluminescence spectroscopy was shown to be the ideal tool for interrogating electronic processes in these materials in order to gather this evidence, since it permitted a large parameter space of time, temperature and intensity to be accessed in order to build up a

detailed picture of what factors influence charge-carrier recombination in MHPs.

Chapter 4 involved an in-depth analysis of charge-carrier–phonon interactions in hybrid lead-halide perovskites, considering the four currently most implemented organic and halide components in hybrid perovskite photovoltaics, which are $FAPbI_3$, $FAPbBr_3$, $MAPbI_3$ and $MAPbBr_3$. An analysis of the temperature-dependent emission linewidth of $FAPbI_3$ and $FAPbBr_3$ allowed it to be established that the Fröhlich interaction between charge-carriers and LO phonons provides the dominant contribution to the predominantly homogeneous linewidth broadening in these hybrid perovskites at room temperature. These findings were successfully corroborated by DFT and many-body perturbation theory calculations, which underline the suitability of an electronic bandstructure picture for describing charge-carriers in perovskites. Furthermore, experimentally measured energies of LO phonon modes responsible for Fröhlich interactions in these materials were obtained, and it was shown that Fröhlich interactions are higher for bromide perovskites than iodide perovskites, providing a link between composition and electron-phonon scattering that fundamentally limits charge-carrier motion. These results lay the groundwork for more quantitative models of charge-carrier mobility values and cooling dynamics that underpin photovoltaic device operation.

The overall analysis presented in Chapter 5 reveals the band-tail PL emission from $FAPbI_3$ to be consistent with typical behaviour for an inorganic semiconductor, described by a band-structure picture with a relatively modest degree of energetic disorder as reflected by spatial variation of the bandgap energy. The maximum value of the anomalous relative Stokes shift observed here for $FAPbI_3$ at low charge-carrier densities ($\approx$40 meV) is similar to the values observed in other inorganic semiconductors such as AlInGaN ($\approx$45 meV) [224], GaInNAs ($\approx$55 meV) [254]and CdSe/ZnSe ($\approx$20 meV) [255], while band-tail emission has also been observed in CIGS and CZTS [256]. Despite often being misidentified until represented on a log-log plot [89], power-law luminescence decays have

also been identified in a range of systems, including semiconductor quantum dots [257], dye-sensitized nanoparticle films [92] and semiconductors such as hydrogenated amorphous Si [90], p-type GaAs [258] and GaP [259]. The observations and numerical analysis here therefore highlight the general applicability of the classic inorganic semiconductor picture to hybrid lead halide perovskites, despite their partly organic ingredients.

Chapter 5 established the energetic distribution of trap states in $FAPbI_3$, a high quality hybrid perovskite that is the active ingredient to some of the highest performing perovskite photovoltaic cells. Its measurements of low-temperature PL over six decades of time after excitation allowed the observation of a power-law time decay in the PL intensity, and an additional emission peak which exhibits an anomalous temperature dependence. It is demonstrated qualitatively and quantitatively that both effects are the direct consequence of charge-carrier recombination in a band-tail of states. Through numerical modelling, it was possible to identify the characteristic energy scale of the band tail, which is proposed to arise from local variations in electrostatic potential caused by different orientations of the polar FA cations. These discoveries provide valuable insight into the influence of trap states on charge-carrier recombination in this highly promising photovoltaic material.

In Chapter 6, the optical properties of single crystals and thin films of $Cs_2AgBiBr_6$ were compared, with the extended available absorbance spectra from the evaporated thin films permitting the novel identification of a distinct excitonic absorption which may necessitate the re-interpretation of previously reported absorbance spectra from single crystals and solution-processed thin films. Further investigation could concentrate on more rigorously quantitatively modelling the absorbance spectra and extending their measurement to higher energies in order to better characterise the direct bandgap. Since the indirect bandgap is that which dominates emission, observations of how charge-carriers funnel into this transition from the direct gap could also be fruitful. Even if these double perovskites do not succeed in solar cells, a better understanding of their

electronic transitions will be required to optimise them for an alternative role as X-ray and gamma radiation detectors [249]. Meanwhile, the identification of a PL decay channel which is only present in the low temperature tetragonal phase gives cause for hope that structural alterations to double perovskites might be able to improve their optoelectronic properties. Attempting this at low temperature by trying to eliminate the aforementioned decay channel by applying strain to a single crystal across the phase transition would be a promising proof of principle.

References

[1] Lanzani, G. *The photophysics behind photovoltaics and photonics*. Wiley-VCH, 2012.

[2] Service, R. F. 'Is it time to shoot for the sun?' *Science*, 2005, **309**, 548–551.

[3] OECD. *World Energy Balances 2017*. OECD, 2017.

[4] Becquerel, A.-E. 'Recherches sur les effets de la radiation chimique de la lumiere solaire au moyen des courants electriques'. *Comptes Rendus Acad. Sci.* 1839, **9**, 145–149.

[5] Philipps, S. *Fraunhofer ISE: Photovoltaics Report*. Tech. rep. Freiburg, 2018. `https://www.ise.fraunhofer.de/en/publications/studies/photovoltaics-report.html`.

[6] Chen, C. J. *Physics of Solar Energy*. John Wiley & Sons, 2011.

[7] Correa-Baena, J.-P., Saliba, M., Buonassisi, T., Grätzel, M., Abate, A., Tress, W. and Hagfeldt, A. 'Promises and challenges of perovskite solar cells'. *Science*, 2017, **744**, 739–744.

[8] Kymakis, E., Alexandrou, I. and Amaratunga, G. A. J. 'High open-circuit voltage photovoltaic devices from carbon-nanotube-polymer composites'. *J. Appl. Phys.* 2003, **93**, 1764–1768.

[9] Hodes, G. 'Perovskite-based solar cells'. *Science*, 2013, **342**, 317–319.

[10] Egger, D. A., Bera, A., Cahen, D., Hodes, G., Kirchartz, T., Kronik, L., Lovrincic, R., Rappe, A. M., Reichman, D. R. and Yaffe, O. 'What remains unexplained about the properties of halide perovskites?' *Adv. Mater.* 2018, **30**, 1800691.

[11] NREL. *Research Cell Efficiency Records, National Center for Photovoltaics*. 2018. `https://www.nrel.gov/pv/assets/images/efficiency-chart-20180716.jpg` (visited on 09/08/2018).

[12] Miyasaka, T. 'Lead halide perovskites in thin film photovoltaics: backgrounds and perspectives'. *Bull. Chem. Soc. Jpn*, 2018, **91**, 1058–1068.

[13] Herz, L. M. 'Charge-carrier dynamics in organic-inorganic metal halide perovskites'. *Annu. Rev. Phys. Chem.* 2016, **67**, 65–89.

[14] Kim, H.-S., Im, S. H. and Park, N.-G. 'Organolead halide perovskite: new horizons in solar cell research'. *J. Phys. Chem. C*, 2014, **118**, 5615–5625.

[15] Malinkiewicz, O., Yella, A., Lee, Y. H., Espallargas, G. M., Graetzel, M., Nazeeruddin, M. K. and Bolink, H. J. 'Perovskite solar cells employing organic charge-transport layers'. *Nature Photon.* 2013, **8**, 128–132.

[16] Berry, J., Buonassisi, T., Egger, D. A., Hodes, G., Kronik, L., Loo, Y.-L., Lubomirsky, I., Marder, S. R., Mastai, Y., Miller, J. S., Mitzi, D. B., Paz, Y., Rappe, A. M., Riess, I., Rybtchinski, B., Stafsudd, O., Stevanovic, V., Toney, M. F., Zitoun, D., Kahn, A., Ginley, D. and Cahen, D. 'Hybrid Organic-Inorganic Perovskites (HOIPs): opportunities and challenges'. *Adv. Funct. Mater.* 2015, **27**, 5102–5112.

[17] Yu, P. Y. and Cardona, M. *Fundamentals of Semiconductors*. Springer-Verlag, 2010.

[18] Rehman, W., Milot, R. L., Eperon, G. E., Wehrenfennig, C., Boland, J. L., Snaith, H. J., Johnston, M. B. and Herz, L. M. 'Charge-carrier dynamics and mobilities in formamidinium lead mixed-halide perovskites'. *Adv. Mater.* 2015, **27**, 7938–7944.

[19] Johnston, M. B. and Herz, L. M. 'Hybrid Perovskites for photovoltaics: charge-carrier recombination, diffusion, and radiative efficiencies'. *Acc. Chem. Res.* 2016, **49**, 146–154.

[20] Ball, J. M. and Petrozza, A. 'Defects in perovskite-halides and their effects in solar cells'. *Nat. Energy*, 2016, **1**, 16149.

[21] Slavney, A. H., Hu, T., Lindenberg, A. M. and Karunadasa, H. I. 'A bismuth-halide double perovskite with long carrier recombination lifetime for photovoltaic applications'. *J. Am. Chem. Soc.* 2016, **138**, 2138–2141.

[22] Savory, C. N., Walsh, A. and Scanlon, D. O. 'Can Pb-free halide double perovskites support high-efficiency solar cells?' *ACS Energy Lett.* 2016, **1**, 949–955.

[23] Rose, G., Humboldt, A. von and Ehrenberg, C. G. *Mineralogischgeognostische Reise nach dem Ural, dem Altai and dem Kaspische Meere, Zweiter Band*. Verlag der Sanderschen Buchandlung, 1842.

[24] Wagner, P., Wackers, G., Cardinaletti, I., Manca, J. and Vanacken, J. 'From colossal magnetoresistance to solar cells: an overview on 66 years of research into perovskites'. *Phys. Status Solidi A*, 2017, **214**, 1700394.

[25] Davies, C. L., Borchert, J., Milot, R. L., Kraus, H., Johnston, M. B. and Herz, L. M. 'Impact of the organic cation on the optoelectronic properties of formamidinium lead triiodide'. *J. Phys. Chem. Lett.* 2018, **9**, 4502–4511.

[26] Goldschmidt, V. M. 'Die Gesetze der Krystallochemie'. *Die Naturwissenschaften*, 1926, **14**, 477–485.

[27] Leijtens, T., Eperon, G. E., Noel, N. K., Habisreutinger, S. N., Petrozza, A. and Snaith, H. J. 'Stability of metal halide perovskite solar cells'. *Adv. Energy Mater.* 2015, **5**, 1500963.

[28] Wang, B., Xiao, X. and Chen, T. 'Perovskite photovoltaics: a high-efficiency newcomer to the solar cell family.' *Nanoscale*, 2014, **6**, 12287–12297.

[29] Brenner, T. M., Egger, D. A., Kronik, L., Hodes, G. and Cahen, D. 'Hybrid organic-inorganic perovskites: low-cost semiconductors with intriguing charge-transport properties'. *Nat. Rev. Mater.* 2016, **1**, 15007.

[30] Poglitsch, A. and Weber, D. 'Dynamic disorder in methylammoniumtrihalogenoplumbates (II) observed by millimeter-wave spectroscopy'. *J. Chem. Phys.* 1987, **87**, 6373–6378.

[31] Weber, D. '$CH_3NH_3PbX_3$, ein Pb (II)-System mit kubischer Perowskitstruktur'. *Z. Naturforsch B*, 1978, **33b**, 1443–1445.

[32] Mitzi, D. B., Prikas, M. T. and Chondroudis, K. 'Thin film deposition of organic-inorganic hybrid materials using a single source thermal ablation technique'. *Chem. Mater.* 1999, **11**, 542–544.

[33] Mitzi, D. B., Feild, C. A., Harrison, W. T. A. and Guloy, A. M. 'Conducting tin halides with a layered organic-based perovskite structure'. *Nature*, 1994, **369**, 467–9.

[34] Mitzi, D. B. and Feild, C. A. 'Transport, optical, and magnetic properties of the conducting halide perovskite $CH_3NH_3SnI_3$'. *J. Solid State Chem.* 1995, **114**, 159–163.

[35] Mitzi, D. B. 'Solution-processed inorganic semiconductors'. *J. Mater. Chem.* 2004, 2355–2365.

[36] Kojima, A., Teshima, K., Shirai, Y. and Miyasaka, T. 'Organometal halide perovskites as visible-light sensitizers for photovoltaic cells'. *J. Am. Chem. Soc.* 2009, **131**, 6050–6051.

[37] Gao, P., Grätzel, M. and Nazeeruddin, M. K. 'Organohalide lead perovskites for photovoltaic applications'. *Energy Environ. Sci.* 2014, **7**, 2448–2463.

[38] Lee, M. M., Teuscher, J., Miyasaka, T., Murakami, T. N. and Snaith, H. J. 'Efficient hybrid solar cells based on meso-superstructured organometal halide perovskites.' *Science*, 2012, **338**, 643–647.

[39] Kim, H.-S., Lee, C.-R., Im, J.-H., Lee, K.-B., Moehl, T., Marchioro, A., Moon, S.-J., Humphry-Baker, R., Yum, J.-H., Moser, J. E., Grätzel, M. and Park, N.-G. 'Lead iodide perovskite sensitized all-solid-state submicron thin film mesoscopic solar cell with efficiency exceeding 9%.' *Sci. Rep.* 2012, **2**, 591.

[40] Etgar, L., Gao, P. and Xue, Z. 'Mesoscopic $CH_3NH_3PbI_3/TiO_2$ heterojunction solar cells'. *J. Am. Chem. Soc.* 2012, **134**, 8–11.

[41] Liang, P. W., Liao, C. Y., Chueh, C. C., Zuo, F., Williams, S. T., Xin, X. K., Lin, J. and Jen, A. K. Y. 'Additive enhanced crystallization of solution-processed perovskite for highly efficient planar-heterojunction solar cells'. *Adv. Mater.* 2014, **26**, 3748–3754.

[42] Snaith, H. J. 'Perovskites: the emergence of a new era for low-cost, high-efficiency solar cells'. *J. Phys. Chem. Lett.* 2013, **4**, 3623–3630.

[43] Grätzel, M. 'The rise of highly efficient and stable perovskite solar cells'. *Acc. Chem. Res.* 2017, **50**, 487–491.

[44] Wang, Z., Lin, Q., Chmiel, F. P., Sakai, N., Herz, L. M. and Snaith, H. J. 'Efficient ambient-air-stable solar cells with 2D-3D heterostructured butylammonium-caesium-formamidinium lead halide perovskites'. *Nat. Energy*, 2017, **2**, 1–10.

[45] Hodes, G. and Cahen, D. 'Photovoltaics: Perovskite cells roll forward'. *Nature Photon.* 2014, **8**, 87–88.

[46] Saliba, M., Matsui, T., Domanski, K., Seo, J.-Y., Ummadisingu, A., Zakeeruddin, S. M., Correa-Baena, J.-P., Tress, W. R., Abate, A., Hagfeldt, A. and Gratzel, M. 'Incorporation of rubidium cations into perovskite solar cells improves photovoltaic performance'. *Science*, 2016, **354**, 206–209.

[47] Stroyuk, O. 'Lead-free hybrid perovskites for photovoltaics'. *Beilstein J. Nanotechnol.* 2018, **9**, 2209–2235.

[48] Shockley, W. and Queisser, H. J. 'Detailed balance limit of efficiency of p-n junction solar cells'. *J. Appl. Phys.* 1961, **32**, 510–519.

[49] Snaith, H. J. 'Present status and future prospects of perovskite photovoltaics'. *Nat. Mater.* 2018, **17**, 372–376.

[50] Liu, M., Johnston, M. B. and Snaith, H. J. 'Efficient planar heterojunction perovskite solar cells by vapour deposition'. *Nature*, 2013, **501**, 395–398.

[51] Yang, W. S., Noh, J. H., Jeon, N. J., Kim, Y. C., Ryu, S., Seo, J. and Seok, S. I. 'High-performance photovoltaic perovskite layers fabricated through intramolecular exchange'. *Science*, 2015, **348**, 1234–1237.

[52] Green, M. A., Jiang, Y., Mahboubi Soufiani, A. and Ho-Baillie, A. W.-Y. 'Optical properties of photovoltaic organic-inorganic lead halide perovskites'. EN. *J. Phys. Chem. Lett.* 2015, **6**, 4774–4785.

[53] Meillaud, F., Shah, A., Droz, C., Vallat-Sauvain, E. and Miazza, C. 'Efficiency limits for single-junction and tandem solar cells'. *Sol. Energ. Mat. Sol. Cells*, 2006, **90**, 2952–2959.

[54] Scharber, M. C. and Sariciftci, N. S. 'Efficiency of bulk-heterojunction organic solar cells'. *Prog. Polym. Sci.* 2013, **38**, 1929–1940.

[55] Davies, C., Filip, M., Patel, J., Crothers, T., Verdi, C., Wright, A., Milot, R., Giustino, F., Johnston, M. and Herz, L. 'Bimolecular recombination in methylammonium lead triiodide perovskite is an inverse absorption process'. *Nat. Commun.* 2018, **9**, 293.

[56] Tvingstedt, K., Vandewal, K., Gadisa, A. and Zhang, F. 'Electroluminescence from charge transfer states in polymer solar cells'. *J. Am. Chem. Soc.* 2009, **10**, 11819–11824.

[57] Stranks, S. D., Eperon, G. E., Grancini, G., Menelaou, C., Alcocer, M. J. P., Leijtens, T., Herz, L. M., Petrozza, A. and Snaith, H. J. 'Electron-hole diffusion lengths exceeding 1 micrometer in an organometal trihalide perovskite absorber'. *Science*, 2013, **342**, 341–344.

[58] Milot, R. L., Eperon, G. E., Snaith, H. J., Johnston, M. B. and Herz, L. M. 'Temperature-dependent charge-carrier dynamics in $CH_3NH_3PbI_3$ perovskite thin films'. *Adv. Funct. Mater.* 2015, **25**, 6218–6227.

[59] Wehrenfennig, C., Liu, M., Snaith, H. J., Johnston, M. B. and Herz, L. M. 'Homogeneous emission line broadening in the organo lead halide perovskite $CH_3NH_3PbI_{3-x}Cl_x$'. *J. Phys. Chem. Lett.* 2014, **5**, 1300–1306.

[60] Eames, C., Frost, J. M., Barnes, P. R., O'Regan, B. C., Walsh, A. and Islam, M. S. 'Ionic transport in hybrid lead iodide perovskite solar cells'. *Nat. Commun.* 2015, **6**, 2–9. arXiv: `1409.6478`.

[61] Wehrenfennig, C. 'Ultrafast spectroscopy of charge separation , transport and recombination processes in functional materials for thin-film photovoltaics'. PhD thesis. University of Oxford, 2014.

[62] Wehrenfennig, C., Eperon, G. E., Johnston, M. B., Snaith, H. J. and Herz, L. M. 'High charge carrier mobilities and lifetimes in organolead trihalide perovskites'. *Adv. Mater.* 2014, **26**, 1584–1589.

[63] Stoumpos, C., Malliakas, C. and Kanatzidis, M. 'Semiconducting tin and lead iodide perovskites with organic cations: phase transitions, high mobilities, and near-infrared photoluminescent properties'. *Inorg. Chem.* 2013, **52**, 9019–9038.

[64] Brenner, T. M., Egger, D. A., Rappe, A. M., Kronik, L., Hodes, G. and Cahen, D. 'Are mobilities in hybrid organic-inorganic halide perovskites actually "high"?' *J. Phys. Chem. Lett.* 2015, **6**, 4754–4757.

[65] Umebayashi, T., Asai, K., Kondo, T. and Nakao, A. 'Electronic structures of lead iodide based low-dimensional crystals'. *Phys. Rev. B*, 2003, **67**, 155405.

[66] Miyata, A., Mitioglu, A., Plochocka, P., Portugall, O., Wang, J. T.-W., Stranks, S. D., Snaith, H. J. and Nicholas, R. J. 'Direct measurement of the exciton binding energy and effective masses for charge carriers in organic-inorganic tri-halide perovskites'. *Nat. Phys.* 2015, **11**, 582–587.

[67] Bi, Y., Hutter, E. M., Fang, Y., Dong, Q., Huang, J. and Savenije, T. J. 'Charge carrier lifetimes exceeding 15 microseconds in methylammonium lead iodide single crystals'. *J. Phys. Chem. Lett.* 2016, **7**, 923–928.

[68] Stranks, S. D., Burlakov, V. M., Leijtens, T., Ball, J. M., Goriely, A. and Snaith, H. J. 'Recombination kinetics in organic-inorganic perovskites: excitons, free charge, and subgap states'. *Phys. Rev. Appl.* 2014, **2**, 034007.

[69] Milot, R. L., Eperon, G. E., Green, T., Snaith, H. J., Johnston, M. B. and Herz, L. M. 'Radiative monomolecular recombination boosts amplified spontaneous emission in $HC(NH_2)_2SnI_3$ perovskite films'. *J. Phys. Chem. Lett.* 2016, **7**, 4178–4184.

[70] Richter, J. M., Abdi-Jalebi, M., Sadhanala, A., Tabachnyk, M., Rivett, J. P., Pazos-Outón, L. M., Gödel, K. C., Price, M., Deschler, F. and Friend, R. H. 'Enhancing photoluminescence yields in lead halide perovskites by photon recycling and light out-coupling'. *Nat. Commun.* 2016, **7**, 506–514.

[71] Wright, A. D., Milot, R. L., Eperon, G. E., Snaith, H. J., Johnston, M. B. and Herz, L. M. 'Band-tail recombination in hybrid lead iodide perovskite'. *Adv. Funct. Mater.* 2017, **27**, 1700860.

[72] Wright, A. D., Verdi, C., Milot, R. L., Eperon, G. E., Pérez-Osorio, M. A., Snaith, H. J., Giustino, F., Johnston, M. B. and Herz, L. M. 'Electron–phonon coupling in hybrid lead halide perovskites'. *Nat. Commun.* 2016, **7**, 11755.

[73] Fang, H.-H., Raissa, R., Abdu-Aguye, M., Adjokatse, S., Blake, G. R., Even, J. and Loi, M. A. 'Photophysics of organic-inorganic hybrid lead iodide perovskite single crystals'. *Adv. Funct. Mater.* 2015, **25**, 2378–2385.

[74] Deschler, F. and Price, M. 'High photoluminescence efficiency and optically pumped lasing in solution-processed mixed halide perovskite semiconductors'. *J. Phys. Chem. Lett.* 2014, **5**, 1421–1426.

[75] Noel, N. K., Abate, A., Stranks, S. D., Parrott, E., Burlakov, V., Goriely, A. and Snaith, H. J. 'Enhanced photoluminescence and solar cell performance via Lewis base passivation of organic-inorganic lead halide perovskites'. *ACS Nano*, 2014, **8**, 9815–9821.

[76] Xing, G., Mathews, N., Sun, S., Lim, S. S., Lam, Y. M., Grätzel, M., Mhaisalkar, S. and Sum, T. C. 'Long-range balanced electron- and hole-transport lengths in organic-inorganic $CH_3NH_3PbI_3$'. *Science*, 2013, **342**, 344–7.

[77] Shi, D., Adinolfi, V., Comin, R., Yuan, M., Alarousu, E., Buin, A., Chen, Y., Hoogland, S., Rothenberger, A., Katsiev, K., Losovyj, Y., Zhang, X., Dowben, P. A., Mohammed, O. F., Sargent, E. H. and Bakr, O. M. 'Low trap-state density and long carrier diffusion in organolead trihalide perovskite single crystals.' *Science*, 2015, **347**, 519–522.

[78] Wei, L., Peng, J., Weiying, W., Defeng, M., Guipeng, L., Zhanguo, W., Jiaming, W., Fujun, X. and Bo, S. 'Anomalous temperature-dependent photoluminescence peak energy in InAlN alloys'. *J. Semicond.* 2014, **35**, 093001.

[79] DeQuilettes, D. W., Vorpahl, S. M., Stranks, S. D., Nagaoka, H., Eperon, G. E., Ziffer, M. E., Snaith, H. J. and Ginger, D. S. 'Impact of microstructure on local carrier lifetime in perovskite solar cells'. *Science*, 2015, **348**, 683–686.

[80] Eperon, G. E., Stranks, S. D., Menelaou, C., Johnston, M. B., Herz, L. M. and Snaith, H. J. 'Formamidinium lead trihalide: a broadly tunable perovskite for efficient planar heterojunction solar cells'. *Energy Environ. Sci.* 2014, **7**, 982–988.

[81] Lindsey, C. P. and Patterson, G. D. 'Detailed comparison of the Williams–Watts and Cole–Davidson functions'. *J. Chem. Phys.* 1980, **73**, 3348–3357.

[82] Johnston, D. C. 'Stretched exponential relaxation arising from a continuous sum of exponential decays'. *Phys. Rev. B*, 2006, **74**, 184430.

[83] Li, X., Bi, D., Yi, C., Decoppet, J.-D., Luo, J., Zakeeruddin, S. M., Hagfeldt, A. and Gratzel, M. 'A vacuum flash-assisted solution process for high-efficiency large-area perovskite solar cells'. *Science*, 2016, **353**, 58–62.

[84] Mülken, O., Blumen, A., Amthor, T., Giese, C., Reetz-Lamour, M. and Weidemüller, M. 'Survival probabilities in coherent exciton transfer with trapping'. *Phys. Rev. Lett.* 2007, **99**, 090601.

[85] Huntley, D. J. 'An explanation of the power-law decay of luminescence'. *J. Phys.: Condens. Matter*, 2006, **18**, 1359–1365.

[86] Saito, R. and Murayama, K. 'A universal distribution function of relaxation in amorphous materials'. *Solid State Commun.* 1987, **63**, 625–627.

[87] Randall, J. T. and Wilkins, M. H. F. 'Phosphorescence and electron traps. II. The interpretation of long-period phosphorescence'. *Proc. Royal Soc. A*, 1945, **184**, 390–407.

[88] Dunstan, D. J. 'Kinetics of distant-pair recombination'. *Philos. Mag. B*, 1982, **46**, 579–594.

[89] Jonscher, A. K. and Polignac, A. de. 'The time dependence of luminescence in solids'. *J. Phys. C: Solid State Phys.* 1984, **17**, 6493–6519.

[90] Street, R. 'Luminescence and recombination in hydrogenated amorphous silicon'. *Adv. Phys.* 1981, **30**, 593–676.

[91] Kuno, M., Fromm, D. P., Hamann, H. F., Gallagher, A. and Nesbitt, D. J. 'Nonexponential "blinking" kinetics of single CdSe quantum dots: a universal power law behavior'. *J. Chem. Phys.* 2000, **112**, 3117–3120.

[92] McNeil, I. J., Ashford, D. L., Luo, H. and Fecko, C. J. 'Power-law kinetics in the photoluminescence of dye-sensitized nanoparticle films: implications for electron injection and charge transport'. *J. Phys. Chem. C*, 2012, **116**, 15888–15899.

[93] Orenstein, J. and Kastner, M. A. 'Thermalization and recombination in amorphous semiconductors'. *Solid State Commun.* 1981, **40**, 85–89.

[94] Randall, J. T. and Wilkins, M. H. F. 'Phosphorescence and electron traps. I. The study of trap distributions'. *Proc. Royal Soc. A*, 1945, **184**, 365–389.

[95] Monroe, D. 'Hopping in exponential band tails'. *Phys. Rev. Lett.* 1985, **54**, 146–149.

[96] Zhu, X.-Y. and Podzorov, V. 'Charge carriers in hybrid organic-inorganic lead halide perovskites might be protected as large polarons'. *J. Phys. Chem. Lett.* 2015, **6**, 4758–4761.

[97] Yang, Y., Ostrowski, D. P., France, R. M., Zhu, K., Lagemaat, J. van de, Luther, J. M. and Beard, M. C. 'Observation of a hot-phonon bottleneck in lead-iodide perovskites'. *Nature Photon.* 2015, **10**, 53–59.

[98] Seitz, F. 'On the mobility of electrons in pure non-polar insulators'. *Phys. Rev.* 1948, **73**, 549–564.

[99] Bardeen, J. and Shockley, W. 'Deformation potentials and mobilities in non-polar crystals'. *Phys. Rev.* 1950, **80**, 72–80.

[100] Petritz, R. and Scanlon, W. 'Mobility of electrons and holes in the polar crystal, PbS'. *Phys. Rev.* 1955, **97**, 1620–1626.

[101] Ferry, D. 'First-order optical and intervalley scattering in semiconductors'. *Phys. Rev. B*, 1976, **14**, 1605–1609.

[102] Oga, H., Saeki, A., Ogomi, Y., Hayase, S. and Seki, S. 'Improved understanding of the electronic and energetic landscapes of perovskite solar cells: high local charge carrier mobility, reduced recombination, and extremely shallow traps.' *J. Am. Chem. Soc.* 2014, **136**, 13818–13825.

[103] Savenije, T., Ponseca, C., Kunneman, L., Abdellah, M., Zheng, K., Tian, Y., Zhu, Q., Canton, S. E., Schlebykin, I. G., Pullerits, T., Yartsev, A. and Sundström, V. 'Thermally activated exciton dissociation and recombination control the carrier dynamics in organometal halide perovskite'. *J. Phys. Chem. Lett.* 2014, **5**, 2189–2194.

[104] Karakus, M., Jensen, S. A., D'Angelo, F., Turchinovich, D., Bonn, M. and Canovas, E. 'Phonon-electron scattering limits free charge mobility in methylammonium lead iodide perovskites.' *J. Phys. Chem. Lett.* 2015, **6**, 4991–4996.

[105] Benavides-Garcia, M. and Balasubramanian, K. 'Bond energies, ionization potentials, and the singlet-triplet energy separations of $SnCl_2$, $SnBr_2$, SnI_2, $PbCl_2$, $PbBr_2$, PbI_2, and their positive ions'. *J. Chem. Phys.* 1994, **100**, 2821–2830.

[106] Viswanath, A., Lee, J., Kim, D., Lee, C. and Leem, J. 'Exciton-phonon interactions, exciton binding energy, and their importance in the realization of room-temperature semiconductor lasers based on GaN'. *Phys. Rev. B*, 1998, **58**, 16333–16339.

[107] Stillman, G., Wolfe, C. and Dimmock, J. 'Hall coefficient factor for polar mode scattering in n-type GaAs'. *J. Phys. Chem. Solids*, 1970, **31**, 1199–1204.

[108] Kim, Y.-H., Cho, H. and Lee, T.-W. 'Metal halide perovskite light emitters'. *PNAS*, 2016, **113**, 11694–11702.

[109] Meng, L., Yao, E.-P., Hong, Z., Chen, H., Sun, P., Yang, Z., Li, G. and Yang, Y. 'Pure formamidinium-based perovskite light-emitting diodes with high efficiency and low driving voltage'. *Adv. Mater.* 2017, **29**, 1603826.

[110] Motti, S. G., Gandini, M., Barker, A. J., Ball, J. M., Srimath Kandada, A. R. and Petrozza, A. 'Photoinduced emissive trap states in lead halide perovskite semiconductors'. *ACS Energy Lett.* 2016, **1**, 726–730.

[111] Leijtens, T., Eperon, G. E., Barker, A. J., Grancini, G., Zhang, W., Ball, J. M., Kandada, A. R. S., Snaith, H. J. and Petrozza, A. 'Carrier trapping and recombination: the role of defect physics in enhancing the open circuit voltage of metal halide perovskite solar cells'. *Energy Environ. Sci.* 2016, **9**, 3472–3481.

[112] Baumann, A., Väth, S., Rieder, P., Heiber, M. C., Tvingstedt, K. and Dyakonov, V. 'Identification of trap states in perovskite solar cells'. *J. Phys. Chem. Lett.* 2015, **6**, 2350–2354.

[113] Leijtens, T., Stranks, S. D., Eperon, G. E., Lindblad, R., Johansson, E. M. J., Ball, J. M., Lee, M. M., Snaith, H. J. and Mcpherson, I. J. 'Electronic properties of meso-superstructured and planar organometal halide perovskite films: charge trapping, photodoping, and carrier mobility'. *ACS Nano*, 2014, **8**, 7147–7155.

[114] Dar, M. I., Jacopin, G., Meloni, S., Mattoni, A., Arora, N., Boziki, A., Zakeeruddin, S. M., Rothlisberger, U. and Graetzel, M. 'Origin of unusual bandgap shift and dual emission in organic-inorganic lead halide perovskites'. *Sci. Adv.* 2016, **2**, e1601156.

[115] Yin, W.-J., Shi, T. and Yan, Y. 'Unusual defect physics in $CH_3NH_3PbI_3$ perovskite solar cell absorber.' *Appl. Phys. Lett.* 2014, **104**, 063903.

[116] Srimath Kandada, A. R., Neutzner, S., D'Innocenzo, V., Tassone, F., Gandini, M., Akkerman, Q. A., Prato, M., Manna, L., Petrozza, A. and Lanzani, G. 'Non-linear carrier Interactions in lead halide perovskites and the role of defects.' *J. Am. Chem. Soc.* 2016, **138**, 13604–13611.

[117] Yamada, Y., Yamada, T., Shimazaki, A., Wakamiya, A. and Kanemitsu, Y. 'Interfacial charge-carrier trapping in $CH_3NH_3PbI_3$ -based heterolayered structures revealed by time-resolved photoluminescence spectroscopy'. *J. Phys. Chem. Lett.* 2016, **7**, 1972–1977.

[118] Duan, H.-S., Zhou, H., Chen, Q., Sun, P., Luo, S., Song, T.-B., Bob, B. and Yang, Y. 'The identification and characterization of defect states in hybrid organic–inorganic perovskite photovoltaics'. *Phys. Chem. Chem. Phys.* 2014, **17**, 112–116.

[119] Kim, J., Lee, S.-h., Lee, J. H. and Hong, K.-h. 'The role of intrinsic defects in methylammonium lead iodide perovskite'. *J. Phys. Chem. Lett.* 2014, **5**, 1312–1317.

[120] Zhang, W., Eperon, G. E. and Snaith, H. J. 'Metal halide perovskites for energy applications'. *Nat. Energy*, 2016, **1**, 16048.

[121] DeQuiletttes, D. W., Zhang, W., Burlakov, V. M., Graham, D. J., Leijtens, T., Osherov, A., Snaith, H. J., Ginger, D. S. and Stranks, S. D. 'Photo-induced halide redistribution in organic–inorganic perovskite films'. *Nat. Commun.* 2016, **7**, 11683.

[122] De Wolf, S., Holovsky, J., Moon, S.-J., Löper, P., Niesen, B., Ledinsky, M., Haug, F.-J., Yum, J.-H. and Ballif, C. 'Organometallic halide perovskites: sharp optical absorption edge and its relation to photovoltaic performance'. *J. Phys. Chem. Lett.* 2014, **5**, 1035–1039.

[123] He, H., Yu, Q., Li, H., Li, J., Si, J., Jin, Y., Wang, N., Wang, J., He, J., Wang, X., Zhang, Y. and Ye, Z. 'Exciton localization in solution-processed organolead trihalide perovskites'. *Nat. Commun.* 2016, **7**, 10896.

[124] Sadhanala, A., Deschler, F., Thomas, T. H., Dutton, S. E., Goedel, K. C., Hanusch, F. C., Lai, M. L., Steiner, U., Bein, T., Docampo, P., Cahen, D. and Friend, R. H. 'Preparation of single phase films of $CH_3NH_3Pb(I_{1-x}Br_x)_3$ with sharp optical band edges'. *J. Phys. Chem. Lett.* 2014, **5**, 2501–2505.

[125] Yamada, Y., Nakamura, T., Endo, M., Wakamiya, A. and Kanemitsu, Y. 'Near-band-edge optical responses of solution-processed organic–inorganic hybrid perovskite $CH_3NH_3PbI_3$ on mesoporous TiO_2 electrodes'. *Appl. Phys. Express*, 2014, **7**, 032302.

[126] Sa-Yakanit, V. and Glyde, N. R. 'Urbach tails and disorder'. *Comments Cond. Mat. Phys.* 1987, **13**, 35–38.

[127] Endres, J., Egger, D. A., Kulbak, M., Kerner, R. A., Zhao, L., Silver, S. H., Hodes, G., Rand, B. P., Cahen, D., Kronik, L. and Kahn, A. 'Valence and conduction band densities of states of metal halide perovskites: a combined experimental - theoretical study'. *J. Phys. Chem. Lett.* 2016, **7**, 2722–2729.

[128] Buin, A., Comin, R., Xu, J., Ip, A. H. and Sargent, E. H. 'Halide-dependent electronic structure of organolead perovskite materials'. *Chem. Mater.* 2015, **27**, 4405–4412.

[129] Fang, X., Zhang, K., Li, Y., Yao, L., Zhang, Y., Wang, Y., Zhai, W., Tao, L., Du, H. and Ran, G. 'Effect of excess $PbBr_2$ on photoluminescence spectra of $CH_3NH_3PbBr_3$ perovskite particles at room temperature'. *Appl. Phys. Lett.* 2016, **108**, 071109.

[130] Meyer, E., Mutukwa, D., Zingwe, N. and Taziwa, R. 'Lead-free halide double perovskites: a review of the structural, optical , and stability properties as well as their viability to replace lead halide perovskites'. *Metals*, 2018, **8**, 1–16.

[131] Lyu, M., Yun, J.-H., Chen, P., Hao, M. and Wang, L. 'Addressing toxicity of lead: progress and applications of low-toxic metal halide perovskites and their derivatives'. *Adv. Energy Mater.* 2017, **7**, 1602512.

[132] Shi, Z., Guo, J., Chen, Y., Li, Q., Pan, Y., Zhang, H., Xia, Y. and Huang, W. 'Lead-free organic-inorganic hybrid perovskites for photovoltaic applications: recent advances and perspectives'. *Adv. Mater.* 2017, **29**, 1605005.

[133] Konstantakou, M. and Stergiopoulos, T. 'A critical review on tin halide perovskite solar cells'. *J. Mater. Chem. A*, 2017, **5**, 11518–11549.

[134] Chatterjee, S. and Pal, A. J. 'Influence of metal substitution on hybrid halide perovskites: towards lead-free perovskite solar cells'. *J. Mater. Chem. A*, 2018, **6**, 3793–3823.

[135] Volonakis, G., Filip, M. R., Haghighirad, A. A., Sakai, N., Wenger, B., Snaith, H. J. and Giustino, F. 'Lead-free halide double perovskites via heterovalent substitution of noble metals'. *J. Phys. Chem. Lett.* 2016, **7**, 1254–1259.

[136] He, Y. and Galli, G. 'Perovskites for solar thermoelectric applications: a first principle study of $CH_3NH_3AI_3$ (A = Pb and Sn)'. *Chem. Mater.* 2014, **26**, 5394–5400.

[137] Giustino, F. and Snaith, H. J. 'Towards lead-free perovskite solar cells'. *ACS Energy Lett.* 2016, **1**, 1233–1240.

[138] Volonakis, G., Haghighirad, A. A., Milot, R. L., Sio, W. H., Filip, M. R., Wenger, B., Johnston, M. B., Herz, L. M., Snaith, H. J. and Giustino, F. '$Cs_2InAgCl_6$: a new lead-free halide double perovskite with direct band gap'. *J. Phys. Chem. Lett.* 2017, **8**, 772–778.

[139] McClure, E. T., Ball, M. R., Windl, W. and Woodward, P. M. 'Cs_2AgBiX_6 (X = Br, Cl) — new visible light absorbing, lead-free halide perovskite semiconductors'. *Chem. Mater.* 2016, **28**, 1348–1354.

[140] Filip, M. R., Hillman, S., Haghighirad, A.-A., Snaith, H. J. and Giustino, F. 'Band gaps of the lead-free halide double perovskites $Cs_2BiAgCl_6$ and $Cs_2BiAgBr_6$ from theory and experiment'. *J. Phys. Chem. Lett.* 2016, **7**, 2579–2585.

[141] Greul, E., Petrus, M. L., Binek, A., Docampo, P. and Bein, T. 'Highly stable, phase pure $Cs_2AgBiBr_6$ double perovskite thin films for optoelectronic applications'. *J. Mater. Chem. A*, 2017, **5**, 19972.

[142] Deng, Z., Wei, F., Sun, S., Kieslich, G., Cheetham, A. K. and Bristowe, P. D. 'Exploring the properties of lead-free hybrid double perovskites using a combined computational-experimental approach'. *J. Mater. Chem. A*, 2016, **4**, 12025–12029.

[143] Slavney, A. H., Leppert, L., Bartesaghi, D., Gold-Parker, A., Toney, M. F., Savenije, T. J., Neaton, J. B. and Karunadasa, H. I. 'Defect-induced band-edge reconstruction of a bismuth-halide double perovskite for visible-light absorption'. *J. Am. Chem. Soc.* 2017, **139**, 5015–5018.

[144] Cvjetko, P., Cvjetko, I. and Pavlica, M. 'Thallium toxicity in humans'. *Arh. Hig. Rada Toksikol.* 2010, **61**, 111–119.

[145] Pan, W., Wu, H., Luo, J., Deng, Z., Ge, C., Chen, C., Jiang, X., Yin, W.-j., Niu, G., Zhu, L., Yin, L., Zhou, Y., Xie, Q. and Ke, X. '$Cs_2AgBiBr_6$ single-crystal X-ray detectors with a low detection limit'. *Nature Photon.* 2017, **11**, 726–732.

[146] Li, H., Shan, X., Neu, J. N., Geske, T., Davis, M., Mao, P., Xiao, K., Siegrist, T. and Yu, Z. 'Lead-free halide double perovskite-polymer composites for flexible X-ray imaging'. *J. Mater. Chem. C*, 2018, Advance Article.

[147] Pelant, I. and Valenta, J. *Luminescence Spectroscopy of Semiconductors*. Oxford University Press, 2012.

[148] Etoh, T. G., Nguyen, A. Q., Kamakura, Y., Shimonomura, K., Le, T. Y. and Mori, N. 'The theoretical highest frame rate of silicon image sensors'. *Sensors*, 2017, **17**, 483.

[149] Fellers, T. J. and Davidson, M. W. *Digital Camera Readout and Frame Rates*. 2018. `http://hamamatsu.magnet.fsu.edu/articles/readoutandframerates.html` (visited on 01/09/2018).

[150] Andor. *Intensified CCD Cameras*. `https://andor.oxinst.com/learning/view/article/intensified-ccd-cameras` (visited on 01/09/2018).

[151] Princeton Instruments. *PI-MAX4 System*. 4. Princeton Instruments, 2014.

[152] Becker, W. *The bh TCSPC Handbook*. Becker & Hickl GmbH, 2017.

[153] Wahl, M. *Time-Correlated Single Photon Counting*. Tech. rep. Berlin, Germany: PicoQuant, 2014.

[154] Lakowicz, J. R. *Principles of Fluorescence Spectroscopy*. Springer, 2006.

[155] Knight, A. J., Wright, A. D., Patel, J. B., Mcmeekin, D. P., Snaith, H. J., Johnston, M. B. and Herz, L. M. 'Electronic traps and phase segregation in lead mixed-halide perovskite'. *ACS Energy Lett.* 2019, **4**, 75–84.

[156] Fox, M. *Optical Properties of Solids*. Oxford University Press, 2001.

[157] Newport. *Technical Note: Introduction to FTIR Spectroscopy*. `https://www.newport.com/n/introduction-to-ftir-spectroscopy` (visited on 05/09/2018).

[158] Xiao, M., Huang, F., Huang, W., Dkhissi, Y., Zhu, Y., Etheridge, J., Gray-Weale, A., Bach, U., Cheng, Y. B. and Spiccia, L. 'A fast deposition-crystallization procedure for highly efficient lead iodide perovskite thin-film solar cells'. *Angew. Chem. Int. Ed.* 2014, **126**, 10056–10061.

[159] Longo, G., Wright, A. D., Johnston, M. B., Herz, L. M. and Snaith, H. J. '$Cs_2AgBiBr_6$ double perovskite thin films prepared by vapor deposition'. *Manuscript in Preparation*, 2018.

[160] Baikie, T., Fang, Y., Kadro, J. M., Schreyer, M., Wei, F., Mhaisalkar, S. G., Gratzel, M., White, T. J., Graetzel, M., White, T. J., Gratzel, M. and White, T. J. 'Synthesis and crystal chemistry of the hybrid perovskite $(CH_3NH_3)PbI_3$ for solid-state sensitised solar cell applications'. *J. Mater. Chem. A*, 2013, **1**, 5628–5641.

[161] Giannozzi, P. et al. 'QUANTUM ESPRESSO: a modular and open-source software project for quantum simulations of materials.' *J. Phys.: Condens. Matter.* 2009, **21**, 395502.

[162] Filip, M. R. and Giustino, F. '*GW* quasiparticle band gap of the hybrid organic-inorganic perovskite $CH_3NH_3PbI_3$: effect of spin-orbit interaction, semicore electrons, and self-consistency'. *Phys. Rev. B*, 2014, **90**, 245145.

[163] Marini, A., Hogan, C., Grüning, M. and Varsano, D. '`yambo`: An ab initio tool for excited state calculations'. *Comp. Phys. Commun.* 2009, **180**, 1392–1403.

[164] Filip, M. R., Verdi, C. and Giustino, F. '*GW* band structures and carrier effective masses of $CH_3NH_3PbI_3$ and hypothetical perovskites of the type $APbI_3$: A = NH_4, PH_4, AsH_4, and SbH_4'. *J. Phys. Chem. C*, 2015, **119**, 25209–25219.

[165] Mostofi, A. A., Yates, J. R., Lee, Y.-S., Souza, I., Vanderbilt, D. and Marzari, N. '`wannier90`: a tool for obtaining maximally-localised Wannier functions'. *Comp. Phys. Commun.* 2008, **178**, 685–699.

[166] Pérez-Osorio, M. A., Milot, R. L., Filip, M. R., Patel, J. B., Herz, L. M., Johnston, M. B. and Giustino, F. 'Vibrational properties of the organic-inorganic halide perovskite $CH_3NH_3PbI_3$ from theory and experiment: factor group analysis, first-principles calculations, and low-temperature infrared spectra'. *J. Phys. Chem. C*, 2015, **119**, 25703–25718.

[167] Swainson, I., Hammond, R., Soullière, C., Knop, O. and Massa, W. 'Phase transitions in the perovskite methylammonium lead bromide, $CH_3ND_3PbBr_3$'. *J. Solid State Chem.* 2003, **176**, 97–104.

[168] Giustino, F., Cohen, M. L. and Louie, S. G. 'Electron-phonon interaction using Wannier functions'. *Phys. Rev. B*, 2007, **76**, 165108.

[169] Poncé, S., Margine, E. R., Verdi, C. and Giustino, F. 'EPW: Electron–phonon coupling, transport and superconducting properties using maximally localized Wannier functions'. *Comp. Phys. Commun.* 2016, **209**, 116–133.

[170] Verdi, C. and Giustino, F. 'Fröhlich electron-phonon vertex from first principles'. *Phys. Rev. Lett.* 2015, **115**, 176401.

[171] Jeon, N. J., Noh, J. H., Yang, W. S., Kim, Y. C., Ryu, S., Seo, J. and Seok, S. I. 'Compositional engineering of perovskite materials for high-performance solar cells'. *Nature*, 2015, **517**, 476–480.

[172] Binek, A., Hanusch, F. C., Docampo, P. and Bein, T. 'Stabilization of the trigonal high temperature phase of formamidinium lead iodide'. *J. Phys. Chem. Lett.* 2015, **6**, 1249–1253.

[173] Eperon, G. E., Beck, C. E. and Snaith, H. J. 'Cation exchange for thin film lead iodide perovskite interconversion'. *Mater. Horiz.* 2015, **3**, 63–71.

[174] McMeekin, D. P., Sadoughi, G., Rehman, W., Eperon, G. E., Saliba, M., Hörantner, M. T., Haghighirad, A., Sakai, N., Korte, L., Rech, B., Johnston, M. B., Herz, L. M. and Snaith, H. J. 'A mixed-cation lead mixed-halide perovskite absorber for tandem solar cells'. *Science*, 2016, **351**, 151–155.

[175] Ha, S. T., Liu, X., Zhang, Q., Giovanni, D., Sum, T. C. and Xiong, Q. 'Synthesis of organic-inorganic lead halide perovskite nanoplatelets: towards high-performance perovskite solar cells and optoelectronic devices'. *Adv. Opt. Mater.* 2014, **2**, 838–844.

[176] Fang, H.-H., Wang, F., Adjokatse, S., Zhao, N., Even, J. and Loi, M. A. 'Photoexcitation dynamics in solution- processed formamidinium lead iodide perovskite thin films for solar cell applications'. *Light Sci. Appl*, 2016, **5**, e16056.

[177] Onoda-Yamamuro, N., Matsuo, T. and Suga, H. 'Calorimetric and IR spectroscopic studies of phase transitions in methylammonium trihalogenoplumbates (II)'. *J. Phys. Chem. Solids*, 1990, **51**, 1383–1395.

[178] Wasylishen, R., Knop, O. and Macdonald, J. 'Cation rotation in methylammonium lead halides'. *Solid State Commun.* 1985, **56**, 581–582.

[179] Varshni, Y. 'Temperature dependence of the energy gap in semiconductors'. *Physica*, 1967, **34**, 149–154.

[180] Frost, J. J. M. J., Butler, K. K. T., Brivio, F., Hendon, C. H., Schilfgaarde, M. van and Walsh, A. 'Atomistic origins of high-performance in hybrid halide perovskite solar cells'. *Nano Lett.* 2014, **14**, 2584–2590.

[181] Wehrenfennig, C., Liu, M., Snaith, H. J., Johnston, M. B. and Herz, L. M. 'Charge carrier recombination channels in the low-temperature phase of organic-inorganic lead halide perovskite thin films'. *APL Mater.* 2014, **2**, 081513.

[182] Wu, X., Trinh, M. T., Niesner, D., Zhu, H., Norman, Z., Owen, J. S., Yaffe, O., Kudisch, B. J. and Zhu, X. X.-Y. 'Trap states in lead iodide perovskites'. *J. Am. Chem. Soc.* 2015, **137**, 2089–2096.

[183] Priante, D., Dursun, I., Alias, M. S., Shi, D., Melnikov, V. a., Ng, T. K., Mohammed, O. F., Bakr, O. M. and Ooi, B. S. 'The recombination mechanisms leading to amplified spontaneous emission at the true-green wavelength in $CH_3NH_3PbBr_3$ perovskites'. *Appl. Phys. Lett.* 2015, **106**, 081902.

[184] Rudin, S., Reinecke, T. L. and Segall, B. 'Temperature-dependent exciton linewidths in semiconductors'. *Phys. Rev. B*, 1990, **42**, 11218–11231.

[185] Lee, J., Koteles, E. S. and Vassell, M. O. 'Luminescence linewidths of excitons in GaAs quantum wells below 150 K'. *Phys. Rev. B*, 1986, **33**, 5512–5516.

[186] Malikova, L., Krystek, W., Pollak, F., Dai, N., Cavus, A. and Tamargo, M. 'Temperature dependence of the direct gaps of ZnSe and $Zn_{0.56}Cd_{0.44}Se$'. *Phys. Rev. B*, 1996, **54**, 1819–1824.

[187] Chen, Y., Kothiyal, G., Singh, J. and Bhattacharya, P. 'Absorption and photoluminescence studies of the temperature dependence of exciton life time in lattice-matched and strained quantum well systems'. *Superlattice Microst.* 1987, **3**, 657–664.

[188] Bartolo, B. D. and Chen, X. *Advances in Energy Transfer Processes*. World Scientific, 2001.

[189] Selci, S., Cricenti, A., Righini, M., Petrillo, C., Sacchetti, F., Alexandre, F. and Chiarotti, G. 'Evaluation of electron-phonon coupling of $Al_{0.27}Ga_{0.73}As$/GaAs quantum wells by normal incidence reflectance'. *Solid State Commun.* 1991, **79**, 561–565.

[190] Masumoto, Y. and Takagahara, T. *Semiconductor Quantum Dots*. Springer-Verlag, 2002.

[191] Spiegelberg, F., Gutsche, E. and Voigt, J. 'Exciton-phonon interaction in CdS'. *Phys. Status Solidi B*, 1976, **77**, 233–242.

[192] Logothetidis, S., Cardona, M., Lautenschlager, P. and Garriga, M. 'Temperature dependence of the dielectric function and the interband critical points of CdSe'. *Phys. Rev. B*, 1986, **34**, 2458–2469.

[193] Gopal, A. V., Kumar, R., Vengurlekar, A. S., Bosacchi, A., Franchi, S. and Pfeiffer, L. N. 'Photoluminescence study of exciton–optical phonon scattering in bulk GaAs and GaAs quantum wells'. *J. Appl. Phys.* 2000, **87**, 1858–1862.

[194] Gammon, D., Rudin, S., Reinecke, T. L., Katzer, D. S. and Kyono, C. S. 'Phonon broadening of excitons in GaAs/AlGaAs quantum wells'. *Phys. Rev. B*, 1995, **51**, 16785–16789.

[195] Qiang, H., Pollak, F. H., Sotomayor Torres, C. M., Leitch, W., Kean, a. H., Stroscio, M. a., Iafrate, G. J. and Kim, K. W. 'Size dependence of the thermal broadening of the exciton linewidth in GaAs/$Ga_{0.7}Al_{0.3}As$ single quantum wells'. *Appl. Phys. Lett.* 1992, **61**, 1411–1413.

[196] Fonoberov, V. A., Alim, K. A., Balandin, A. A., Xiu, F. and Liu, J. 'Photoluminescence investigation of the carrier recombination processes in ZnO quantum dots and nanocrystals'. *Phys. Rev. B*, 2006, **73**, 165317.

[197] Fischer, A., Kim, D., Hays, J., Shan, W., Song, J., Eason, D., Ren, J., Schetzina, J., Luo, H., Furdyna, J., Zhu, Z., Yao, T., Klem, J. and Schäfer, W. 'Femtosecond coherent spectroscopy of bulk ZnSe and ZnCdSe/ZnSe quantum wells'. *Phys. Rev. Lett.* 1994, **73**, 2368–2371.

[198] Hellmann, R., Koch, M., Feldmann, J., Cundiff, S. T., Göbel, E. O., Yakovlev, D. R., Waag, A. and Landwehr, G. 'Homogeneous linewidth of excitons in semimagnetic CdTe/$Cd_{1-x}Mn_xTe$ multiple quantum wells'. *Phys. Rev. B*, 1993, **48**, 2847–2850.

[199] Li, T., Lozykowski, H. and Reno, J. 'Optical properties of CdTe/$Cd_{1-x}Zn_xTe$ strained-layer single quantum wells'. *Phys. Rev. B*, 1992, **46**, 6961–6968.

[200] Zhang, X. B., Taliercio, T., Kolliakos, S. and Lefebvre, P. 'Influence of electron-phonon interaction on the optical properties of III nitride semiconductors'. *J. Phys.: Condens. Matter*, 2001, **13**, 7053–7074.

[201] Yamada, Y. and Nakamura, T. 'Photocarrier recombination dynamics in perovskite $CH_3NH_3PbI_3$ for solar cell applications'. *J. Am. Chem. Soc.* 2014, **136**, 11610–11613.

[202] D'Innocenzo, V., Grancini, G., Alcocer, M. J., Kandada, A. R. S., Stranks, S. D., Lee, M. M., Lanzani, G., Snaith, H. J. and Petrozza, A. 'Excitons versus free charges in organo-lead tri-halide perovskites'. *Nat. Commun.* 2014, **5**, 3586.

[203] Price, M., Butkus, J., Jellicoe, T., Sadhanala, A., Briane, A., Halpert, J., Broch, K., Hodgkiss, J., Friend, R. and Deschler, F. 'Hot carrier cooling and photo-induced refractive index changes in organic-inorganic lead halide perovskites.' *Nat. Commun.* 2015, **6**, 8420.

[204] Gopalan, S., Lautenschlager, P. and Cardona, M. 'Temperature dependence of the shifts and broadenings of the critical points in GaAs'. *Phys. Rev. B*, 1987, **35**, 5577–5584.

[205] Grimvall, G. *The Electron-Phonon Interaction in Metals*. North-Holland, 1981.

[206] Hirasawa, M., Ishihara, T., Goto, T., Uchida, K. and Miura, N. 'Magnetoabsorption of the lowest exciton in perovskite-type compound (CH_3NH_3)PbI_3'. *Physica B*, 1994, **201**, 427–430.

[207] Tanaka, K., Takahashi, T., Ban, T., Kondo, T., Uchida, K. and Miura, N. 'Comparative study on the excitons in lead-halide-based perovskite-type crystals $CH_3NH_3PbBr_3CH_3NH_3PbI_3$'. *Solid State Commun.* 2003, **127**, 619–623.

[208] Wehrenfennig, C., Liu, M., Snaith, H. J., Johnston, M. B. and Herz, L. M. 'Charge-carrier dynamics in vapour-deposited films of the organolead halide perovskite $CH_3NH_3PbI_{3-x}Cl_x$'. *Energy Environ. Sci.* 2014, **7**, 2269–2275.

[209] Kawai, H., Giorgi, G., Marini, A. and Yamashita, K. 'The mechanism of slow hot-hole cooling in lead-iodide perovskite: first-principle calculation on carrier lifetime from electron-phonon interaction.' *Nano Lett.* 2015, **15**, 3103–3108.

[210] Linde, D. von der and Lambrich, R. 'Direct measurement of hot-electron relaxation by picosecond spectroscopy'. *Phys. Rev. Lett.* 1979, **42**, 1090–1093.

[211] Bi, D., Tress, W., Dar, M. I., Gao, P., Luo, J., Renevier, C., Schenk, K., Abate, A., Giordano, F., Correa Baena, J.-P., Decoppet, J.-D., Zakeeruddin, S. M., Nazeeruddin, M. K., Grätzel, M. and Hagfeldt, A. 'Efficient luminescent solar cells based on tailored mixed-cation perovskites'. *Sci .Adv.* 2016, **2**, e1501170.

[212] Baranovskii, S., Eichmann, R. and Thomas, P. 'Temperature-dependent exciton luminescence in quantum wells by computer simulation'. *Phys. Rev. B*, 1998, **58**, 13081–13087.

[213] Galkowski, K., Mitioglu, A., Miyata, A., Plochocka, P., Portugall, O., Eperon, G. E., Wang, J. T.-W., Stergiopoulos, T., Stranks, S. D., Snaith, H. J. and Nicholas, R. J. 'Determination of the exciton binding energy and effective masses for methylammonium and formamidinium lead tri-halide perovskite semiconductors'. *Energy Environ. Sci.* 2016, **9**, 962–970.

[214] Han, Q., Bae, S.-H., Sun, P., Hsieh, Y.-T., Yang, Y. M., Rim, Y. S., Zhao, H., Chen, Q., Shi, W., Li, G. and Yang, Y. 'Single crystal formamidinium lead iodide ($FAPbI_3$): insight into the structural, optical, and electrical properties'. *Adv. Mater.* 2016, **28**, 2253–2258.

[215] Dunstan, D. J. and Boulitrop, F. 'Photoluminescence in hydrogenated amorphous silicon'. *Phys. Rev. B*, 1984, **30**, 5945–5957.

[216] Tiedje, T. and Rose, A. 'A physical interpretation of dispersive transport in disordered semiconductors'. *Solid State Commun.* 1981, **37**, 49–52.

[217] Eliseev, P. G., Osinski, M., Lee, J., Sugahara, T. and Sakai, S. 'Band-tail model and temperature-induced blue-shift in photoluminescence spectra of $In_xGa_{1-x}N$ grown on sapphire'. *J. Electron. Mater*, 2000, **29**, 332–341.

[218] Svane, A., Christensen, N. E., Cardona, M., Chantis, A. N., Van Schilfgaarde, M. and Kotani, T. 'Quasiparticle self-consistent *GW* calculations for PbS, PbSe, and PbTe: Band structure and pressure coefficients'. *Phys. Rev. B*, 2010, **81**, 1–10.

[219] Xing, G., Mathews, N., Lim, S. S., Yantara, N., Liu, X., Sabba, D., Grätzel, M., Mhaisalkar, S. and Sum, T. C. 'Low-temperature solution-processed wavelength-tunable perovskites for lasing.' *Nat. Mater.* 2014, **13**, 476–480.

[220] Kong, W., Ye, Z., Qi, Z., Zhang, B., Wang, M., Rahimi-Iman, A., Wu, H., Lifshitz, E., Yassen, M., Bykov, L. and Dag, I. 'Characterization of an abnormal photoluminescence behavior upon crystal-phase transition of perovskite $CH_3NH_3PbI_3$'. *Phys. Chem. Chem. Phys.* 2015, **17**, 16405–16411.

[221] Panzer, F., Baderschneider, S., Gujar, T. P., Unger, T., Bagnich, S., Jakoby, M., Bässler, H., Hüttner, S., Köhler, J., Moos, R., Thelakkat, M., Hildner, R. and Köhler, A. 'Reversible laser induced amplified spontaneous emission from coexisting tetragonal and orthorhombic phases in hybrid lead halide perovskites'. *Adv. Optical Mater.* 2016, **4**, 917–928.

[222] Tilchin, J., Dirin, D. N., Maikov, G. I., Sashchiuk, A., Kovalenko, M. V. and Lifshitz, E. 'Hydrogen-like Wannier–Mott excitons in single crystal of methylammonium lead bromide perovskite'. *ACS Nano*, 2016, **10**, 6363–6371.

[223] Rubel, O., Galluppi, M., Baranovskii, S. D., Volz, K., Geelhaar, L., Riechert, H., Thomas, P. and Stolz, W. 'Quantitative description of disorder parameters in (GaIn)(NAs) quantum wells from the temperature-dependent photoluminescence spectroscopy'. *J. Appl. Phys.* 2005, **98**, 063518.

[224] Kazlauskas, K., Tamulaitis, G., Žukauskas, A., Khan, M. A., Yang, J. W., Zhang, J., Simin, G., Shur, M. S. and Gaska, R. 'Double-scaled potential profile in a group-III nitride alloy revealed by Monte Carlo simulation of exciton hopping'. *Appl. Phys. Lett.* 2003, **83**, 3722–3724.

[225] Friel, I., Thomidis, C. and Moustakas, T. D. 'Well width dependence of disorder effects on the optical properties of AlGaN/GaN quantum wells'. *Appl. Phys. Lett.* 2004, **85**, 3068–3070.

[226] Yin, W. J., Shi, T. and Yan, Y. 'Unique properties of halide perovskites as possible origins of the superior solar cell performance'. *Adv. Mater.* 2014, **26**, 4653–4658.

[227] Li, Q., Xu, S. J., Cheng, W. C., Xie, M. H., Tong, S. Y., Che, C. M. and Yang, H. 'Thermal redistribution of localized excitons and its effect on the luminescence band in InGaN ternary alloys'. *Appl. Phys. Lett.* 2001, **79**, 1810–1812.

[228] Li, Q., Xu, S. J., Xie, M. H. and Tong, S. Y. 'Origin of the 'S-shaped' temperature dependence of luminescent peaks from semiconductors'. *J. Phys.: Condens. Matter*, 2005, **17**, 4853–4858.

[229] Li, Q., Xu, S. J., Xie, M. H. and Tong, S. Y. 'A model for steady-state luminescence of localized-state ensemble'. *Europhys Lett.* 2005, **71**, 994–1000.

[230] Baranovskii, S. D. 'Theoretical description of charge transport in disordered organic semiconductors'. *Phys. Status Solidi B*, 2014, **251**, 487–525.

[231] Könenkamp, R. *Photoelectric Properties and Applications of Low-Mobility Semiconductors*. Springer Berlin Heidelberg, 2000.

[232] Baranowski, M., Latkowska, M., Kudrawiec, R. and Misiewicz, J. 'Model of hopping excitons in GaInNAs: simulations of sharp lines in micro-photoluminescence spectra and their dependence on the excitation power and temperature'. *Journal of Physics: Condensed Matter*, 2011, **23**, 205804.

[233] Miller, A. and Abrahams, E. 'Impurity conduction at low concentrations'. *Phys. Rev.* 1960, **120**, 745–755.

[234] Dal Don, B., Kohary, K., Tsitsishvili, E., Kalt, H., Baranovskii, S. D. and Thomas, P. 'Quantitative interpretation of the phonon-assisted redistribution processes of excitons in $Zn_{1-x}Cd_xSe$ quantum islands'. *Phys. Rev. B*, 2004, **69**, 045318.

[235] De Bastiani, M., D'Innocenzo, V., Stranks, S. D., Snaith, H. J. and Petrozza, A. 'Role of the crystallization substrate on the photoluminescence properties of organolead mixed halides perovskites'. *APL Mater.* 2014, **2**, 081509.

[236] Grancini, G., Marras, S., Prato, M., Giannini, C., Quarti, C., De Angelis, F., De Bastiani, M., Eperon, G. E., Snaith, H. J., Manna, L. and Petrozza, A. 'The impact of the crystallization processes on the structural and optical properties of hybrid perovskite films for photovoltaics'. *J. Phys. Chem. Lett.* 2014, **5**, 3836–3842.

[237] Juarez-Perez, E. and Sanchez, R. 'Photoinduced giant dielectric constant in lead halide perovskite solar cells'. *J. Phys. Chem. Lett.* 2014, **5**, 2390–2394.

[238] March, S. A., Riley, D. B., Clegg, C., Webber, D., Liu, X., Dobrowolska, M., Furdyna, J. K., Hill, I. G. and Hall, K. C. 'Four-wave mixing in perovskite photovoltaic materials reveals long dephasing times and weaker many-body interactions than GaAs'. *ACS Photonics*, 2017, **4**, 1515–1521.

[239] Ma, J. and Wang, L.-W. 'Nanoscale charge localization induced by random orientations of organic molecules in hybrid perovskite $CH_3NH_3PbI_3$'. *Nano Lett.* 2015, **15**, 248–253.

[240] Gokmen, T., Gunawan, O., Todorov, T. K. and Mitzi, D. B. 'Band tailing and efficiency limitation in kesterite solar cells'. *Appl. Phys. Lett.* 2013, **103**, 103506.

[241] Greeff, C. W. and Glyde, H. R. 'Anomalous Urbach tail in GaAs'. *Phys. Rev. B*, 1995, **51**, 1778–1783.

[242] Miller, O. D., Yablonovitch, E. and Kurtz, S. R. 'Strong internal and external luminescence as solar cells approach the Shockley-Queisser limit'. *IEEE J. Photovolt.* 2012, **2**, 303–311.

[243] Tiedje, T. 'Band tail recombination limit to the output voltage of amorphous silicon solar cells'. *Appl. Phys. Lett.* 1982, **40**, 627–629.

[244] Heath, J. T., Cohen, J. D., Shafarman, W. N., Liao, D. X. and Rockett, A. A. 'Effect of Ga content on defect states in $CuIn_{1-x}Ga_xSe_2$ photovoltaic devices'. *Appl. Phys. Lett.* 2002, **80**, 4540–4542.

[245] Phuong, L. Q., Yamada, Y., Nagai, M., Maruyama, N., Wakamiya, A. and Kanemitsu, Y. 'Free carriers versus excitons in $CH_3NH_3PbI_3$ perovskite thin films at low temperatures: charge transfer from the orthorhombic phase to the tetragonal phase'. *J. Phys. Chem. Lett.* 2016, **7**, 2316–2321.

[246] Schade, L., Wright, A. D., Johnson, R. D., Dollmann, M., Nayak, P., Herz, L., Nicholas, R., Snaith, H. and Radaelli, P. G. 'Revealing the relationship between the structural and optical properties in the PV candidate $Cs_2AgBiBr_6$ double perovskite'. *Manuscript in Preparation*, 2018.

[247] Bartesaghi, D., Slavney, A. H., Gélvez-Rueda, M. C., Connor, B. A., Grozema, F. C., Karunadasa, H. I. and Savenije, T. J. 'Charge carrier dynamics in $Cs_2AgBiBr_6$ double perovskite'. *J. Phys. Chem. C*, 2018, **122**, 4809–4816.

[248] Kirchartz, T. and Rau, U. 'Decreasing radiative recombination coefficients via an indirect band gap in lead halide perovskites'. *J. Phys. Chem. Lett.* 2017, **8**, 1265–1271.

[249] Steele, J. A., Puech, P., Keshavarz, M., Yang, R., Banerjee, S., Kim, C. W., Yuan, H., Heo, N. H., Vanacken, J., Walsh, A., Hofkens, J. and Roeffaers, M. B. J. 'Giant electron-phonon coupling and deep conduction band resonance in metal halide double perovskite'. *ACS Nano*, 2018, **12**, 8081–8090.

[250] Elliott, R. J. 'Intensity of optical absorption by excitions'. *Phys. Rev.* 1957, **108**, 1384–1389.

[251] Hoye, R. L. Z., Eyre, L., Wei, F., Brivio, F., Sadhanala, A., Sun, S., Li, W., Zhang, K. H. L., MacManus-Driscoll, J. L., Bristowe, P. D., Friend, R. H., Cheetham, A. K. and Deschler, F. 'Fundamental carrier lifetime exceeding 1 µs in $Cs_2AgBiBr_6$ double perovskite'. *Adv. Mater. Interfaces*, 2018, **5**, 1800464.

[252] Niesner, D., Hauck, M., Shrestha, S., Levchuk, I., Matt, G. J., Osvet, A., Batentschuk, M., Brabec, C., Weber, H. B. and Fauster, T. 'Structural fluctuations cause spin-split states in tetragonal $(CH_3NH_3)PbI_3$ as evidenced by the circular photogalvanic effect'. *PNAS*, 2018, **115**, 9509–9514.

[253] Rooney, A. P., Li, Z., Zhao, W., Gholinia, A., Kozikov, A., Auton, G., Ding, F., Gorbachev, R. V., Young, R. J. and Haigh, S. J. 'Anomalous twin boundaries in two dimensional materials'. *Nat. Commun.* 2018, **9**, 3597.

[254] Grüning, H., Kohary, K., Baranovskii, S. D., Rubel, O., Klar, P. J., Ramakrishnan, A., Ebbinghaus, G., Thomas, P., Heimbrodt, W., Stolz, W. and Rühle, W. W. 'Hopping relaxation of excitons in GaInNAs/GaNAs quantum wells'. *Phys. Status Solidi C*, 2004, **1**, 109–112.

[255] Dal Don, B., Kohary, K., Tsitsischvili, E., Eichmann, R., Baranovskii, S. D., Thomas, P. and Kalt, H. 'Temperature dependent excitonic relaxation in CdSe/ZnSe quantum islands: experiment and computer simulation'. *Phys. Status Solidi C*, 2003, **0**, 1509–1513.

[256] Romero, M. J., Du, H., Teeter, G., Yan, Y. and Al-Jassim, M. M. 'Comparative study of the luminescence and intrinsic point defects in the kesterite Cu_2ZnSnS_4 and chalcopyrite $Cu(In,Ga)Se_2$ thin films used in photovoltaic applications'. *Phys. Rev. B*, 2011, **84**, 1–5.

[257] Menšik, M. and Kral, K. 'Power-law photoluminescence decay in indirect gap quantum dots'. *Microelectron. Eng.* 2013, **111**, 170–174.

[258] Dingle, R. 'Radiative lifetimes of donor-acceptor-pairs in p-type gallium arsenide'. *Phys. Rev.* 1969, **184**, 788–796.

[259] Thomas, D. G., Hopfield, J. J. and Augustyniak, W. M. 'Kinetics of radiative recombination at randomly distributed donors and acceptors'. *Phys. Rev.* 1965, **140**, 202–220.